Growth and properties of GaAs/(In,Ga)As core-shell nanowire arrays on Si

D I S S E R T A T I O N

zur Erlangung des akademischen Grades

d o c t o r r e r u m n a t u r a l i u m
(Dr. rer. nat.)
im Fach Physik
eingereicht an der
Mathematisch-Naturwissenschaftlichen Fakultät
Humboldt-Universität zu Berlin

von
M.Sc. Hanno Küpers

Präsidentin der Humboldt-Universität zu Berlin:
Prof. Dr.-Ing. Dr. Sabine Kunst

Dekan der Mathematisch-Naturwissenschaftlichen Fakultät:
Prof. Dr. Elmar Kulke

Gutachter:
(i) Prof. Dr. Henning Riechert
(ii) Prof. Christoph T. Koch, PhD
(iii) Prof. Dr. Stefano Sanguinetti

Tag der mündlichen Prüfung: 31.07.2018

'Make it count!'
Trice Johnson,
Cyberobics

Abstract

This thesis presents an investigation of the growth of GaAs nanowires (NWs) and (In,Ga)As shells by molecular beam epitaxy (MBE) with a second focus on the optical properties of these core-shell structures. The selective-area growth of GaAs NWs on Si substrates covered by an oxide mask is investigated, revealing the crucial impact of the surface preparation on the vertical yield of NW arrays. Based on these results, a two-step growth approach is presented that enables the growth of thin and untapered NWs while maintaining the high vertical yield. For a detailed quantitative description of the NW shape evolution, a growth model is derived that comprehensively describes the NW shape resulting from changes of the droplet size during elongation and direct vapour-solid growth on the NW sidewalls. This growth model is used to predict the NW shape over a large parameter space to find suitable conditions for the realization of desired NW shapes and dimensions. Using these GaAs NW arrays as templates, the optimum parameters for the growth of (In,Ga)As shells are investigated and we show that the locations of the sources in the MBE system crucially affect the material quality. Here, the three-dimensional structure of the NWs in combination with the substrate rotation and the directionality of material fluxes in MBE results in different flux sequences on the NW sidefacets that determine the growth dynamics and hence, the point defect density. For GaAs NWs with optimum (In,Ga)As shell and outer GaAs shell, we demonstrate that thermionic emission with successive nonradiative recombination at the surface leads to a strong thermal quenching of the luminescence intensity, which is succesfully suppressed by the addition of an AlAs barrier shell to the outer shell structure. Finally, a process is presented that enables the ex-situ annealing of NWs at high temperatures resulting in the reduction of alloy inhomogeneities in the (In,Ga)As shell quantum wells and small emission linewidths.

Keywords: GaAs, nanowire, molecular beam epitaxy, selective-area growth, radial growth, core-shell, (In,Ga)As shell, photoluminescence, carrier dynamics, ex-situ annealing

Zusammenfassung

Diese Arbeit präsentiert Untersuchungen zum Wachstum von GaAs Nanodrähten (NWs) und (In,Ga)As Hüllen mittels Molekularstrahlepitaxie (MBE) mit sekundärem Fokus auf den optischen Eigenschaften solcher Kern-Hülle Strukturen. Das ortsselektive Wachstum von GaAs NWs auf mit Oxidmasken beschichteten Si Substraten wird untersucht, wobei der entscheidende Einfluss der Oberflächenpreparation auf die vertikale Ausbeute von NW Feldern aufgedeckt wird. Basierend auf diesen Ergebnissen wird ein zweistufiger Wachstumprozess präsentiert der es ermöglicht NWs mit dünner und gerade Morphologie zu erhalten ohne die vertikale Ausbeute zu verringern. Für die detaillierte Beschreibung der NW Form wird ein Wachstumsmodell entwickelt, das die Einflüsse der Veränderung der Tropfen Größe während des Wachstums sowie direktes des Wachstums auf den NW Seitenwänden umfassend beschreibt. Dieses Wachstumsmodell wird benutzt für die Vorhersage der NW Form über einen großen Parameterraum um geeignete Bedingungen für die Realisierung von erwünschten NW Formen und Dimensionen zu finden. Ausgehend von diesen NW Feldern werden die optimalen Parameter für das Wachstum von (In,Ga)As Hüllen untersucht und wir zeigen, dass die Anordnung der Materialquellen im MBE System die Materialqualität entscheidend beeinflusst. Die dreidimensionale Struktur der NWs in Kombination mit der Substratrotation und der Richtungsabhängigkeit der Materialflüsse in MBE resultieren in unterschiedlichen Flusssequenzen auf der NW Seitenfacette welche die Wachstumsdynamik und infolgedessen die Punktdefektdichte bestimmen. An Proben mit optimaler (In,Ga)As Hülle und äußerer GaAs Hülle zeigen wir, dass thermionische Emission mit anschließender nichtstrahlender Rekombination auf der Oberfläche zu einem starken thermischen Verlöschen der Lumineszenz Intensität führt, welches durch das Hinzufügen einer AlAs Barrierenhülle zur äußeren Hüllenstruktur erfolgreich unterdrückt werden kann. Abschließend wird ein Prozess präsentiert der das ex-situ Tempern von NWs bei hohen Temperaturen ermöglicht, was in der Reduzierung von Inhomogenitäten in den (In,Ga)As Hüllenquantentöpfen führt und in beispiellosen optischen Eigenschaften resultiert.

Stichwörter: GaAs, Molekularstrahlepitaxie, ortsselektives Wachstum, radiales Wachstum, Kern-Hülle Struktur, (In,Ga)As Hülle, Photolumineszenz, Ladungsträgerdynamik, ex-situ Tempern

List of publications

Publications of parts of this work

H. Küpers, A. Tahraoui, R. B. Lewis, S. Rauwerdink, M. Matalla, O. Krüger, F. Bastiman, H. Riechert, and L. Geelhaar, *Surface preparation and patterning by nano imprint lithography for the selective area growth of GaAs nanowires on Si(111)*, Semicond. Sci. Technol. **32**, 115003 (2017)

H. Küpers, R. B. Lewis, A. Tahraoui, M. Matalla, O. Krüger, F. Bastiman, H. Riechert, and L. Geelhaar, *Diameter evolution of selective area grown Ga-assisted GaAs nanowires*, Nano Res. (2018) DOI: 10.1007/s12274-018-1984-1

H. Küpers, P. Corfdir, R. B. Lewis, T. Flissikowski, A. Tahraoui, H. T. Grahn, O. Brandt, and L. Geelhaar, *Impact of outer shell structure and localization effects on charge carrier dynamics in GaAs/(In,Ga)As nanowire core-shell quantum wells*, submitted for publication in Appl. Phys. Lett.

H. Küpers, R. B. Lewis, M. Niehle, P. Corfdir, A. Trampert, and L. Geelhaar, *Role of flux directionalities for the growth of nanowire shells*, in preparation

Further publications

P. Corfdir, R. B. Lewis, O. Marquardt, H. Küpers, J. Grandal, E. Dimakis, A. Trampert, L. Geelhaar, O. Brandt, and R.T. Phillips, *Exciton recombination at crystal-phase quantum rings in GaAs/$In_xGa_{1-x}As$ core/multishell nanowires*, Appl. Phys. Lett. **109**, 82107 (2016)

P. Corfdir, H. Küpers, R. B. Lewis, T. Flissikowski, H. T. Grahn, L. Geelhaar, and O. Brandt, *Exciton dynamics in GaAs/(Al,Ga)As core-shell nanowires with shell quantum dots*, Phys. Rev. B **94** 155413 (2016)

A. Davtyan, T. Krause, D. Kriegner, A. Al-Hassan, D. Bahrami, S. M. Mostafavi Kashani, R. B. Lewis, H. Küpers, A. Tahraoui, L. Geelhaar, M. Hanke, S. J. Leake, O. Loffeld, and U. Pietsch, *Threefold rotational symmetry in hexagonally shaped core–shell (In,Ga)As/GaAs nanowires revealed by coherent X-ray diffraction imaging*, J. Appl. Crystallogr. **50** 1–8 (2017)

R. B. Lewis, L. Nicolai, H. Küpers, M. Ramsteiner, A. Trampert, and L. Geelhaar, *Anomalous Strain Relaxation in Core–Shell Nanowire Heterostructures via Simultaneous Coherent and Incoherent Growth*, Nano Lett. **17** 136–142 (2017)

R. B. Lewis, P. Corfdir, J. Herranz, H. Küpers, U. Jahn, O. Brandt, and L. Geelhaar, *Self-Assembly of InAs Nanostructures on the Sidewalls of GaAs Nanowires Directed by a Bi Surfactant*, Nano Lett. **17** 4255–4260 (2017)

W. Lin, U. Jahn, H. Küpers, E. Luna, R. B. Lewis, L. Geelhaar, and O. Brandt, *Efficient methodology to correlate structural with optical properties of GaAs nanowires based on scanning electron microscopy*, Nanotechnology **28** 415703 (2017)

A. Al Hassan, R. B. Lewis, H. Küpers, W.-H. Lin, D. Bahrami, T. Krause, D. Salomon, A. Tahraoui, M. Hanke, L. Geelhaar, U. Pietsch, *Determination of indium content of GaAs/(In,Ga)As/(GaAs) core-shell-shell nanowires by x-ray diffraction and nano x-ray fluorescence*, Phys. Rev. Mater. **2** 14604 (2018)

L. Hüttenhofer, R. B. Lewis, S. Rauwerdink, A. Tahraoui, H. Küpers, L. Geelhaar, O. Marquardt, S. Ludwig, *Optimization of ohmic contacts to n-type GaAs nanowires*, arXiv:1711.08284, submitted for publication in Phys. Rev. Applied

R. B. Lewis, P. Corfdir, H. Küpers, T. Flissikowski, O. Brandt, L. Geelhaar, *Nanowires bending over backwards from strain partitioning in asymmetric core–shell heterostructures*, Nano Letters (2018) DOI: 10.1021/acs.nanolett.7b05221

A. Davtyan, V. Favre-Nicolin, R. B. Lewis, H. Küpers, L. Geelhaar, D. Kriegner, D. Bahrami, A. Al-Hassan, G. Chahine, O. Loffeld, and U. Pietsch, *Coherent X-ray diffraction imaging meets ptychography to study core-shell-shell nanowires*, accepted for publication in MRS Advances

Conference presentations

H. Küpers, A. Tahraoui, D. Bahrami, F. Bastiman, U. Pietsch, H. Riechert, and L. Geelhaar, *Comparison of different pre-patterning techniques for the selective-area growth of GaAs nanowires on Si by molecular beam epitaxy*, **(Poster)**, 582. Heraeus Seminar III-V Nanowire Photonics, Bad Honneff, March 2015

H. Küpers, U. Jahn, P. Corfdir, R. B. Lewis, O. Brandt, and L. Geelhaar, *Growth approaches for GaAs/(Al,Ga)As core-shell nanowires in molecular beam epitaxy and their impact on the lu-*

minescence, **(Poster)**, PULSE Summer School: Epitaxy updates and promises, Île de Porquerolles, France, September 2015

H. Küpers, A. Tahraoui, R. B. Lewis, H. Riechert, and L. Geelhaar, *Selective area growth of GaAs nanowires combining high vertical yield and desirable morphology*, **(contributed talk)**, Spring Meeting of the German Physical Society (DPG), Regensburg, March 2016

H. Küpers, R. B. Lewis, A. Tahraoui, M. Matalla, O. Krüger, F. Bastiman, H. Riechert, and L. Geelhaar, *Decoupling nucleation and elongation in selective area growth of GaAs nanowires to achieve high vertical yield and tailored morphology*, **(contributed talk)**, 19^{th} European Workshop on Molecular Beam Epitaxy, Korobitsyno, St. Petersburg, Russia, March 2017

H. Küpers, R. B. Lewis, P. Corfdir, and L. Geelhaar, *Consequences of the deposition sequence inherent to the growth of nanowire shells in molecular beam epitaxy*, **(Poster)**, Nanowire Week, Lund, Sweden, May 2017

H. Küpers, P. Corfdir, R. B. Lewis, T. Flissikowski, A. Tahraoui, H. T. Grahn, O. Brandt, and L. Geelhaar, *Charge carrier dynamics in GaAs/(In,Ga)As/(Al,Ga)As core-multishell nanowire heterostructures*, **(contributed talk)**, Fall Meeting of the Materials Research Society (MRS), Boston, USA, November 2017

Abbreviations

APT	atom probe tomography
CL	cathodoluminescence
CPQR	crystal-phase quantum ring
cw-PL	continuous-wave photoluminescence
EBL	electron-beam lithograhy
FWHM	full width at half maximum
LED	light-emitting diode
MBE	molecular beam epitaxy
MEE	migration enhanced epitaxy
ML	monolayer
MOVPE	metalorganic vapour phase epitaxy
NW	nanowire
PECVD	plasma-enhanced chemical vapour deposition
PL	photoluminescence
QW	quantum well
RHEED	reflection high energy election diffraction
RTA	rapid thermal annealing
SAG	selective-area growth
SEM	scanning electron microscopy
SF	stacking fault
TEM	transmission electron microscopy
TPL	triple phase line
TRPL	time-resolved photoluminescence
UHV	ultra high vacuum
VLS	vapor-liquid-solid
VS	vapor-solid
WZ	wurtzite
XRD	x-ray diffractometry
ZB	zincblende

List of basic symbols

Symbol	Name	Unit
$a_{100,111}$	lattice spacing of the (100) and (111) plane	Å
E_g	band gap energy	eV
f_{eff}	effective flux on sidewall due to desorption from surface	nm/min
$f_{\text{Ga,In,Al,As}}$	molecular fluxes of Ga, In, Al, and As	nm/min
GR_{av}	average growth rate	nm/min
$\hbar$	Planck constant divided by 2π (1.054×10^{-34})	Js
k_B	Boltzmann constant (1.381×10^{-23})	J K^{-1}
k	wavevector or reciprocal space vector	
λ	adatom diffusion length	nm
m_0	electron rest mass (9.109×10^{-31})	kg
n	refractive index	
$n_{\text{FX,Xloc}}$	number density of free and localized excitons	cm^{-3}
$r_{\text{VLS,VS,tot}}$	NW radius due to VLS and VS growth and combined	nm
$R_{5/3}$	experimental V/III flux ratio	
$R_{5/3,\text{ eff.}}$	effective V/III flux ratio in Tersoff's growth model	
ρ	dopant density	cm^{-3}
t_{growth}	growth time	min
τ_{inc}	lifetime of adatom before incorporation	ns
$\tau_{\text{FX,Xloc}}$	radiative lifetime of free and localized exciton	ns
τ_{NR}	nonradiative lifetime of free exciton	ns
T	Temperature	K

Contents

List of publications **vii**

Abbreviations **xi**

List of basic symbols **xiii**

1 Introduction **1**

2 Methods for the growth and analysis of GaAs nanowire core-shell structures **5**
2.1 Semiconductor growth by molecular beam epitaxy 5
2.2 Photoluminescence spectroscopy 8

3 Selective area growth of GaAs nanowires on patterned Si substrates **13**
3.1 Growth of GaAs nanowires 14
3.2 Growth of GaAs nanowires on substrates patterned by electron beam lithography 17
3.2.1 Pattern processing by electron beam lithography 17
3.2.2 Impact of surface preparation on vertical yield 19
3.2.3 Impact of growth parameters on vertical yield 22
3.3 Growth on large scale arrays patterned by nano-imprint lithography . . . 23
3.4 Conclusion 25

4 Diameter evolution of selective area grown GaAs nanowires **27**
4.1 Two-step growth for diameter variation while maintaining high vertical yield 28
4.2 Model for radial growth 30
4.2.1 Descripton of growth model 30
4.2.2 Evaluating the nanowire shape 34
4.2.3 Predictive modelling of the nanowire shape 36
4.3 Role of surface diffusion for the doping of nanowires 40
4.4 Conclusion 43

5 Growth and properties of (In,Ga)As shells on GaAs nanowires by molecular beam epitaxy **45**
5.1 NW core-shell structures . . . 46
5.1.1 Growth of NW core-shell structures . . . 46
5.1.2 Microstructure of core-shell structures . . . 47
5.2 Impact of growth parameters on luminescence properties of (In,Ga)As shells 48
5.2.1 Growth temperature . . . 49
5.2.2 As flux . . . 52
5.2.3 Ga and In flux . . . 53
5.2.4 Discussion of optimum growth conditions . . . 54
5.3 Role of the flux directionality in MBE . . . 56
5.3.1 Growth with different As cells . . . 56
5.3.2 Inherent flux sequences . . . 59
5.3.3 Role of rotation speed and configuration of group III cells . . . 62
5.4 Conclusion . . . 64

6 Impact of outer shell structure and localization effects on charge carrier dynamics in (In,Ga)As shell quantum wells **65**
6.1 Localized states in the (In,Ga)As shell quantum well . . . 66
6.2 Thermal quenching of luminescence intensity . . . 67
6.3 Exciton dynamics in the shell quantum well at low temperature . . . 70
6.4 Conclusion . . . 73

7 Ex-situ annealing of core-shell nanowires **75**
7.1 Description of the annealing process . . . 76
7.2 Impact of annealing process on luminescence properties . . . 78
7.3 Strain in the capped core-shell system . . . 81
7.4 Luminescence properties of the annealed core-shell sample . . . 84
7.5 Conclusion . . . 88

8 Conclusions and outlook **89**
8.1 Conclusions . . . 89
8.2 Outlook . . . 92

Bibliography **95**

List of figures **117**

Acknowledgements **119**

Selbstständigkeitserklärung **121**

1 Introduction

Today's western societies are characterized by rapid transformations due to the digitalization. Now, everybody can access enormous amounts of information and process it with mobile electronics that offer huge computing power and quick data transfer. The rapid development of consumer electronics is to a large part based on progress in solid-state electronics using semiconductor materials which started their breakthrough with the invention of the transistor by Bardeen, Brattain, and Shockley about 70 years ago. Most consumer electronics of today rely on the highly developed Si technology which has been driven by engineering efforts over many decades. Despite its predominance in logic circuits, Si has fundamental disadvantages for high performance electronics, such as its relatively low carrier mobility and indirect band-gap, inhibiting efficient light emission. In contrast, the archetypical compound semiconductor gallium arsenide (GaAs) exhibits higher carrier mobilities and efficient light emission in the near infrared due to its direct band-gap. Furthermore, it forms a versatile material system with its alloys (Al,Ga)As and (In,Ga)As, enabling the realization of functional heterostructures. Therefore, many specialized devices rely on GaAs heterostructures, such as infrared lasers, high-efficiency solar cells, and power amplifiers for wireless communication. A decade old dream of the electronics industry is the monolithic combination of the advantageous properties of GaAs with the mature Si platform. However, the large lattice mismatch and difference in thermal expansion coefficient between Si and GaAs make this heteroepitaxial combination very complicated.[1]

A conceptually facile strategy of integrating these materials is the reduction of their interface area. Vertical one-dimensional nanostructures called nanowires (NWs) exhibit diameters of tens of nanometers, thus facilitating the elastic strain relaxation to the surface and confining plastic relaxation by formation of misfit dislocations to the interface area. Therefore, in the form of NWs, GaAs and other III-V materials can be grown on Si substrates with high structural quality.[2] Furthermore, NWs have attracted attention due to their specific fundamental properties such as the formation of crystal phase quantum structures[3–6] and their enhanced light-coupling characteristics.[7] In recent years, many basic device structures based on GaAs NWs have been realized such as light-emitting diodes (LEDs),[8] lasers,[9] and photovoltaic cells.[10]

To use GaAs NWs as the basis for more complex device structures, they can be combined with other materials forming heterostructures, such as axial segments of its alloys,[11] or quantum dots inside the NW[12] or decorating the NW sidewalls.[13,14] Another promising structure are radial heterostructures in the core-shell geometry, which

have so far been used mostly for surface passivation, and only few studies discuss radial quantum wells.[15,16] Due to its lower bandgap energy compared to GaAs, an (In,Ga)As quantum wells (QWs) is the archetypical system which has been widely explored in the case of planar heterostructures, but in the case of (In,Ga)As shell QWs, only few studies exist so far.[16–19] The lattice parameter of (In,Ga)As increases drastically with increasing In content, leading to plastic relaxation of the strain by the formation of misfit dislocations. Therefore, InP needs to be used as a substrate for planar (In,Ga)As layers with high In contents that emit in the infrared range which is of interest for optical communication using fiber optics. In contrast, for core-shell structures, the small NW diameter results in a new form of strain distribution, where shells grown pseudomorphically around the NW core share the strain with the core. This strain partitioning enables the growth of (In,Ga)As shell QWs with In contents up to 50% without the formation of dislocations.[20] The first LED structures based on such (In,Ga)As shell QWs were realized at PDI before beginning this work,[17] unfortunately showing low luminescence intensities at room temperature. Here, a detailed investigation of the electronic and structural properties was necessary to understand the luminescence properties.

This thesis is devoted to the realization of GaAs/(In,Ga)As nanowire core-shell structures of high quality. To enable efficient LED structures and more complex laser structures,[21] we use GaAs NWs grown on patterned Si substrates as core templates for the shell growth. This selective area growth assures the precise control of the growth processes as shadowing of the molecular beams by neighbouring NWs can be avoided by using arrays with suitable separation between the NWs. This control during NW growth is necessary to obtain the exact NW morphologies that are required for core-shell structures that enable the realization of complex devices. The growth of ordered NW arrays had not been established at Paul-Drude-Institut before starting this project and is part of this work.

Following this introduction, in chapter 2, the experimental methods are presented that have been used for most of this work. A brief introduction to molecular beam epitaxy is given and the specific system that was used in this work is presented. Furthermore, photoluminescence spectroscopy is explained and the two main characterization techniques that have been used are described: The setup used for continuous-wave photoluminescence spectroscopy at varying temperatures and the setup for time-resolved photoluminescence spectroscopy at varying temperatures.

In chapter 3, the vapour-liquid-solid (VLS) growth of semiconductor NWs is discussed in general and the Ga-assisted growth of GaAs NWs is introduced. Following this discussion, we focus on the selective area growth of GaAs NWs. First, we present the processes for patterning substrates and necessary surface preparation techniques for the realization of GaAs NW arrays with high vertical yield. Then, we discuss the impact of the V/III flux ratio on the growth results.

In chapter 4, a two-step growth approach is presented, which enables the growth of untapered NWs with small diameters and high vertical yield. Based on this versatile

growth approach, we show that significant vapour-solid growth on the NW sidewalls contributes to the diameter evolution of the NWs. We derive a growth model that takes into account the diameter variation due to changes of the droplet size and the direct growth on the NW sidewalls. With this model we can precisely describe the shape of entire NWs and use it in a predictive manner to obtain untapered NWs of different length that are required for the growth of core-shell structures. Finally, we explore the role of diffusion processes on the NW sidewall for the doping of NW structures and explain how different dopant profiles might form.

In chapter 5, we introduce the growth of (In,Ga)As shells on GaAs NW cores. First, the general requirements for the conformal growth of shells are discussed and the microstructure of such samples is presented. Then, we show the optimization of the growth temperature, the V/III flux ratio, and the growth rate to achieve (In,Ga)As shell quantum wells with optimum luminescence properties. Subsequently, we concentrate on the role of the flux directionality in MBE for the growth of NW shells. We show that the relative positions of the material sources in the MBE setup has crucial impact on the luminescence properties of core-shell structures. We show that the directionality of the fluxes and the three-dimensional nature of NWs lead to flux sequences on the NW sidewalls and discuss possible explanations for its impact on the luminescence properties.

In chapter 6, we investigate the luminescence properties of the shell quantum wells in more detail. We show that alloy clustering due to the specific growth processes, leads to localization of charge carriers at low temperatures. Furthermore, we explore the impact of different outer shell structures on the luminescence properties at varying temperatures. We show that an AlAs barrier shell with a GaAs spacer shell are necessary to obtain high luminescence intensities over the full temperature range.

In chapter 7, we present a process that enables the ex-situ annealing of NWs at high temperatures. We show that the addition of a SiN_x cap to the core-shell structure prevents the destruction of the material at annealing temperatures of up to 900 °C. Furthermore, we show that the luminescence peak corresponding to the (In,Ga)As shell quantum well narrows and shifts to higher energies, indicating strong homogenization of the alloy and reduction of the alloy clustering that is inherent to the growth process. Finally, we compare the luminescence properties of an annealed sample to the as-grown samples.

In chapter 8, the work is concluded and an outlook is given to future work based on the results presented in this work.

2 Methods for the growth and analysis of GaAs nanowire core-shell structures

In this chapter, the main experimental methods are described that were used in this work for the synthesis of the samples and their optical characterization.

2.1 Semiconductor growth by molecular beam epitaxy

The development of molecular beam epitaxy as a technique for semiconductor growth went hand in hand with the quest for the synthesis of high quality material and novel heterostructures at the beginning of the 1970s.[22] Early on, MBE was developed to grow GaAs layers of high quality[23] and shortly afterwards heterostructures could be realized[24] enabling the experimental investigation of superlattices motivated by theoretical predictions.[25]

The fundamental idea of MBE is to have a directed beam of molecules or atoms impinging on a heated substrate, where they form a crystalline phase. In order to achieve such beams, the atoms must not scatter with other atoms while traversing to the substrate. Therefore, ultra high vacuum conditions are necessary ($p < 10^{-9}$ mbar) which are maintained by multiple pumps. The molecular beams are generated by Knudsen evaporation cells where a crucible holds material of highest purity and is electrically heated to high temperatures. Due to the simplicity of the involved processes compared to vapour phase epitaxy where complex precursor molecules are used, MBE is a versatile tool to explore basic growth phenomena. Here, the growth dynamics are crucially dependent on adatom adsorption and desorption, as well as adatom diffusion and incorporation. These processes are thermally activated and affected by the total and relative material fluxes, which can be precisely controlled in MBE. The low growth rates that can be precisely controlled by the temperature of the evaporation cells even enable the growth of layers with thickness precision of less than a monolayer.

Desirably, the growth of planar layers proceeds in the Frank–van-der-Merwe growth mode, if the lattice-mismatch to the underlying layer or substrate, respectively, is not too large.[26] Here, it is assumed that the initial surface energy is higher than the sum of the surface energy of the new layer and the interface energy of the two layers. The minimization of the free energy then drives the formation of complete layers in layer-by-layer growth. For low growth rates, this layer growth may happen by step-flow growth, where surface adatoms can diffuse to the next step edge where they incorporate without

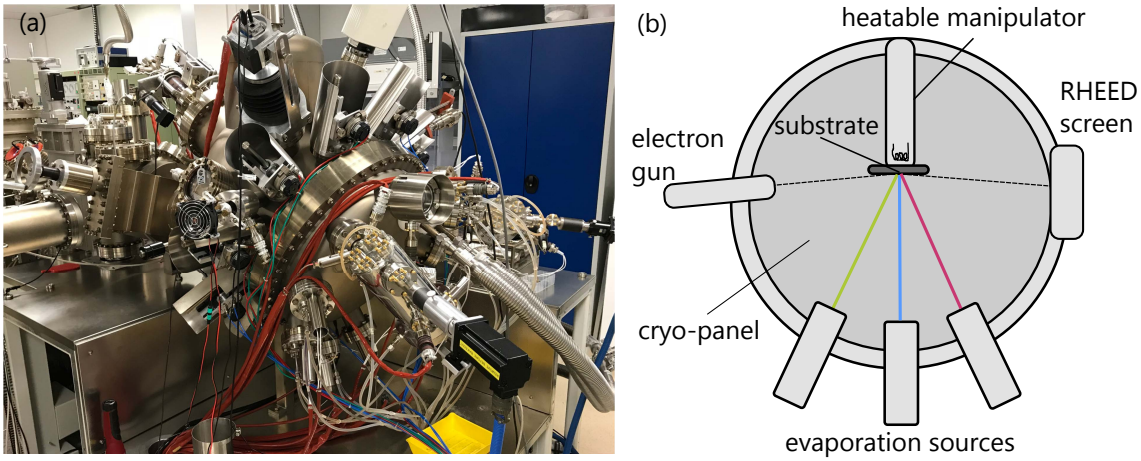

Figure 2.1: (a) Photograph of the MBE setup used for this work. The growth chamber is in the front. (b) Schematic diagram of the growth chamber of a MBE setup.

the formation of a new island on the terrace. This growth mode leads to the formation of very smooth layers.

The UHV conditions also enable the in-situ characterization of the crystalline structure by reflection high energy diffraction (RHEED). With this method, the three-dimensional growth can be monitored and surface reconstructions on layers can be characterized.[27] Unfortunately, the sample holder for the substrates used for most samples of this thesis blocks the RHEED beam from the sample surface. Furthermore, the substrates used in this work contain different fields (cf. 3.2.1) which are smaller than a typical RHEED spot and therefore the measurement would necessarily integrate over many fields, making the results unclear. Therefore, no in-situ characterization technique was used for the growth of NWs in this work.

All samples discussed in the framework of this thesis were grown in the VG V80H MBE system shown in Figure 2.1(a). Substrates are loaded into the UHV system through a bakeable fast entry lock, pumped by a turbomolecular pump. By heating the substrates to 125 °C the ambient water film is removed from the substrate surface. Prior to growth, the substrates are heated in the preparation chamber to 400 °C to remove any remaining residues. The vacuum in the preparation chamber is maintained by an ion pump and a Ti sublimation pump, achieving a base pressure of below 10^{-10} mbar. Figure 2.1(b) shows a schematic diagram of the growth chamber of the MBE setup. Here, the vacuum is maintained by a cryo pump, an ion pump and a Ti sublimation pump. Furthermore, a cryo panel filled with liquid nitrogen lies around the heated cells and the substrate to enhance condensation of residual atoms and molecules at the surface. With this effort a base pressure of below 10^{-10} mbar is achieved. The sample holder in the growth chamber contains a heater with a maximum temperature of 850 °C which can rotate continuously during growth to achieve a good homogeneity for planar samples. The temperature of the substrate on the heater is measured by a pyrometer calibrated to the oxide desorp-

tion temperature of GaAs(100). The material cells are mounted on 10 cell ports, directed onto the substrate under an angle of 33.5° (one port is occupied by a heated window). The exact locations of the sources with respect to each other are discussed in detail in chapter 5.3.2. Sources for Ga, In, Al, Be, and Si are typical Knudsen evaporation cells connected to PID temperature controllers. Additionally, the system contains two sources for As with valved crackers (VEECO 500 CC). The cracker temperature was maintained at 850–900 °C to supply mostly As_2. For the growth of NWs there is only limited information on the role of the As species.[28] All shutters and temperatures are controlled by a software developed at Paul-Drude-Institut, assuring the repeatability of growth experiments.

The material fluxes are measured by an ion gauge which can be moved in front of the sample holder. The obtained beam equivalent pressure needs to be translated to a growth rate or atomic flux to have physically meaningful and repeatable parameters. For the calibration of the group III cells, layers of different alloys — (Al,Ga)As on GaAs(100) and (In,Ga)As on InP(100) — were grown and the growth rate was calculated from the thickness and composition measured by X-ray diffraction measurements. This procedure is valid when the growth of planar III-As layers is As-rich, as needed for smooth layers, and therefore the growth rate depends on the group III material flux. For the calibration of the As flux, we monitored the surface reconstruction of a GaAs(100) layer by RHEED at 580 °C. For As-rich conditions, the surface reconstruction is (2x4), whereas for Ga-rich conditions it is (4x2).[29,30] The 1:1 point for Ga and As fluxes can be found when the As flux is reduced until the surface reconstruction changes gradually at a specific As flux.[31] From the growth rate calibration of the Ga flux, the As flux can be calibrated. This calibration was done for both As cells to have consistent fluxes of the two cells which will be important for the shell growth discussed in chapter 5.3.

In literature, fluxes and growth rates are often given in units of ML/s, which depend on the growth plane of the substrate. In the case of NWs, there are two growth planes, (111)B in axial direction and (110) in radial direction. Therefore, we use a unit for the fluxes that does not depend on the growth plane, which is nm/min. This unit corresponds to the material of one species that is necessary to grow zincblende GaAs of a certain thickness per minute on a planar substrate. When the details of the shell growth on the $(1\bar{1}0)$ sidefacets are discussed in chapter 5, we also refer to the amount of monolayers on the sidefacets. The GaAs(110) plane has a surface density of Ga atoms of $S_{(110)} = 2\ \mathrm{at}/\sqrt{2}a_{\mathrm{GaAs}}^2 = 4.426\ \mathrm{at/nm^2}$, with the lattice constant of GaAs $a_{\mathrm{GaAs}} = 0.565$ nm. The density of Ga atoms in the GaAs matrix is $\rho = 4\ \mathrm{at}/a_{\mathrm{GaAs}}^3 = 22.22\ \mathrm{at/nm^3}$. Consequently, a monolayer of GaAs on the (110) plane has a thickness of $d_{110} = S/\rho = 0.199$ nm and a growth rate of 1 nm/min corresponds to 0.084 ML/s on the (110) plane. For the exact growth rate on the sidefacet one needs to take into account the substrate rotation and the tilting of the sources with respect to the substrate normal ($\beta = 33.5°$). One finds that the flux on the sidewall is $f_{\mathrm{SW}} = \tan(\beta)/\pi \cdot f_{\mathrm{planar}} \simeq 0.21 \cdot f_{\mathrm{planar}}$ where f_{planar} is the flux incident on the substrate plane. Consequently, a planar flux of 9.5 nm/min corresponds

to one monolayer on the (110) NW sidefacets.

2.2 Photoluminescence spectroscopy

For the investigation of the electronic properties of semiconductors with direct bandgap, luminescence spectroscopy is a powerful tool. This part on the presentation of the involved processes is based on the description in chapters 6 and 7 of the book by Yu and Cardona.[32] A luminescence process comprises three separate steps: Excitation, thermalization, and recombination, as visualized in Figure 2.2. First, a non-equilibrium distribution of electron-hole pairs is excited externally. In the case of photoluminescence, this is done by photons of a laser beam with the energy $\hbar\omega_{\mathrm{exc}}$ (blue arrow in Figure 2.2). Then, the electron and hole reduce their energy by the emission of optical and acoustic phonons, indicated by the arrows corresponding to longitudinal optical (LO) phonons in Figure 2.2, having a phonon energy of about 36 meV for GaAs at low temperatures.[33] The corresponding phonon-carrier interaction times can range from 0.1 ps to tens of ps. As these thermalization processes are much faster than the necessary time it takes electrons and holes to recombine, it is assumed that the electrons and holes adopt quasi-equilibrium distributions around the minima of the energy bands, which is at the Γ-point for direct semiconductors like GaAs and (In,Ga)As. At this thermal equilibrium, the carrier population decreases exponentially with increasing energy, which makes luminescence experiments a sensitive probe for low-lying energy levels. Furthermore, the thermalization process separates the excitation process and the emission process, and thus, removing the correlation between the two. In special cases, this thermalization process may be incomplete, resulting in emission of photons from electron-hole pairs with higher energy, a phenomenon called hot luminescence.

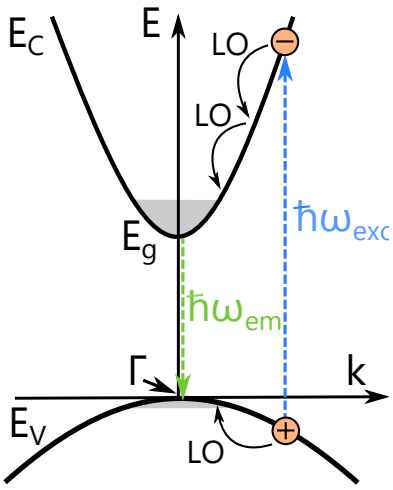

Figure 2.2: Diagram showing the different steps in a luminescence process: the excitation process of electron hole pairs by the absorption of a photon with energy $\hbar\omega_{\mathrm{exc}}$ (blue), the relaxation to the band edge by emission of phonons, and the recombination producing an emitted photon with energy $\hbar\omega_{\mathrm{em}}$ (green).

Finally, the thermalized electron-hole pairs recombine spontaneously if no strong external field is present to induce stimulated emission. The emission only depends on the band structure and energy levels of the sample. If the semiconductor material has a direct band-gap and electric dipole transitions are allowed, electron-hole pairs recombine radiatively. For semiconductors with indirect band-gap, such as Si, electrons will thermalize in the indirect conduction band valley at high k values. Recombination of these

electrons with holes is impeded, as the momentum of a generated photon is not large enough to assure conservation of momentum, and many phonons need to be involved in the recombination process. However, in direct semiconductors, free electrons and holes recombine with the radiative recombination time τ_{rad}. Furthermore, defects leading to deep-centers within the band-gap or surface states may lead to nonradiative recombination characterized by the nonradiative lifetime τ_{NR}.

At low temperatures, shallow impurities are not completely ionized and trap charge carriers. These trapped carriers can recombine with free carriers, leading to emission of photons with reduced energy compared to band-to-band emission discussed before. GaAs grown by MBE typically contains significant amounts of carbon atoms, acting as acceptors resulting in a characteristic transition of holes bound by the carbon acceptors and free electrons. Beyond that, more specific shallow electronic levels within the band-gap exist resulting in emission at various energies, such as donor-acceptors pairs.

For semiconductor samples of high purity and high quality, electron-hole pairs are attracted by the screened Coulomb interaction and form Wannier excitons at low temperatures. Here, the electron and hole form a bound state with a center-of-mass motion and a reduced mass μ. In the effective mass approximation of the electronic band structure around the Γ-point, one can calculate the binding energy in the ground state similar to the procedure for the hydrogen atom and obtains

$$E_{\mathrm{b}} = \frac{\mu e^4}{32\pi^2\hbar^2\epsilon_0^4} = \left(\frac{\mu}{m\epsilon_0^2}\right) \times 13.6\ \mathrm{eV}, \tag{2.1}$$

where e is the electron charge, $\hbar$ is Planck's constant, and ϵ_0 is the low-frequency dielectric constant of the semiconductor. If the hole mass is much larger than the electron mass as it is the case for many semiconductors like GaAs, the reduced mass μ is close to the hole mass. Then, the binding energy of an exciton is similar to the donor binding energy. For GaAs, the binding energy according to Equation 2.1 is 4.7 meV ($m^*_{\mathrm{el}}/m = 0.067$, $m^*_{\mathrm{ho}}/m = 0.5$ and $\epsilon_0 = 13.1$) which is close to reported experimental values. The exciton Bohr radius is $a_0 = 112$ Å, which is a measure of how far the exciton wavefunction extends within the lattice. In a semiconductor of high quality, the light that was generated by the recombination of an exciton may generate excitons again. This process happens continously and it cannot be distinguished between light and excitons in the materials, therefore it can be treated as a coupled state called exciton-polariton. The energy of extracted photons generated by exciton-polaritons is reduced by the exciton binding energy compared to the energy of photons due to band-to-band recombination of free carriers. Similar to these, excitons can also be bound to shallow defects and localization sites in quantum wells, which can be alloy clusters or regions with larger QW thickness.

Continuous-wave photoluminescence spectroscopy

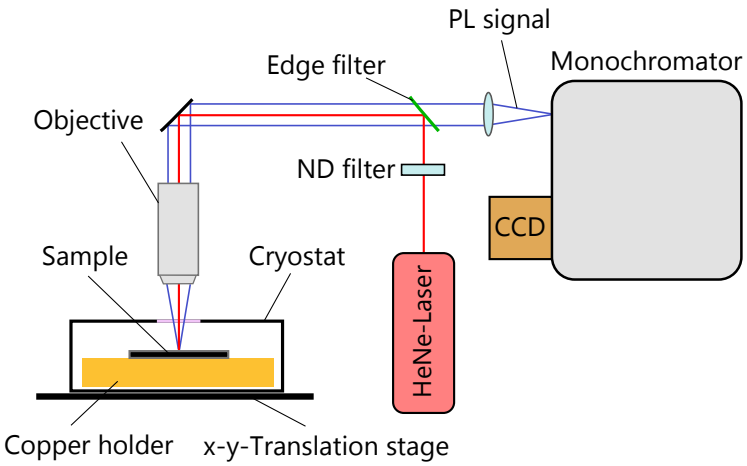

Figure 2.3: Schematic diagram of µ-PL setup. Figure based on diagram from PhD thesis of Christian Hauswald.[34]

In continuous-wave photoluminescence (cw-PL) spectroscopy, the excitation of charge carriers in the material and the measurement of the generated PL signal proceeds continuously. Here, the charge carrier distribution is in a steady-state. Figure 2.3 shows a diagram of the HORIBA JOBIN YVON LABRAM HR 800 UV µ-PL setup which was used for all cw-PL measurements presented in this thesis. For excitation, a Helium-Neon (HeNe) laser is used, emitting at a wavelength of 632.8 nm, corresponding to the transition energy in Ne atoms. The laser power can be decreased by inserting neutral density optical filters into the optical path. The beam is deflected by mirrors and an edge filter to a microscope objective, which focuses the light onto the sample. The luminescent light from the sample is collected by the same objective as used for excitation. At the edge filter a part of the signal is not deflected and enters the monochromator. Here, a grating with 600 grooves/mm is used to disperse the light which is then detected by a liquid Nitrogen-cooled Si charge-coupled device (CCD) with 1024 x 256 pixels. The sample itself is mounted inside a continuous-flow cryostat. A flow of liquid He in combination with a PID controlled heater element in the cryostat maintain a constant temperature between 10 K and 300 K. The cryostat is mounted on an electric translation stage for localization of the specific location on the sample.

The setup contains dispersive optical elements such as the microscope objective. Furthermore, the sensitivity of the Si CCD detector depends on the wavelength of the incoming light and decreaseses strongly for photon energies close to the Si band-gap energy.[35] Therefore, the measured spectra need to be corrected for the system response to obtain comparable intensities and peak shapes at different wavelengths. In this context, we measured the broad thermal emission of a quartz tungsten halogen reference lamp (BENTHAM CL2), and divided the measured spectra by the nominal values provided by the manufacturer. Figure 2.4 presents the obtained attenuation factor of the PL signal as

a function of wavelength. This curve was used to correct all cw-PL spectra presented in this thesis. It shows that for detection wavelengths above 950 nm the PL signal is attenuated by more than an order of magnitude. In order to assure a reasonable intensity in the PL investigations, we concentrated on (In,Ga)As shells with moderate In contents of 15%, corresponding to an unstrained band-gap energy of 1.299 eV ($\lambda = 955$ nm).

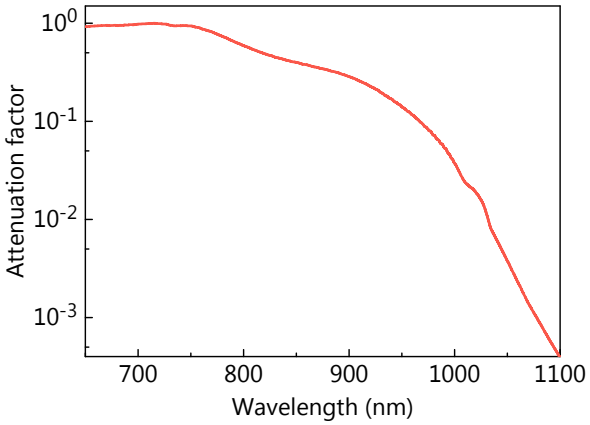

Figure 2.4: Attenuation factor of the PL signal as a function of wavelength due to the system response.

The microscope has a numerical aperture of 0.25 and a magnification of 10×, leading to an estimated spot size of about 5–10 µm in diameter. As the spot size is not well known, we did not attempt to calculate the excitation density but only state the excitation power. However, we estimate that for the mentioned spot sizes the typical excitation densities used in this thesis are well below 540–8700 W/cm^2 (for a maximum excitation power of 1.7 mW). Furthermore, we assume that an ensemble of NWs is measured. For the mentioned spot sizes and NW arrays with separation of 1 µm and a vertical yield of 60% we expect that 18–73 NWs are measured simultaneously.

Time-resolved photoluminescence spectroscopy

In time-resolved PL spectroscopy, charge carriers are excited by a light pulse and the luminescence signal is measured as a function of delay time. Thereby, the charge-carrier dynamics can be investigated. Figure 2.5 shows a schematic diagram of the setup for time-resolved photoluminescence experiments used in this thesis. A COHERENT VERDI solid-state laser with wavelength of 532 nm pumps a COHERENT MIRA 900 Ti:Sapphire laser. The laser is tuned to a central wavelength of 750 nm and emits pulses with a duration of 200 fs and repetition rate of 76 MHz. The laser pulses are generated by passive mode-locking in the laser cavity. A Kerr-lens focuses intense pulses onto a pinhole, whereas less intense continuous light is not focused and attenuated by the pinhole. Thereby, only intense pulses remain in the cavity. These pulses are composed of many longitudinal modes with a fixed phase relationship. The pulsed laser light is focused onto the sample by the same objective used for cw-PL. By moving a set of mirrors and the objective on a x-y stage one can direct the laser beam onto different locations on the sample. The emitted light is collected by the same objective and directed to the monochromator. Here, a grating with 300 lines/mm disperses the light spectrally, which is detected by a HAMAMATSU C5680 streak camera in syncroscan mode.

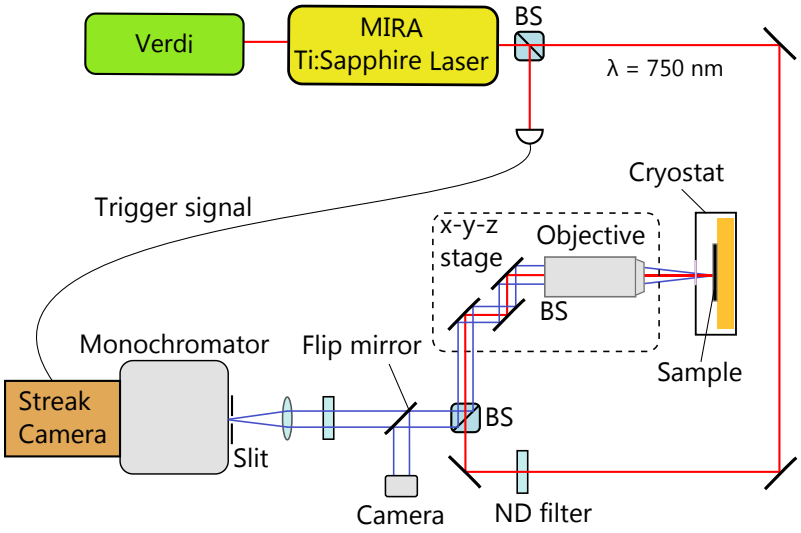

Figure 2.5: Schematic diagram of the time-resolved PL setup. Figure based on diagram from PhD thesis of Christian Hauswald.[34]

The streak camera consists of a cathode tube with photocathode and phosphor screen. The spectrally dispersed light generates electrons in the photocathode which travel through the cathode tube. The spectral dispersion is maintained in vertical direction to the electron beam. The electrons are deflected along the vertical direction normal to the spectral plane by an electric field generated by a sawtooth voltage applied to the deflection electrodes. The voltage is generated by a sweep-curve circuit which is triggered by a photodiode detecting the pulsed laser signal extracted from the beam path by a beam splitter (BS). After traversing the tube, the electrons hit the phosphor screen and the generated light is detected by a camera. Thereby, temporal and spectral information of a stream of light is transferred into spatial information on the screen. A resulting spectrum is shown in Figure 2.6. Here, the PL intensity is shown according to the colormap on the left. The delay time is given as the y-axis and the photon energy as the x-axis. Such a two-dimensional spectrum is imaged by the camera on the phosphor screen and can be understood as a series of separate spectra taken at different times.

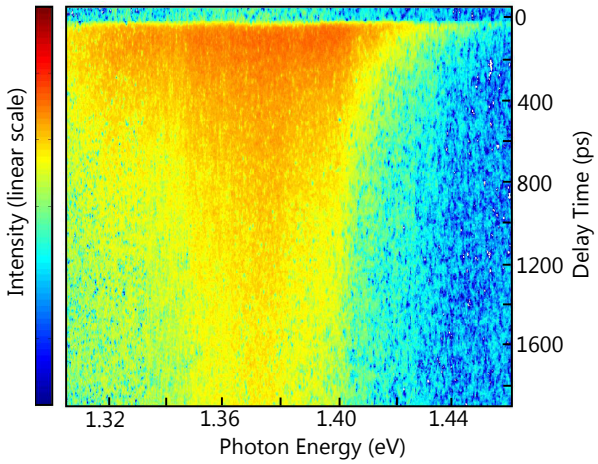

Figure 2.6: Time-resolved PL of a GaAs/(In,Ga)As core-shell sample discussed in chapter 6.3. Here multiple single spectra are added to obtain a spectrum over a larger spectral range.

3 Selective area growth of GaAs nanowires on patterned Si substrates

Various techniques have been used to synthesize GaAs NWs such as MBE[36,37] and metalorganic vapour phase epitaxy (MOVPE).[38] In research, the most popular method for fundamental growth studies is MBE, as complex pre-cursor materials can be avoided and the UHV conditions assure highest purity. For growth by MBE, the Ga-assisted growth approach is a particularly clean method as no external catalyst materials are necessary and thus it has become a major technique for the exploration of the growth of GaAs NWs. In this chapter, we introduce the Ga-assisted growth of GaAs NWs by MBE with a focus on selective area growth (SAG) on patterned substrates, which has been of great interest in recent years.[39–43] Despite much progress, realizing a high vertical yield, i.e. ratio of vertical NWs to holes in the mask, remains challenging. Often, NWs form at the desired position but do not elongate perpendicular to the substrate or even crystallites form instead of NWs. Vertical yield values vary significantly among different studies[39,44] because the yield depends not only on growth parameters[42,44] but also critically on mask processing conditions.[40,41] Here, we investigate in particular the impact of the surface preparation and the V/III ratio on the growth of vertical NWs. These results will be the basis for all growth experiments discussed in this thesis.

In section 3.1, we review the development and current state of GaAs NW growth with particular emphasis on growth by MBE. The vapour-liquid-solid growth mode is explained and the Ga-assisted growth approach for GaAs NWs is motivated. Finally, we discuss distinct features of NWs that make them particularly interesting for growth experiments, i.e. the beneficial strain distribution and the formation of materials in the wurtzite crystal structure that typically exist only in zincblende structure.

In section 3.2, the processing of substrates for SAG using electron beam lithography and dry etching is explained and the mask design is presented. On the basis of the processed substrates, the impact of different surface preparation procedures is explored. It is shown that rinsing the substrate in boiling ultrapure water increases the vertical yield drastically. Different methods are used to understand the impact on the surface itself. Finally, we discuss the growth of NWs by SAG in more detail and explore the impact of the V/III ratio on the vertical yield of NW arrays.

In section 3.3, the growth of NWs with high vertical yield gets transferred to substrates patterned by nano-imprint lithography, making the growth of large arrays of NWs feasible.

Parts of this chapter have been published in H. Küpers *et al.*, *Semicond. Sci. Technol.* **32** 115003 (2017)[45] and H. Küpers *et al.*, *Nano Research* (2018)[46].

3.1 Growth of GaAs nanowires

The intentional growth of semiconductor NWs was first observed by Wagner and Ellis in 1964.[47] Their study introduced the vapour-liquid-solid (VLS) growth method which is now a popular approach used in many NW growth experiments. Here, material is present in three thermodynamic phases: The vapour phase represents the source of material, the molecular beam in the case of MBE. The vapour is collected by a liquid particle and incorporated into it as a solute. An increase of the concentration of growth species in the droplet leads to supersaturation of those atoms in the droplet. Consequently, the dissolved material crystallizes and forms a solid phase below the droplet, leading to the growth of one dimensional nanostructures. After the first realization of Si NWs,[47] VLS NWs consisting of many other semiconductor materials have been synthesized, such as ZnO, Si_xGe_{1-x}, and GaN among others.[48]

Also for the archetypical compound semiconductor GaAs, the growth of nanowhiskers and nanowires was explored.[49] Initially, the samples were grown using a Au nanoparticle as droplet.[50] For vapour phase methods like MOVPE, the droplet acts as a catalyst in cracking the metal-organic pre-cursor molecules. Therefore, MOPVE growth approaches, apart from vapour-solid NW growth,[51] strongly rely on Au catalysts but also other foreign metal catalysts have been introduced,[52] such as Ag[53] and Sn.[54] However, many metals – Au in particular – are known to act as a deep states in many semiconductors, which is detrimental for their respective electric and optical properties.[55] Consequently, a degrading effect of the Au droplet on the general cleanliness of the MBE system and the NW characteristics in particular was expected, which was later put into perspective.[56,57] However, in 2008 two groups reported the succesful growth of GaAs NWs under a Ga droplet, thus avoiding any external catalyst material.[36,37] Within the past 10 years, this Ga-assisted growth approach has become very successfull for the growth of NWs and most GaAs NW samples grown by MBE are based on this growth approach today. Recently, the Ga-assisted growth has also been used successfully to grow GaAs NWs in MOVPE[58] and hydride vapour phase epitaxy.[59] Furthermore, it was found that the low solubility of As in the Ga droplet leads to nucleation anti-bunching of new monolayers, which results in a high homogeneity in the length of NW ensembles,[60,61] an important but more subtle advantage of the Ga-assisted growth approach.

Figure 3.1(a) and (b) illustrate the VLS growth of GaAs NWs in the Ga-assisted approach. Here, molecular fluxes of Ga and As_2 are supplied in the vapour phase. The adatom diffusion length of Ga on native oxide covered Si substrates is on the order of hundreds of nanometers, which is smaller than on bare Si surfaces. Still, the collectiono of Ga from a large area on the surface leads to the nucleation and formation of Ga droplets,

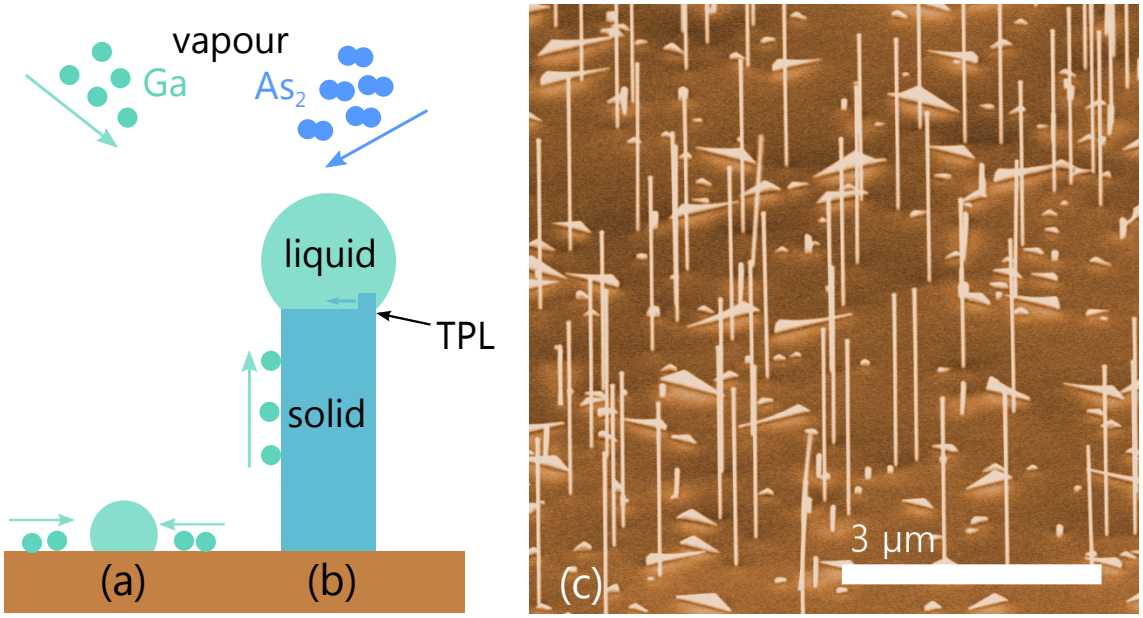

Figure 3.1: Description of the Ga-assisted VLS growth: (a) Ga atoms form droplets due to large surface diffusion length. (b) The droplet accommodates As and Ga, leading to the growth of solid GaAs. The large supply of Ga by diffusion on the sidefacets is indicated by the green arrow. (c) SEM image of GaAs NWs grown on a Si substrate covered by a thin native oxide. The growth conditions are $T_{\mathrm{growth}} = 630\,^{\circ}\mathrm{C}$, f_{Ga} =1.9 nm/min, and $R_{5/3} = 7$. The detailed growth procedure is described elsewhere[62]. The Ga droplet is hardly visible due to the thin NW diameter of 30 nm. The sample is tilted by 25° from the substrate normal. Micrograph acquired by Anne-Kathrin Bluhm.

as shown in Figure 3.1(a). The density of the droplets in combination with randomly occuring pinholes in the oxide layer determine the density of forming objects.[63,64] These pinholes provide the connection to the crystalline substrate, where crystalline GaAs is nucleated when the As concentration in the Ga droplet has reached a critical value for supersaturation. By continued growth below the droplet the NW forms as shown in Figure 3.1(b). GaAs NWs typically grow in the $\langle\bar{1}\bar{1}\bar{1}\rangle$B direction and form six $\{1\bar{1}0\}$ sidefacets. The high surface diffusion of Ga on these NW sidefacets leads to a large supply of Ga atoms to the droplet. In contrast, it is assumed that As does not diffuse on the surface but desorbs immediately. Additionally, a secondary source of As by re-desorption from the substrate has been shown to increase the As supply at the droplet.[65] Consequently, only As that impinges on the droplet and gets accommodated contributes to growth. Due to this discrepancy of the two species, the effective V/III ratio at the droplet is much smaller than the nominal ratio corresponding to the fluxes. Therefore, V/III flux ratios well above one can be used to grow NWs while maintaining a liquid Ga droplet. Figure 3.1(c) shows a micrograph of a typical GaAs NW sample grown on a native oxide covered Si(111) substrate in the Ga-assisted growth mode. The NWs have a length of several µm and widths of around 30 nm, underlining the high aspect ratio.

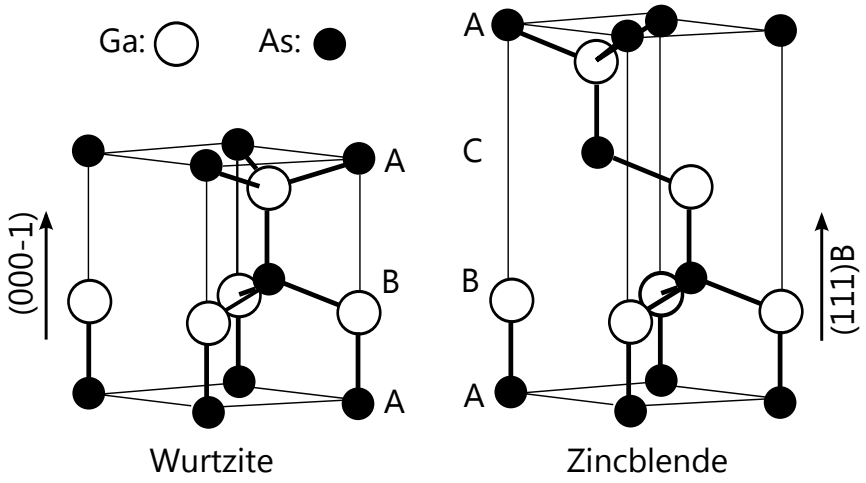

Figure 3.2: Ball and stick model of the wurtzite and zincblende structure with indicated stacking sequence. The thick sticks represent bonds and the thin lines visualize the unit cell.

The small diameter of NWs enables the heteroepitaxial growth on foreign substrates. Strain due to the lattice-mismatch can relax either elastically at the surface or relax plastically via dislocation formation which is confined to the interface and bottom part of the NW.[66–69] This property enables the growth of GaAs NWs on Si substrates without the formation of extended defects,[2,70] despite the large lattice mismatch of 4.1% and thermal expansion coefficient mismatch of 60% which complicates the growth of planar GaAs layers on Si.[71–73] This material combination is desirable as it enables the integration of active photonic components based on III-V materials with the silicon platform, supplying logic circuits. Therefore, all samples discussed in this thesis and most of the III-As NW samples synthesized at the Paul-Drude-Institut are grown on Si substrates.

Most III-V compound semiconductors (except Nitrides) are known to form in the cubic face-centered zincblende crystal structure.[74] In contrast, in the form of NWs these materials can adopt the wurtzite crystal structure, either in the form of short axial segments or spanning the entire NW.[51,75–77] Also rotational twins and stacking faults are often observed in NWs. Figure 3.2 shows the wurtzite structure and the zincblende structure in a ball and stick model, where the black balls are Ga atoms and the white balls are As atoms. Typically, the two structures are characterized by their respective stacking sequence of (111) planes in the three available positions on top of each other as indicated by the letters in Figure 3.2. For the wurtzite structure, the stacking is ABABAB...and for the zincblende structure ABCABCABC.... Based on this stacking order one can also distinguish stacking faults and twin-planes, two planar defects that often exist in NWs. For stacking faults, a plane is skipped leading to a stacking sequence of ABCA<u>BA</u>BC..., which appears like a monolayer of wurtzite in the otherwise zincblende crystal. Twin-planes are characterized by a stacking of ABCAB<u>CB</u>A...where the stacking order is reversed. All these defects form normal to the typical NW growth direction and extend

over the entire NW cross-section.

The formation of polytypic material is inherent to the VLS growth mode where the nucleation of new monolayers below the droplet is assumed to start at the edge.[78] Here, the nucleus faces the TPL of vapour, liquid and solid. Depending on the wetting angle of the droplet on the NW top, this boundary has a different shape affecting the surface energy of a nucleus formed at the TPL and determining whether nuclei form preferentially in the zincblende or the wurtzite structure.[77,79] More recently, the presence of an edge facet was shown by in-situ TEM techniques.[80] For certain droplet sizes or wetting angles, respectively, these edge facets have been observed which lead to the preferential formation of zincblende nuclei in the center of the growth plane instead of wurtzite nuclei at the TPL. The droplet size and wetting angle, both depend on the growth conditions, particularly the V/III flux ratio,[77] enabling the control of the crystal structure. This formation of polytypic NWs leads to many novel discoveries, as the materials show different electronic properties, most notably different band gaps and band offsets, resulting in complex electronic structures. Such crystal phase quantum structures give rise to emission over a wide range of energies.[3–5,81,82]

3.2 Growth of GaAs nanowires on substrates patterned by electron beam lithography

As we discussed previously, for the growth on native oxide, the formation of NWs depends on the density of nanoholes in the oxide layer which are randomly positioned as exemplified by Figure 3.1(c). However, for many applications, controlling the position of the NWs on the chip is essential. One prominent approach is SAG in the holes of a patterned mask, which is defined in sputtered or thermal silicon oxide layers using advanced lithography methods.[39–43] Due to the low sticking on the oxide surface, growth is confined to the nano-holes. Similar to growth on native oxide covered substrates, a Ga droplet is formed which accommodates As, leading to VLS growth of NWs. The major differences are the nature of the mask surface and the interface of the droplet to the bare Si substrate inside the mask hole, both having a crucial impact on the growth results as we will discuss in this section.

3.2.1 Pattern processing by electron beam lithography

For all samples that are presented in this thesis except in chapter 3.3, substrates were patterned by electron beam lithography (EBL). First, 100 nm of positive EBL resist is spin-coated on 2" and 3" Si(111) wafers covered with a 15–20 nm thick thermal silicon dioxide (SiO_2) layer. The oxide thickness is measured precisely for every substrate by spectroscopic ellipsometry, to determine the correct etching time at a later step. Then, the pattern is written in an EBL system (Both steps done by Mathias Matalla at Ferdinand-Braun-Institut). Here, a focused electron beam is directed onto the wafer and leads to

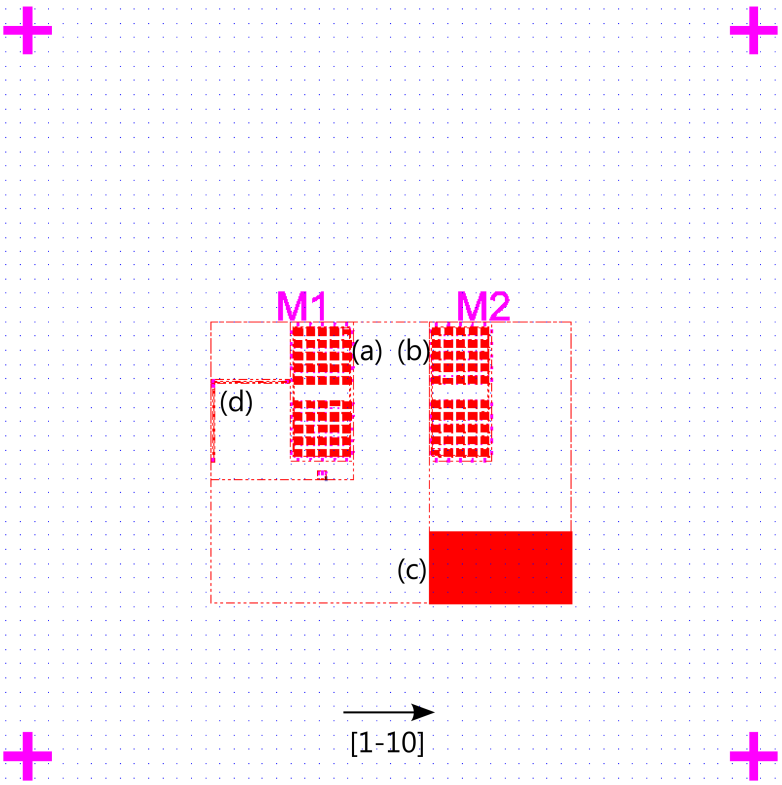

Figure 3.3: Mask outline of a single 10 mm x 10 mm substrate. The crosses mark the corners of the chip. The mask contains (a,b) two matrixes of arrays with different hole sizes and separations, (c) a 1 mm x 2 mm field with 1 µm separation, and (d) two lines of holes with 10µm separation.

cross-linking of the polymer chains in the intended areas. Subsequently, the resist is developed and the oxide mask is etched by reactive ion etching using CHF_3 to avoid underetching effects (Done by Bernd Drescher at PDI). Finally, the wafers were cut into square pieces with an edge length of 10 mm and cleaned by organic solvents, oxygen plasma and UV ozone. With this procedure we achieve 9 (29) highly comparable substrate pieces per 2" (3") wafer (Final cutting and cleaning done by Sander Rauwerdink). Immediately before loading into the MBE system, the surface of the substrate was prepared by a wet chemical treatment which will be described in detail in the next section.

Figure 3.3 shows the mask outline of a single substrate piece. The small square fields, (a) and (b), located below the markers ("M1/M2") have a size of 100 µm x 100 µm. They contain hexagonal arrays of holes with separations ranging from 0.1 to 10 µm and minimum hole diameters of 40–50 nm, organized in a 5 x 10 matrix. This matrix of arrays exists twice. Furthermore, the substrates contain a 1 mm x 2 mm large field (c) located at the bottom right side with a hole spacing of 1 µm and size of 40 nm for XRD measurements with a conventional lab setup. On the left side (d), two 1 mm long lines of holes with separation of 10 µm exist for measurements of single NWs with X-ray synchrotron beams in grazing incidence. The mask is aligned to the substrate orientation such that it

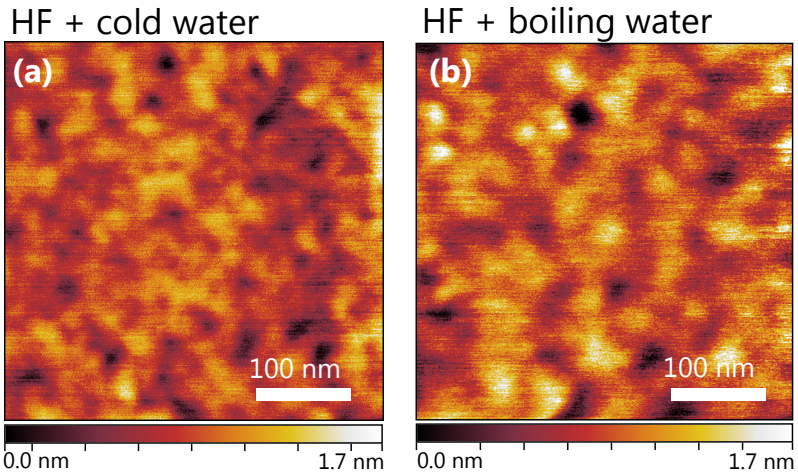

Figure 3.4: AFM micrographs of Si(111) surfaces treated with (a) HF and cold water and (b) HF and boiling water following the rinse in cold water. In both cases the measurement was carried out in large marker areas of a patterned substrate where the thermal oxide had been removed before the wet treatment. RMS roughness values are 0.19 nm and 0.17 nm, respectively. Reprinted from Küpers *et al.* [45].

can be cleaved along the $\langle 1\bar{1}0 \rangle$ direction into two pieces exhibiting identical field matrices and either the single NW line or XRD field for different characterization methods.

3.2.2 Impact of surface preparation on vertical yield

Many research groups struggle with a low reproducibility of the vertical yield of GaAs NWs in selective area growth by MBE (private communication). One reason is the limited understanding of the initial nucleation of NWs at the substrate-droplet interface. Here, the initial GaAs nucleus forms below the Ga droplet at the Si surface. The different phases and interfaces involved make it a complex system which determines the initial growth of the nucleus into a NW or other objects. A way to change this interface is the exploration of different surface treatments of the Si(111) surface prior to growth. In general, fluoride acid solutions are employed to remove the native silicon oxide in the mask openings. Aqueous solutions of HF have been reported to produce atomically rough Si(111) surfaces.[83,84] The surface is oxide free but small Si islands are present with di- and trihydrides saturating the dangling bonds of the Si atoms at the edges of the islands. These edges are selectively etched in etching solutions with a higher pH value, as for example ammonium fluoride (NH_4F), leading to an atomically flat surface.[84] A similar effect is achieved by boiling the sample in oxygen-free water for up to 10 min where OH^- ions attack the Si backbonds:[85] It was reported that this treatment leads to a Si(111) surface which is completely terminated by mono-hydrides,[86] and the smoothness of the surface on an atomic scale was confirmed by scanning tunneling microscopy.[87]

Figure 3.4 presents the surface topography of etched Si(111) substrates as measured by atomic force microscopy (AFM) on patterned substrates after etching in 1% HF solution

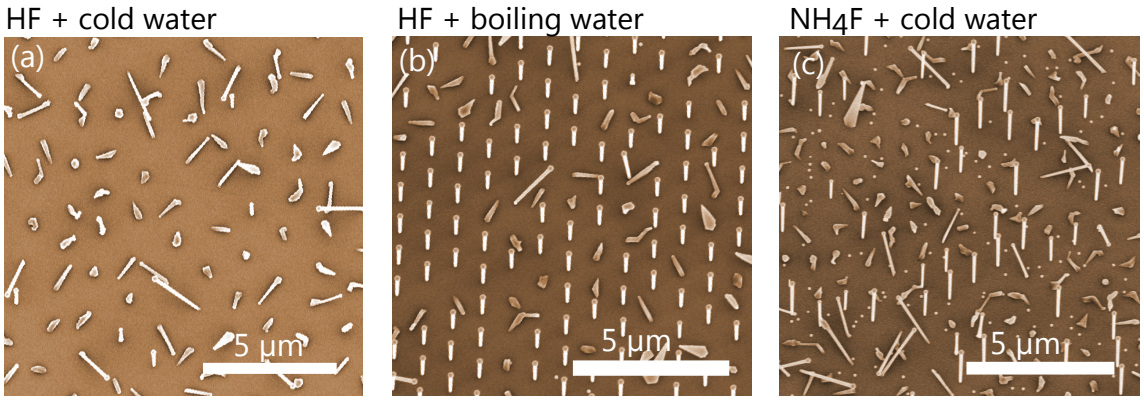

Figure 3.5: SEM micrographs comparing NW samples grown on substrates patterned by EBL and exposed to different surface treatments prior to growth: (a) HF and cold water, (b) HF and cold and boiling water, and (c) NH_4F and cold water. The vertical yield increases from below 5% to 65% with the addition of the boiling water treatment. For the sample treated with NH_4F the vertical yield is 25%. The viewing angle for all micrographs is 15° from normal. Reprinted from Küpers *et al.* [45].

for 60 s and rinsing with (a) cold (20 °C) water and (b) cold and subsequently boiling (100 °C) water. The root-mean-square roughness values are 0.19 nm and 0.17 nm, respectively. We cannot assume this difference to be significant due to the resolution limit of the setup. Even though we cannot access the atomic roughness by AFM measurements, the sample with the boiling water rinse shows a larger feature size (average equivalent square size is 31.2 nm in (a) and 38.0 nm in (b) as calculated by a segmentation grain analysis using *gwyddion*). These larger islands are consistent with a smoother surface for the boiled sample.

In order to explore the impact of such surface treatments on NW growth, different treatments were carried out before loading the samples into the MBE system. Figure 3.5 shows scanning electron microscopy (SEM) images of samples after growth for substrates pre-treated with: (a) HF (1%) for 60 s with 3 min cold (20 °C) water rinse, (b) HF (1%) for 60 s with 3 min cold (20 °C) water rinse and 10 min hot (100 °C) water rinse, and (c) NH_4F (40%) for 120 s with 3 min cold (20 °C) water rinse. Prior to growth, substrates were annealed in the growth chamber at around 680 °C for 10 minutes, after which the temperature was lowered to the growth temperature of 630 °C. Ga was pre-deposited at a flux of 8.5 nm/min for 90 s. Subsequently, NW growth was initiated by supplying Ga and As_2 simultaneously at a V/III ratio of 2.4. The growth time was 15–30 min, after which all sources were closed and the substrate was ramped to 100 °C. In Figure 3.5(a), the vertical yield is below 5% with most holes occupied by tilted NWs or crystallites. However, the growth is restricted to the holes and the oxide surface seems to be free of residues. Figure 3.5(b) shows that adding a boiling water rinse in addition to the cold water rinse leads to a drastic increase in vertical yield to 65%. Figure 3.5(c) shows another sample which was grown on a wafer etched in NH_4F instead of the HF dip (no boiling water). This sample also exhibits an increase in vertical yield to 25%. However, many

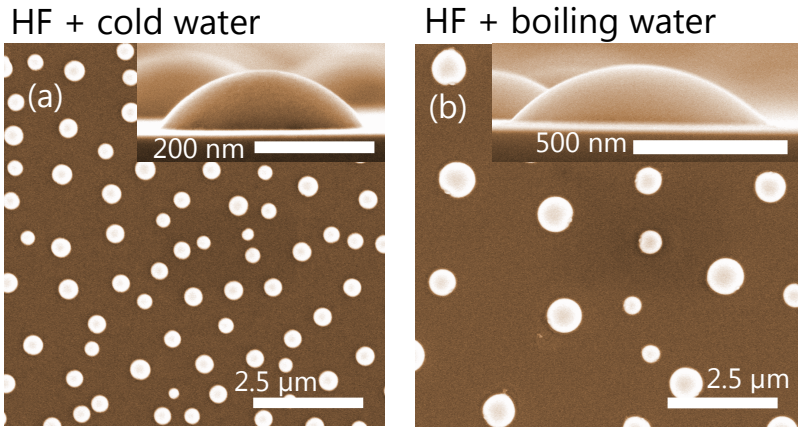

Figure 3.6: SEM top-view micrographs of Ga droplets deposited on unpatterned Si(111) substrates with different surface treatments: (a) HF and cold water and (b) HF, cold water and boiling water. Insets: SEM micrographs in side-view, showing a contact angle of 50° and 45°. Reprinted from Küpers *et al.*[45].

droplets are present on the oxide surface indicating the presence of residues. Furthermore, the NWs of this sample have different lengths. Results from earlier experiments suggest that incompletely etched holes lead to the inhomogeneous length distribution. Here it may result from the low etching rate of the solution. The NH_4F etching leads to a smoother surface but was reported to leave insoluble salt residues on the surface.[88] These residues may be the reason for the accumulation of material on the oxide surface as seen in Figure 3.5(c).

Previously, it was reported for NW growth on unpatterned substrates that the contact angle of droplets on the substrate surface can have a significant impact on the nucleation of NWs.[89] In order to check if the here presented surface treatment changes the contact angle we deposited Ga droplets on unpatterned Si(111) substrates in a similar fashion as has been done in the mentioned study. Even though we assume that the hole in the oxide mask has a significant impact on the shape of the Ga droplet, here, we are interested in the surface properties of the Si substrate. This effect will be similar on a bare substrate and in an etched hole and therefore we can use unpatterned substrates for this experiment. Figure 3.6 shows SEM top-view micrographs for samples with different surface treatments: (a) 1% HF for 60 s and rinsing in cold water and (b) 1% HF for 60 s and rinsing subsequently in cold and boiling water. The mean droplet diameter increases from 390 $\pm$ 50 nm to 620 $\pm$ 210 nm using boiling water and the density decreases from 0.92 µm^{-2} to 0.21 µm^{-2}. The larger separation and size of the droplets indicate a longer surface diffusion length of Ga atoms on the Si surface for the substrate rinsed in boiling water, which is consistent with a smoother surface due to the hot water treatment. The insets of Figure 3.6 show side-view micrographs of Ga droplets after the deposition. The contact angle is similar for the two samples (approximately 50° and 45°). These values are in agreement with the reported values for an oxide free surface.[89] Thus, the observed

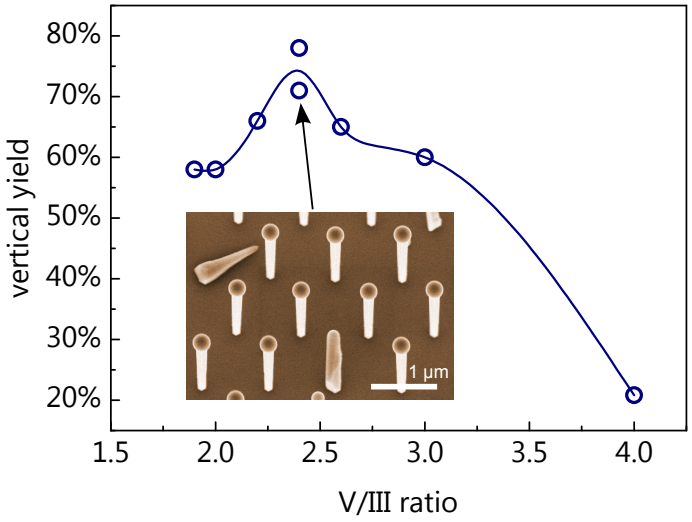

Figure 3.7: Vertical yield for varying V/III flux ratio. The maximum is at 2.4 and for higher V/III ratios the vertical yield decreases drastically. Inset: SEM image of a sample grown with optimum V/III ration. The sample is tilted by 15°. Reprinted from Küpers *et al.*[46].

increase in vertical yield does not correlate with a significant change in contact angle. Consequently, NW nucleation cannot be understood by only investigating the contact angle and the underlying surface energies. Furthermore, our results are in agreement with the hypothesis that reducing the atomic-scale roughness leads to an improved vertical yield. We suppose that an atomically rough substrate surface may lead to a high density of initial nuclei at the droplet substrate interface leading to a rapid crystallization of the liquid Ga droplet into a GaAs crystallite that can be seen in Figure 3.5(a).

3.2.3 Impact of growth parameters on vertical yield

In addition to the mask processing conditions, the growth conditions play a crucial role for the formation of vertical NWs. Similar to growth on native oxide, for initiating NW growth, a Ga droplet needs to form. On the thin native silicon oxide, the surface diffusion length is on the order of several µm, determining the collection area of Ga. In combination with the density of pinholes in the oxide, it determines the number density of droplets and consequently NWs on the wafer.[63,64,90] In contrast, for SAG the diffusion of Ga atoms on the thicker thermal oxide is negligible due to high desorption and consequently Ga droplets are only formed by Ga atoms impinging directly in the hole opening.[44,91] Therefore, typically a Ga pre-deposition step is used to deposit enough Ga atoms to form a droplet of sufficient size before initiating NW growth. It was shown that at a Ga flux of 17 nm/min a deposition time of 45 s was optimal for patterns with holes having a similar size as on our substrates.[44] Thus, in our experiments we used a pre-deposition time of 90 s at a flux of 8.5 nm/min to achieve the same amount of Ga atoms for droplet formation.

After this pre-deposition step, the addition of an As flux initiates the GaAs crystal growth. The ratio of As and Ga flux is a particularly crucial factor for vertical NW growth. Figure 3.7 shows the vertical yield as a function of V/III ratio based on a series of samples grown with different As flux. The growth temperature was 630°C, the Ga flux 8.5 nm/min, the pre-deposition time 90 s and the As flux was varied from 15.3 nm/min to 34 nm/min. The vertical yield is highest at a V/III ratio of 2.4 yielding values above 70%. Figure 3.8(a) shows a larger part of a NW array grown under optimized growth conditions, underlining the high vertical yield. If the V/III ratio is too low, the droplet increases in size but no crystalline material is formed or the growth proceeds horizontaly on the substrate. On the other hand, if the V/III ratio is too high, the droplet rapidly crystallizes into GaAs and only crystallites are formed, terminating the VLS growth. This result is in qualitative agreement with previous reports,[40,42] which are based on different calibration procedures making it difficult to compare the exact V/III ratios. Due to the negligible collection of Ga atoms from the SAG mask, as discussed before, the effective V/III ratio at the droplet is larger than for growth on native oxide. Consequently, the V/III ratios used for SAG are lower than typical values used for growth on native oxide covered substrates for achieving comparable growth results.[90] The inset of Figure 3.7 shows a high-magnification micrograph of a NW array grown with the optimum growth conditions, underlining the high vertical yield and selective growth. Furthermore, the NWs exhibit a larger diameter compared to the sample grown on the native oxide covered substrate shown in Figure 3.1. This discrepancy is due to the different V/III ratios that were required for the growth on the different substrates. In the next chapter, we introduce a solution to this discrepancy.

3.3 Growth on large scale arrays patterned by nano-imprint lithography

For the realization of large NW arrays, it is desirable to transfer the growth from EBL patterned substrates to substrates patterned by a method with a higher throughput. Nano-imprint lithography (NIL) has been shown to be a potentially fast and effective technique to produce masks for SAG of NWs.[42,92,93] However, so far the NIL approach could not realize feature sizes that are comparable to what was achieved with EBL (40 nm).[39–41,43,94–96] However, for core-shell NW devices[17] it is desirable that the hole size is smaller than the final NW diameter of typically 50 nm in order to minimize leakage currents between the substrate and doped shells. Theoretically, the resolution limit of NIL depends mainly on the minimum feature size on the stamp, which can be fabricated by EBL. However, in practice, the precise pattern transfer into the mask layer with high fidelity depends first on the thickness and the uniformity of the residual layer underneath the imprint pattern, and second on the optimization of the plasma etching parameters for each process step.

Recently, a NIL process has been established at PDI, that enables the realization of

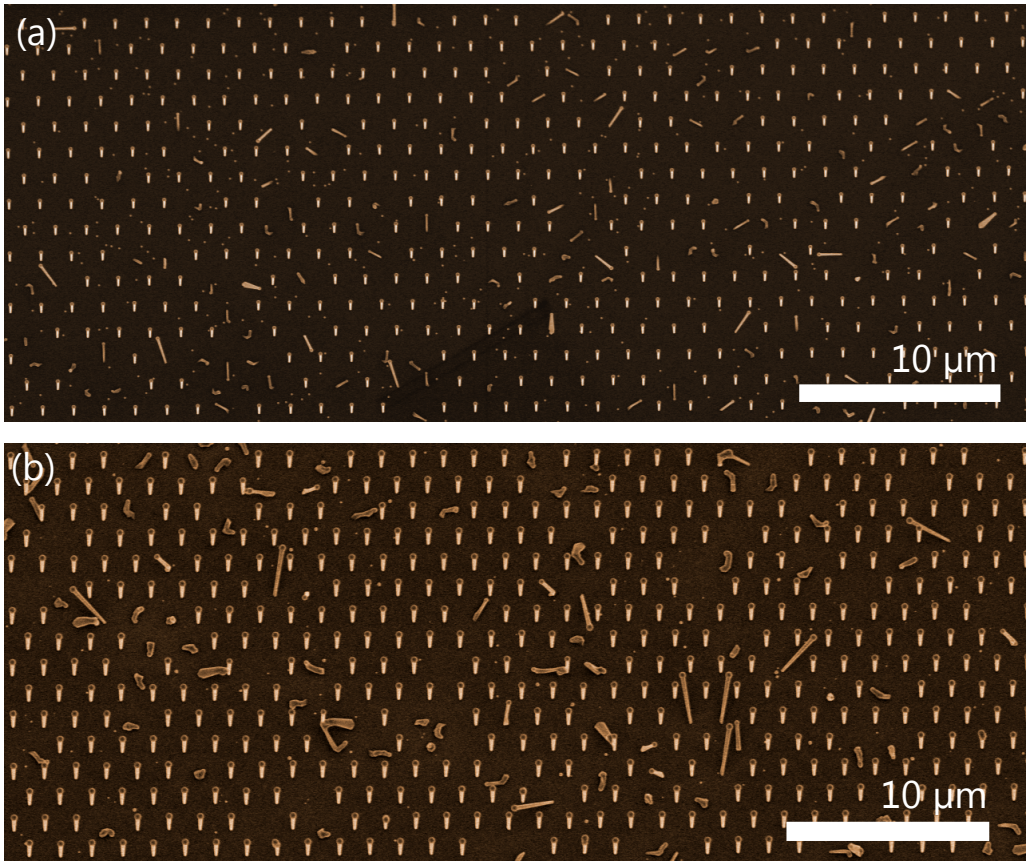

Figure 3.8: Micrographs of NW arrays on substrates patterned by different techniques: (a) Substrate patterned by EBL with optimized surface treatment and growth conditions. An overall vertical yield of 80% was achieved. (b) Substrate patterned by NIL with same surface treatment and growth conditions as in (a). The separation of the holes is 1.5 µm in both arrays. Both micrographs were taken under an angle of 15° from the substrate normal. The different morphology is due to different growth times of 20 min and 30 min, respectively.

hole sizes comparable to what has been achieved by EBL[45]. In this process an indirect pattern transfer is used to avoid underetching of the resist layer during the etching of the holes into the mask layer. Thereby, hole diameters below 50 nm could be realized in large arrays on the scale of the wafer (1.5 cm x 1.5 cm). Figure 3.8(b) shows a micrograph of a part of a NW array grown on a substrate patterned by NIL. Based on the optimization of surface preparation and growth parameters presented earlier in this chapter we could use the substrates patterned by NIL for the first time at PDI for the successful growth of NW ensembles with high vertical yield. However, for the course of this thesis we relied on the established EBL process for a high supply of substrates.

3.4 Conclusion

We introduced the growth of GaAs NWs by MBE with a focus on the Ga-assisted growth mode which is fundamental for this thesis. Based on the description of the current state of GaAs NW growth, we described our efforts to establish the growth of NWs on patterned Si substrates. Here, we improved the vertical yield of Ga-assisted GaAs NWs grown by MBE from 5% to 65% by following an improved substrate preparation procedure. The key process is rinsing in boiling water as the last step before loading the substrate into the MBE chamber. The origin for the improvement is not clear but we expect that it is related to the atomic scale roughness. These results will be important for understanding the initial formation of VLS NWs and will help facilitate the reproducible and comparable selective area growth of VLS NWs. On this basis we could investigate the impact of the most crucial growth parameter, namely the V/III flux ratio, on the vertical yield. Here, we found an optimum V/III ratio of 2.4 yielding a vertical yield of above 70%. This result is, in fact, smaller than the best report of close to 100%[44] but good in comparison to the majority of reports by other groups.[42,43,97,98] This result could then get transferred to substrates patterned by a novel NIL process. Therefore, this study presents the basis for the growth of NW samples on large-scale substrates and cost-effective patterns with a high vertical yield. The optimization of processing and growth parameters obtained in this chapter is the basis for establishing SAG as a reliable method to synthesize GaAs NW ensembles at PDI. Therefore, these results are the starting point for the detailed investigation of NW growth processes in the next chapter.

4 Diameter evolution of selective area grown GaAs nanowires

For many NW-based device structures it is crucial to control the diameter and shape of the NWs.[43,99] However, NWs grown by SAG typically exhibit a larger diameter and more tapering compared to NWs grown on unpatterned Si substrates covered with native oxide. In the Ga-assisted growth of GaAs NWs,[36,37] the droplet determines the NW diameter.[100] The droplet size depends on the effective V/III ratio at the droplet, which is affected crucially by surface diffusion of Ga. Therefore, the change of the size of the droplet during NW growth can easily lead to a diameter variation of the forming NW, resulting in either positively or negatively (inversely) tapered NWs.[37,101–103] Recently, theoretical models have been established to describe the shape of such NWs based on the droplet dynamics.[104,105] However, in addition to diameter variation due to the droplet dynamics, direct vapour-solid (VS) growth on the side facets is regularly observed, which also influences the NW diameter,[28,37,42,97,106–109] but this phenomenon lacks a comprehensive description.

In section 4.1, we develop a two-step growth procedure to decouple NW nucleation in the mask holes from NW elongation. NWs are nucleated at a low V/III ratio to maximizie the vertical yield based on the optimization of processing conditions and growth parameters discussed in chapter 3. After nucleation, the V/III flux ratio is adjusted to tailor the NW morphology. Using this approach, we realize high vertical yields of thin and untapered NWs with lengths of several µm.

In section 4.2, we analyze the elongation phase in detail using our versatile growth procedure. We find that radial VS growth has a strong impact on the final diameter and shape of the NW. We present a model that explains the observed radial growth and is consistent with the understanding of diffusion processes that are responsible for the axial growth. Finally, we combinine our VS growth model with an existing model for VLS growth by Tersoff.[104] Thereby, we can quantitatively describe the shape of complete NWs and its evolution during elongation. Finally, we use our comprehensive model to calculate the tapering over a large parameter space. This predictive map underlines the impact of the growth time on tapering and shows the full capability of the growth model.

In section 4.3, we discuss the impact of the radial growth and the involved diffusion processes on the doping of such NWs. Depending on the diffusion length of the dopant atoms we discuss different dopant density profiles in NWs and possible experiments to verify these. This understanding might be beneficial for the realization of doped NW

heterostructure with desired doping profiles. Furthermore, it can possibly give valuable insight into the fundamental adatom diffusion of dopant atoms, which is not accessible in 2D layer growth.

Parts of this chapter have been published in H. Küpers *et al.*, *Nano Research* (2018).[46]

4.1 Two-step growth for diameter variation while maintaining high vertical yield

Figure 4.1(a) shows a high-resolution micrograph of NWs grown under the optimum growth conditions discussed in chapter 3.2.3 (T_{growth} = 630 °C, f_{Ga} = 8.5 nm/min, $R_{5/3}$ = 2.2). The NW diameter is 160 nm at the top and tapering is pronounced at -2.5% (linearized tapering $\frac{d_{bot}-d_{top}}{l}$, where d_{bot} and d_{top} are the NW diameter at bottom and top, respectively, and l is the NW length[37]). We also note that higher resolution images show steps on the NW side facets. Diameters reported in literature for SAG are typically larger than the diameter for NWs grown on unpatterned substrates. For SAG the reported NW diameters are typically well above 60 nm for NW lengths of several µm,[41,42] whereas for growth on native oxide diameters down to 30 nm have been reported.[37,90] Furthermore, most reported SAG NWs were negatively tapered.[39,42,97,98] Both the large diameter and the tapering are a consequence of the lower V/III ratio, resulting in a large VLS droplet.[37,104]

The different requirements for vertical growth (low V/III ratio) and thin diameters (high V/III ratio) imply that both features cannot be achieved with a single set of growth conditions. To overcome this difficulty, we developed a growth approach with two sets of growth parameters for the different phases of growth: The first step provides growth conditions necessary to achieve a high vertical yield as discussed in section 3.2.3. These are a 90 s pre-deposition phase for Ga droplet formation, and subsequently GaAs growth with a low V/III ratio of 2.2. This step lasts 300 s, which is long enough to establish the stable VLS growth of NWs which reach a length of about 300 nm and have a diameter of 30 nm. In the second step the V/III ratio is increased by decreasing the Ga flux by closing one of the two Ga cells. This approach allows the V/III ratio to be increased without increasing the As flux, which would change the elongation rate (elongation varies linearly with As flux.[37] The total growth time for these two-step samples was 30 min.

Figure 4.1(b) shows a micrograph of a sample grown with a V/III ratio of 10.8 during the second step. This micrograph illustrates a thin and untapered morphology that has not been shown previously for selective area grown Ga-assisted GaAs NWs of this length. Furthermore, the sample exhibits a vertical yield of 55%, which is comparable to our optimized one-step yield, discussed in section 3.2.3. This result illustrates the efficacy of the two-step approach, which allows for the optimal V/III ratio both for nucleation and NW morphology.

Figure 4.1(c) presents in more detail the diameter at the top (green diamonds) and

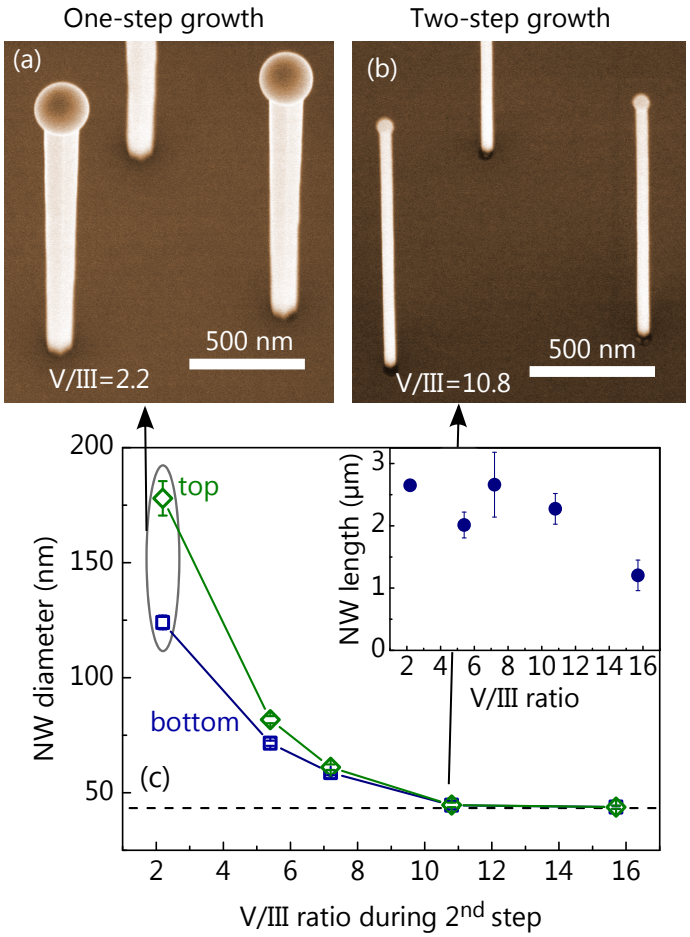

Figure 4.1: (a) SEM image of NWs grown with a constant V/III flux ratio of 2.2 for 30 min. The sample is tilted by 25° from the substrate normal. (b) SEM image of NWs grown with a two-step growth approach under a second-step V/III flux ratio of 10.8, exemplifying the efficacy of the growth approach. The sample is tilted by 25°. (c) NW diameter at top (green diamonds) and bottom (blue squares) for different V/III flux ratios during the second growth step. Inset: NW length for varying V/III ratio during the second step. The NW length is independent of the V/III ratio (Ga flux) except for the highest V/III ratio, where the NWs are significantly shorter due to the termination of the VLS growth. Adapted from Küpers *et al.* [46].

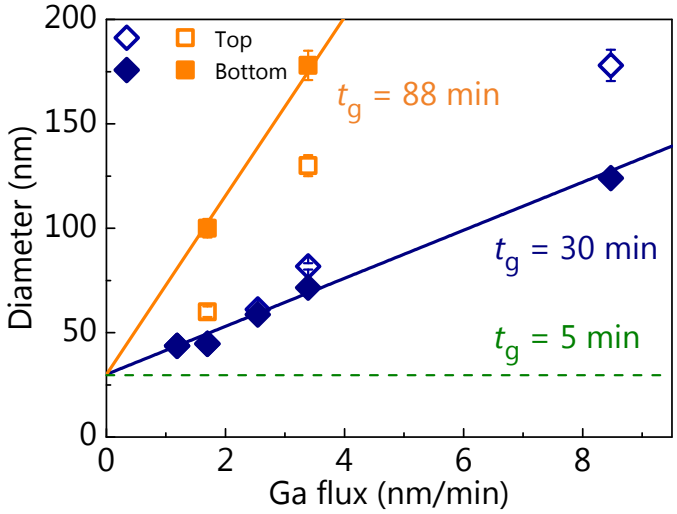

Figure 4.2: Diameter at the bottom (full symbols) and top (open symbols) of the NWs for varying Ga flux during the second growth step. The blue diamonds represent the same data as in Figure 4.1(c) (30 min growth time) and the orange squares represent samples grown for 88 min. The lines are guides to the eye for the bottom diameters of the two series. The green dashed line represents the bottom diameter at the beginning of the second step. Reprinted from Küpers *et al.* [46].

bottom (blue squares) of the NWs for varying V/III ratios during the second step. Both diameters decrease monotonically with increasing V/III ratio, becoming constant at a value of 45 nm for V/III ratios above 10.8. The inset of Figure 4.1(c) shows the NW length for varying V/III ratio in the second step. The length is roughly constant as expected for a constant growth time and As flux.[37,90,109] However, the NWs grown with highest V/III flux ratio of 15.7 are significantly shorter. These NWs exhibit a small Ga droplet with a low contact angle, indicating that the VLS growth is ceasing due to the high V/III ratio. For the highest V/III ratios the NWs have an untapered morphology. These thin and untapered NWs with high vertical yield will be the basis for all NW core-shell samples in the following chapters.

4.2 Model for radial growth

4.2.1 Descripton of growth model

In this study, all two-step samples start from a similar NW base which is grown within the first step. Thus, the diameter at the bottom of the NWs at the beginning of the second step is the same for all samples (30 nm) and it is unaffected by the droplet dynamics during the second step. Therefore, the variation of the bottom diameter in Figure 4.1(c) can only be caused by direct VS growth on the side-facets. In order to understand this phenomenon in more detail we plot the bottom diameters from Figure 4.1(c) as a function of Ga flux in Figure 4.2, making it more convenient to analyze VS growth. Additionally,

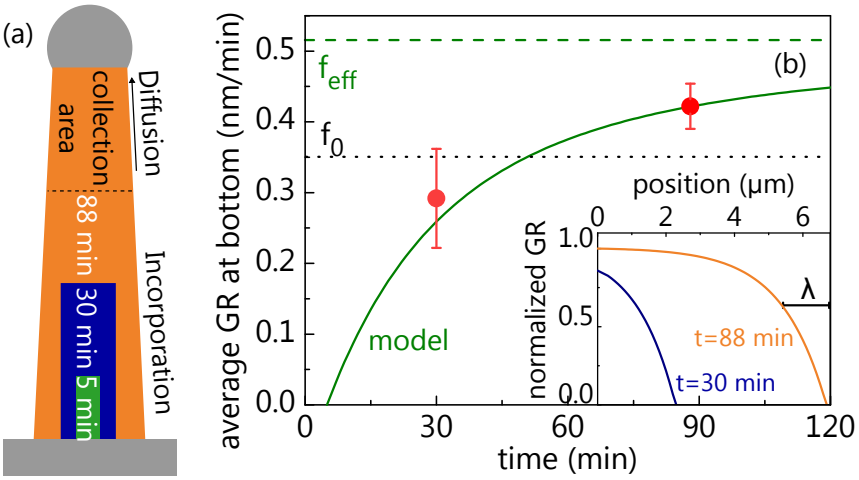

Figure 4.3: (a) Sketch of the NWs grown for different times, visualizing the VLS and VS growth processes: Within the collection area, most adatoms diffuse to the droplet, whereas below the collection area most adatoms are incorporated into the NW sidewall. (b) Average radial growth rate at the bottom of the NW calculated by Equation 4.1 for different times. The green line is a fit of Equation 4.5 to the data. The black dotted line represents the nominal flux f_0 from the effusion cell and the green dashed line the effective flux f_{eff} as determined by our model. Inset: Normalized differential radial growth rate as a function of position along the NW after 30 min of growth (blue line) and 88 min (orange line), as calculated by Equation 4.3. Reprinted from Küpers *et al.* [46].

we show data for samples with a longer growth time (88 min). For both series the bottom diameter increases linearly with increasing Ga flux (lines are guides to the eye), a clear indication of VS growth.

Figure 4.2 also shows the top diameter for the short and long NW series (open symbols), allowing the NW shape to be compared for the two growth times. Although NWs grown with Ga flux of 1.7 /nm/min show no tapering after 30 min, the top diameter after 88 min is much smaller than the bottom diameter. In other words, the tapering of the NW changes throughout growth and the untapered NW shape holds only for a certain growth time. The evolution of the NW shape with time is visualized in Figure 4.3(a).

To understand the above results, we first want to concentrate on the VS radial growth that happens at the bottom of the NWs. Focusing on the sample series grown with a V/III ratio of 10.8 ($f_{\text{Ga}} = 17$ nm/min), which leads to the smallest diameters, we calculate time-averaged radial growth rates GR_{av} as

$$GR_{\text{av}} = (r_{\text{g}} - r_1)/(t_{\text{g}} - t_1)\,, \tag{4.1}$$

with the NW radius at the bottom r_{g} after growth time t_{g}, and the NW radius at the bottom after the first step $r_1 = 30$ nm at $t_1 = 5$ min. These average growth rates are useful for considering only the growth during the second step. Figure 4.3(b) shows the calculated growth rates for the respective growth times based on the experimental diam-

eters in Figure 4.2. The average growth rate increases with growth time, and for 88 min it is larger than the growth rate corresponding to the directly impinging Ga flux from the effusion cell taking into account substrate rotation and angle between substrate normal and effusion cell. This finding indicates that a secondary flux exists, which we attribute to the re-evaporation of atoms from the oxide surface to the NW side-facets.[110] We exclude surface adatom diffusion on the substrate as it has been shown that this effect is not significant due to the low sticking coefficient of Ga on the thermal oxide.[44]

A central factor of VLS growth of NWs is a large diffusion length on the NW side-facets.[36,111] Ga atoms that impinge on the NW sidefacet diffuse along the NW axis to reach the Ga droplet where they eventually incorporate into the lattice at the liquid-solid interface. However, this supply by diffusion takes place mostly within a diffusion length from the droplet as indicated by the 'collection area' in Figure 4.3(a). For long NWs the bottom might be too far away for Ga atoms to reach the droplet. If we neglect desorption of Ga atoms on the NW sidewalls, which is a reasonable assumption at the growth temperature of 630 °C,[112] all Ga atoms that do not contribute to the diffusion supply must incorporate into the NW sidewall. For the quantitative description of the diffusion we solve the one-dimensional diffusion Equation.[113] The adatom density is given by

$$n(z,t) = \tau_{\mathrm{inc}} f_{\mathrm{eff}} \left(1 - \exp\left(-\frac{l(t)-z}{\lambda}\right)\right) , \tag{4.2}$$

with the surface lifetime before incorporation τ_{inc} (neglecting desorption), the total impinging Ga flux f_{eff}, the time-dependent NW length $l(t)$, the position on the NW axis z, and the diffusion length λ.[104] We calculate the radial growth rate at a specific point z as

$$GR(z,t) = \begin{cases} n(z,t)/\tau_{\mathrm{inc}} & \text{for } z \leq l(t) \\ 0 & \text{for } z > l(t) . \end{cases} \tag{4.3}$$

This equation, using a dimensionless $f_{\mathrm{eff}} = 1$ and $\lambda = 1.2$ µm (value that is obtained by the following analysis), is plotted in the inset of Figure 4.3(b) for two different times, corresponding to different NW lengths. The local radial VS growth rate strongly decreases near the droplet within a length comparable to the diffusion length, representing the collection area. Consequently, the radial VS growth rate at the bottom of the NW changes with time.

From Equation 4.3 we calculate the radially grown thickness at position z for the duration t_1 to t_{g} by integrating $GR(z,t)$ as

$$r_{\mathrm{VS}}(z,t_{\mathrm{g}}) = \int_{t_1}^{t_{\mathrm{g}}} GR(z,t)dt , \tag{4.4}$$

and therefore the average growth rate follows as

$$GR_{\mathrm{av}}(z,t_{\mathrm{g}}) = \frac{1}{t_{\mathrm{g}} - t_1} \int_{t_1}^{t_{\mathrm{g}}} GR(z,t)dt . \tag{4.5}$$

The model depends only on two free parameters, f_{eff} and λ. The time dependent length is calculated from the mean NW lengths in Figure 4.1(c), by assuming a constant growth rate, yielding $GR_{\text{ax}} = 76$ nm/min.

A fit of Equation 4.5 to the experimental data is shown by the green line in Figure 4.3(b). Here, we use $t_1 = 5$ min. An impinging flux f_{eff} of 0.52 nm/min (shown as green dashed line) is obtained, which amounts to 150% of the nominal impinging flux f_0 (black dotted line). This value is consistent with results reported for re-evaporation of As from the substrate and NW sidewalls[65] and re-evaporation of Ga in dense GaP NW arrays[110] and thus, confirms the hypothesis that Ga is re-evaporated from the substrate surface. Also the lack of growth on the oxide surface confirms that Ga desorbs from the oxide. A diffusion length of 1.2 μm is obtained from the fit, which is a reasonable value for this system and comparable to earlier results.[111]

Collection area - Diffusion length

In order to maintain a constant supply of Ga for the droplet and balance the high impinging As flux a large collection of Ga diffusing on the sidewall to the Ga droplet is necessary. Thereby the V/III ratio supplied by the cells can be larger than one without consuming the Ga droplet. Based on mass balance, the volume of grown Ga needs to be equal to the volume of Ga, directly impinging on the NW sidewall and on the droplet.

For the calculation of the collected amount of Ga we take into account diffusion of Ga adatoms on the sidewalls to the droplet and Ga atoms impinging directly on the droplet surface. Here, we neglect diffusion from the thermal oxide surface of the substrate as it is negligible at the growth temperature. On the other hand we include Ga re-evaporation from the substrate surface in the effective flux $f_{\text{eff}} = 0.52$ nm/min. Also we only consider the growth of a segment from growth time t_1 = 30 min to t_2=88 min to exclude varying factors during the intial phase of NW growth. We want to note that a more precise treatment of the impinging flux on the droplet surface was done previously[114] but here the collection by diffusion dominates the supply and it is sufficient to model the droplet supply in a basic way as atoms impinging on the droplet cross-section.

The collected volume depends on the impinging flux f_{eff}, the growth time t_{g}, the tilting angle of the source in the MBE α, the NW diameter d_{NW} (including the VS grown amount), the droplet diameter d_{drop}, and finally the diffusion length λ of Ga adatoms on the NW sidewall. We calculate

$$V_{\text{collection}} = f_{\text{eff}} t_{\text{g}} [\pi d_{\text{NW}} \lambda + \frac{\pi}{4} d_{\text{drop}}^2] = (8.05 \pm 0.59) \cdot 10^6 \text{nm}^3, \tag{4.6}$$

using the experimental values $\alpha = 33.5\ ^\circ$, $d_{\text{NW}} = 65 \pm 5$ nm, $t_{\text{g}} = t_2 - t_1 = 58$ min, $d_{\text{drop}} = 75 \pm 5$ nm. Here, we averaged the diameters for the growth duration of the segment. Furthermore we used the two fitting parameters from our radial growth model, $f_{\text{eff}} = 0.52$ nm/min and $\lambda = 1200$ nm.

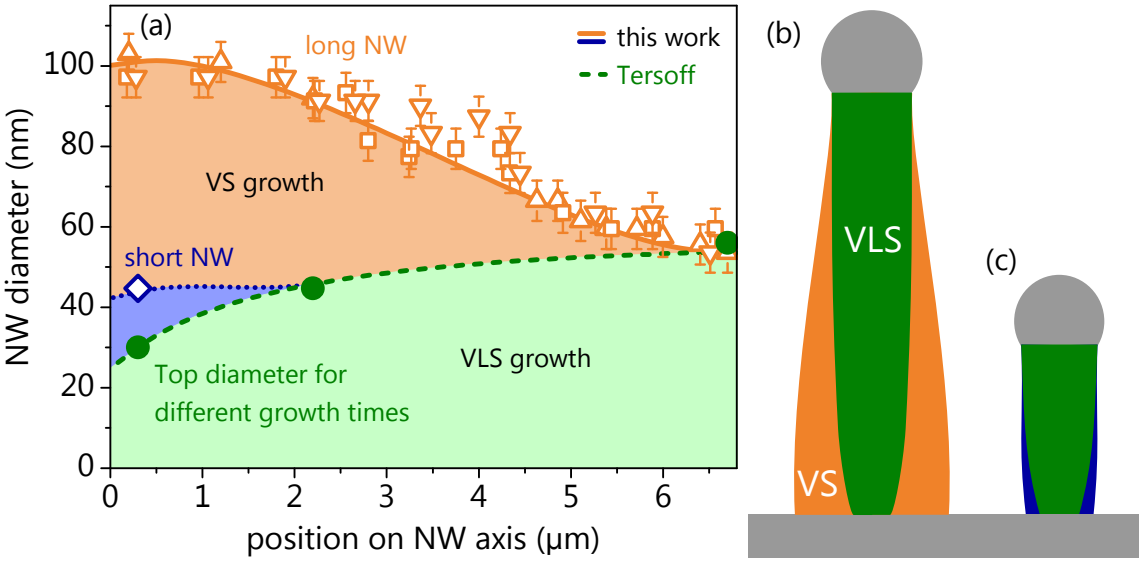

Figure 4.4: (a) NW diameter as a function of position along the NW axis for NWs grown for 5, 30 and 88 min. The full green circles show the top diameter for the three different times corresponding to different lengths. The dashed green line is a fit by Equation 4.8 describing droplet dynamics.[104] The open orange triangles and squares represent the diameter at different points of three long NWs. The diameter as calculated by Equation 4.9 is shown as the orange line. The dotted blue line shows the calculated values for the short NWs and is in agreement with the experimental value at the NW bottom shown as open blue diamond. The calculated shapes of the long and short NWs are shown schematically in (b) and (c), respectively. The green parts result from VLS growth, the orange and blue parts from VS growth. Reprinted from Küpers *et al.*[46].

The grown volume depends only on the grown length l_{NW}, corresponding to the axial growth rate, and the NW diameter d_{NW} at the top during growth, which was averaged from the experimental NW top diameters, and we can calculate

$$V_{\mathrm{grown}} = l_{\mathrm{NW}} \frac{\pi}{4} d_{\mathrm{NW,top}}^2 = (8.64 \pm 1.40) \cdot 10^6 \ \mathrm{nm}^3, \tag{4.7}$$

using the values $l = 4400 \pm 400$ nm, $d_{\mathrm{NW,top}} = 50 \pm 3$ nm. The two volumes calculated from fit values (Equation 4.6) and experimental data (Equation 4.7) agree within the error, meaning that the grown volume is equal to the collected volume of Ga atoms. This result shows that the fit factors we gained from our model for the radial VS growth are consistent with values necessary for axial growth.

4.2.2 Evaluating the nanowire shape

So far, we have established a model for the radial VS growth and have used it to explain the diameter widening observed at the bottom of the NWs. For a full description of the shape of a NW, both droplet dynamics (VLS) and radial growth (VS) need to be accounted for over the entire NW length. Tersoff has built a model for the self-assisted VLS NW

growth based on rate equations in order to explain the tapering due to the dynamics of the droplet.[104] According to that model, VLS growth can be stable for a large range of V/III ratios. The V/III ratio in combination with a natural length scale — the diffusion length λ — and a geometrical factor — the ratio of droplet height and NW radius $\eta = h/r$ — determine the dynamics of the NW diameter. However, in this model radial VS growth is neglected.

The model by Tersoff describing the radius of forming VLS NWs r_{VLS} over their length z is described by the equation:

$$\frac{dr_{\mathrm{VLS}}}{dz} = \frac{\frac{2\Omega_{\mathrm{L}}}{\Omega_{\mathrm{x}}}}{\eta(3+\eta^2)} \left[\frac{1}{R_{5/3,\,\mathrm{eff.}}} \left(1 + \frac{\lambda}{(1+\eta^2) r_{\mathrm{VLS}}} \right) - 1 \right] , \tag{4.8}$$

with Ω_{L} the atomic volume of liquid Ga, Ω_{x} the volume per two-atom unit of the crystal, and $R_{5/3,\,\mathrm{eff.}}$ the effective V/III flux ratio.

As a starting point for the full description of the NW shape, we consider the evolution of the top diameter with growth time. The top diameter is not affected by radial VS growth, and thus, these values are described well by Tersoff's model. The green circles in Figure 4.4(a) show the top diameter of the three samples grown for different times with the same growth conditions, plotted as a function of length. The dashed green line represents a fit of the solution of Equation 4.8 to the experimental data. The free fit parameters are a droplet shape factor η of 3.35 and an effective V/III ratio $R_{5/3,\,\mathrm{eff.}}$ of 5 ($\Omega_{\mathrm{L}}/\Omega_{\mathrm{x}} \approx 0.42$ for GaAs). The diffusion length was set to 1.2 µm as determined above.

The orange triangles and squares in Figure 4.4(a) represent the diameter along the axis of three 7 µm long NWs as measured by SEM after 88 min of growth. In striking contrast to the evolution of the top diameter, these long NWs exhibit a positively tapered shape, resulting from the radial VS growth. In order to describe the former dependence, we amended Tersoff's model to include direct radial VS growth. We simply add the contributions for VLS growth (solution of Equation 4.8) and VS growth (Equation 4.4) because radial growth due to droplet dynamics and VS growth are independent of each other:

$$r_{\mathrm{tot}}(z) = r_{\mathrm{VLS}} + r_{\mathrm{VS}} \, . \tag{4.9}$$

The result of this equation — using the fit parameters from the evaluation of the top diameters for the VLS contribution (fit to Equation 4.8) and from the fit of the VS model to the average radial VS growth rates at the bottom (fit to Equation 4.5) — is shown as the orange line in Figure 4.4(a). This model describes the diameter of the long NW along its entire length well. At the bottom a rather flat part is present in both the model and the experimental data. Here, the droplet dynamics lead to strong negative tapering, as seen in the green curve. This effect is compensated by the VS growth, yielding a flat bottom part. The upper part of the NW exhibits a positive tapering as it is dominated by VS growth. The amount of NW material resulting from axial VLS and radial VS growth is indicated by the green and orange areas, respectively. A visualization of the calculated

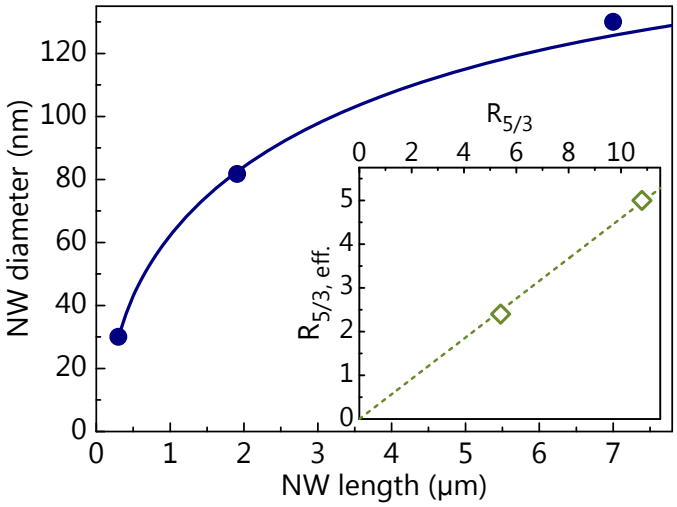

Figure 4.5: NW diameter as a function of NW length for the series of NW samples with $R_{5/3} = 5.4$. The circles are experimental values of the top diameter of samples grown for different times. The line represents theoretical values calculated by the solution to Equation 4.8 using $R_{5/3,\,\text{eff.}} = 2.4$. Inset: Effective V/III ratio $R_{5/3,\,\text{eff.}}$ as a function of experimental V/III ratio $R_{5/3}$. The dashed line is a fit of Equation 4.11 to the data.

NW shape with the parts due to VLS and VS growth is shown in Figure 4.4(b). We emphasize the strong agreement between the experimental data and our model. The model curves are not fits to the data, but are calculations using the fit parameters gained from the analysis of the VS growth at the NW bottom by Equation 4.5. The excellent agreement between experimental data and model seen in Figure 4.4(a) demonstrates the validity of our model.

We use our comprehensive model to describe the shape of the short NWs, which is shown as the blue line in Figure 4.4(a). In agreement with our experimental results, the shape is essentially untapered. Our model reveals that the untapered morphology as shown in Figure 4.4(c) is a consequence of the droplet dynamics and the VS growth compensating each other. Thus, by balancing droplet dynamics and VS growth, straight NWs can be achieved.

4.2.3 Predictive modelling of the nanowire shape

So far, we have shown that our model successfully describes the experimental data. Based on these results, we want to use it to explore a larger range of the parameter space and predict the outcome of future growth experiments. In principle, the model only depends on the V/III ratio, which governs the axial and radial growth. However, to vary the V/III ratio in the complete model represented by Equation 4.9, we need to correlate the effective V/III ratio from Tersoff's model $R_{5/3,\,\text{eff.}}$ in Equation 4.8 with the experimental value for the V/III ratio $R_{5/3}$. In the previous analysis, we obtained $R_{5/3,\,\text{eff.}} = 5$ by

fitting the model to the experimental data corresponding to $R_{5/3} = 10.8$ (cf. Figure 4.4). For the time series grown with $R_{5/3} = 5.4$ (Ga flux of 3.4 nm/min in Figure 4.2), we use the same procedure to obtain a value for $R_{5/3,\,\mathrm{eff.}}$. The circles in Figure 4.5 show the NW top diameter as function of length. The blue line shows a fit of Equation 4.8 to the experimental data, using λ=1200 nm and η=3.35 as before, yielding $R_{5/3,\,\mathrm{eff.}} = 2.4$.

The inset in Figure 4.5 shows the effective V/III ratio $R_{5/3,\,\mathrm{eff.}}$ as a function of experimental V/III ratio $R_{5/3}$. The effective V/III ratio is calculated as

$$R_{5/3,\,\mathrm{eff.}} = \frac{k_5 F_5^n}{k_3 F_3^n - \Phi_{\mathrm{evap}}}\,, \tag{4.10}$$

with sticking factor k_5 and k_3 for As and Ga, respectively, the nominal As and Ga fluxes F_5^n and F_3^n, respectively, and a flux of Ga atoms desorbing from the droplet Φ_{evap}.[104] The desorption rate for bulk Ga at 630 °C is low and we expect an increase due to the Kelvin effect only for smaller droplets.[115] Therefore, we assume that Φ_{evap} is negligible and we obtain

$$R_{5/3,\,\mathrm{eff.}} = \frac{k_5 F_5^n}{k_3 F_3^n} = \frac{k_5}{k_3} R_{5/3}\,. \tag{4.11}$$

The dashed line in the inset of Figure 4.5 shows a fit of Equation 4.11 to the two data points, yielding $k_5/k_3 = 0.459 \pm 0.007$. This value suggests that sticking of Ga atoms is twice as high as for As. Possibly, only one As atom per As_2 dimer is absorbed into the droplet or the value just relates to the re-evaporation rate of dissolved As from the droplet. However, this result is only based on two data points.

In our two-step growth scheme, $R_{5/3}$ is varied by adjusting the Ga flux. As the VS growth rate in Equation 4.2 is proportional to the Ga flux, it must also change according to the V/III ratio in the complete model, yielding

$$f_{\mathrm{eff}} = \frac{10.8}{R_{5/3}} \cdot 0.52\ \mathrm{nm/min} = \frac{2.58}{R_{5/3,\,\mathrm{eff.}}} \mathrm{nm/min}. \tag{4.12}$$

This dependence is only valid for the exact As flux that was used in our study. With equations 4.9, 4.11 and 4.12 we can calculate the NW shape $d(z, t, R_{5/3})$ that depends only on time and V/III ratio, besides constant parameters such as diffusion length and droplet shape factor. For a meaningful visualization we reduce the complete NW shape to the linearized tapering value Γ:

$$\Gamma(R_{5/3}, t_{\mathrm{growth}}) = \frac{r(z_{\mathrm{bottom}}, R_{5/3}, t_{\mathrm{growth}}) - r(z_{\mathrm{top}}, R_{5/3}, t_{\mathrm{growth}})}{l} \tag{4.13}$$

Figure 4.6 shows Γ calculated by Equation 4.13 as a function of V/III ratio and growth time. Negative tapering is marked in red, positive tapering in blue. The corresponding shapes are visualized by schematic NWs in the respective areas. The tapering due to droplet dynamics is strongest for small V/III ratios, leading to negative tapering, in par-

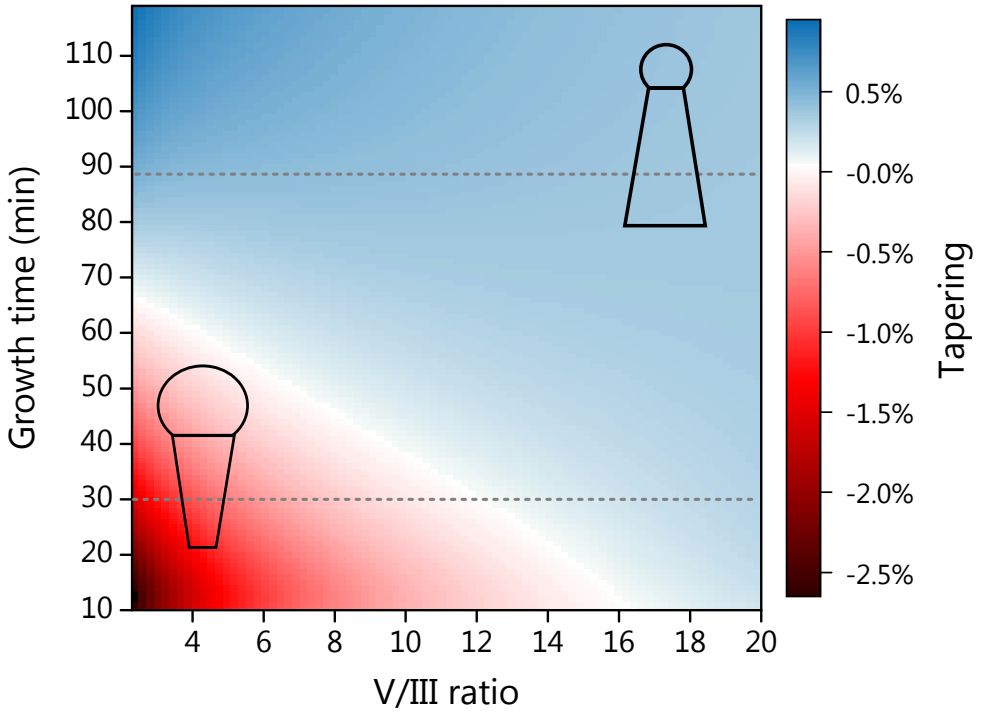

Figure 4.6: Tapering as function of V/III ratio and growth time for a diffusion length of 1.2 µm. The white area displays an untapered morphology. The two sketches exemplify the NW shapes in regions of negative (red) and positive (blue) tapering. The two lines correspond to the data series shown in Figure 4.7(a).

ticular for short growth times when VS growth is negligible due to the small NW length. However, after the droplet has reached a constant size and the NW has gained in length, the VS growth always dominates, leading to positive tapering. This result is in agreement with the common understanding of tapering due to droplet dynamics[37,116] and extends it by integrating VS growth. Interestingly, in the map we observe strong positive tapering for low V/III ratios and long growth times. Here, the radial VS growth is comparably large, particularly at the bottom. For long growth times, the droplet approaches a constant size, which in combination leads to the strong positive tapering. This result is in contrast to what has been predicted when the VS growth is neglected.

To validate our results we compare the calculated values with the experimental values from two series. Figure 4.7(a) shows the experimental data for tapering as a function of V/III ratio for growth times of 30 (blue circles) and 88 min (orange circles). The values are calculated from the diameters reported in Figure 4.2. The dashed lines represent values calculated using our model (indicated by dotted lines in Figure 4.6). For 88 min growth time, the calculated values are in good agreement with the experimental values. For 30 min growth time the calculated values deviate from the experimental values, in particular for low V/III ratios. Here, the calculated values are lower than the experimental values. By comparing the experimental shape of these NWs with the calculated shape (not shown here), we see that the experimental bottom diameter is larger than the

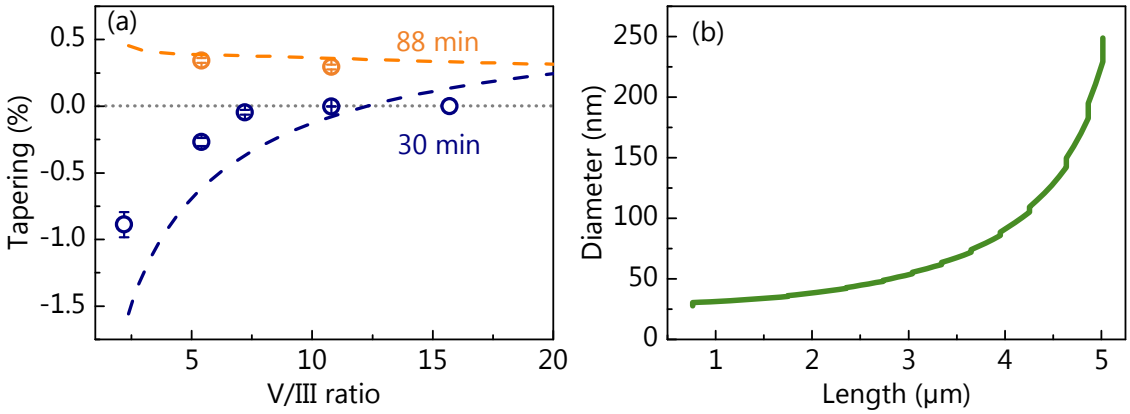

Figure 4.7: (a) Tapering as a function of V/III ratio for growth times of 30 min (blue) and 88 min (orange). The circles are values calculated from experimental data in Figure 4.2 and the dashed lines are calculated data taken from the map in Figure 4.6 as indicated by the dashed lines. (b) Unique combinations of diameter and length for untapered NW morphologies corresponding to the white region in Figure 4.6.

calculated value, leading to the discrepancy in tapering. Also the calculated value for the sample with V/III ratio of 15.8 is larger than the experimental value.

At the bottom of the NW, the tapering of the VLS grown part of the NW is very large, in particular for low V/III ratio, as the droplet increases rapidly in size during the initial stage of growth (cf. bottom part in Figure 4.5). This large tapering implies that many atomic steps exist on the NW sidefacets following the curvature. For a tapering value of 2% the average terrace width for a monolayer step would be 39 nm on the $(1\bar{1}0)$ facet. These steps might act as preferential incorporation sites for Ga atoms into the lattice, resulting in a larger diameter at the bottom of the NW. Such tapering-dependent effects are not taken into account by our model. On the other hand, for very high V/III ratios the VLS growth is beginning to cease, leading to a smaller droplet size and NW diameter than expected from the model, explaining the observed deviation. This behaviour is not taken into account by Tersoff's model. However, even though deviations between model and experiment exist, the general behaviour is described well.

The white area in Figure 4.6 indicates the parameter sets resulting in untapered NWs. This stripe separates the negatively and positively tapered regions. Figure 4.7(b) shows the corresponding calculated diameter and length of these untapered NWs. Here, short growth times correspond to short NWs. The Figure shows that for every length only a unique diameter exist for which an untapered NW can be realized. This result is a consequence from our model which shows that tapering is length-dependent. Even if an equilibrium droplet size has been achieved quickly, the time-dependence of the VS growth might change the bottom diameter non-linearly over time. This result is in contrast to the self-equilibration theories proposed previously[104,111,117] and it poses a major difficulty for the realization of NW ensembles of arbitrary length and diameter. The dominant parameter in our model is the surface diffusion length of Ga. Therefore, by changing the

growth temperature during the second step one might obtain different values, shifting the curve in Figure 4.7(b) horizontally. However, by changing the growth temperature, also other properties of the complex growth system might change, such as the evaporation of As from the droplet.

4.3 Role of surface diffusion for the doping of nanowires

For the realization of functional electronic devices it is necessary to dope the semiconductor material with foreign atoms, to obtain p and n-type material with controlled charge carrier densities. Therefore, understanding the doping mechanisms is of highest interest in growth studies. For planar layers, it is typically assumed that dopant atoms do not desorb from the surface and are incorporated entirely into the lattice. In the case of NWs, the distinction of the incorporation path of dopant atoms is not trivial. The dopant atoms impinge on the droplet as well as on the NW sidewalls, hence they could be incorporated via the droplet or directly into the sidewall. Therefore, many studies focused on the incorporation path and the consequences for the dopant densities and electrical properties in NWs.[118–125] This path is particularly important when using Si as dopant which can incorporate on both lattice sites leading to either p or n-type material. This amphoteric behaviour depends on the growth conditions and NW shells are typically n-type,[122] whereas for VLS grown cores strong self-compensation has been observed.[120,126]

In the previous sections, we have shown that a substantial part of the NW volume is grown by direct radial VS growth. Dopant atoms impinging on the NW sidewall might incorporate into this VS grown shell as it was suggested previously.[120] We have shown that the VS growth on the sidewall depends on the adatom diffusion length of Ga λ_{Ga}. Similarly, the incorporation of dopant atoms must depend on their respective adatom diffusion length $\lambda_{\mathrm{dopant}}$. To our knowledge, adatom diffusion of dopants was not investigated for planar layers as it is difficult to assess. However, for NWs we can discuss three extreme cases by only taking into account the diffusion length of Ga and the dopant species, respectively:

(i) $\lambda_{\mathrm{dopant}} \gg \lambda_{\mathrm{Ga}}$: The dopant atoms diffuse more readily to the droplet than the Ga atoms and only get incorporated through the droplet. The dopant density in the VLS grown part will be higher than the nominal value, obtained from planar reference layers, as the ratio of dopant atoms to Ga atoms is larger than in the nominal case. Consequently, the VS grown shell will be virtually undoped.

(ii) $\lambda_{\mathrm{dopant}} \approx \lambda_{\mathrm{Ga}}$: The dopant atoms and Ga atoms diffuse to the droplet in a similar way. The dopant density will have the nominal value in the VLS and VS grown part as dopant atoms and Ga atoms are distributed homogeneously over the entire NW structure.

(iii) $\lambda_{\mathrm{dopant}} \ll \lambda_{\mathrm{Ga}}$: The dopant atoms do not diffuse along the NW sidewall and incorporate where they impinge. In this case, the VLS grown part is only doped by dopant atoms impinging directly on the droplet surface. There, the dopant density would be proportional to the Ga/As ratio as the As flux determines the axial growth rate but the nominal dopant density is typically calibrated to the Ga flux. The dopant density in the VS grown part is determined by the radial GaAs growth rate which changes over time as we have shown in the previous sections. Consequently, the dopant density would show a gradient in the VS grown part.

In the first two cases, it is trivial to calculate the expected dopant densities that could be verified by experiment. In the third case the density profile is more complex in the VS grown shell and we calculate it using our growth model. For simplicity, we exclude diffusion of dopant atoms completely ($\lambda_{\mathrm{dopant}} = 0$ µm). The dopant density in the VS grown part is determined by the GaAs growth rate on the sidewall. From Equation 4.3 and 4.4 we calculate the VS growth rate and the thickness of the grown shell as a function of time:

$$\begin{aligned} GR_{\mathrm{VS}}(z,t) &= f_{\mathrm{eff}}\left[1-\exp\left(\frac{z-GR_{\mathrm{ax}}t}{\lambda_{\mathrm{Ga}}}\right)\right] \\ d(z,t) &= f_{\mathrm{eff}}\left[t+\frac{\lambda_{\mathrm{Ga}}}{GR_{\mathrm{ax}}}\exp\left(\frac{z-GR_{\mathrm{ax}}t}{\lambda_{\mathrm{Ga}}}\right)-\frac{\lambda_{\mathrm{Ga}}}{GR_{\mathrm{ax}}}\exp\left(\frac{z}{\lambda_{\mathrm{Ga}}}\right)\right]. \end{aligned} \tag{4.14}$$

Assuming that the dopant atoms neither diffuse on the surface nor inside the lattice we calculate the dopant density ρ from GR_{VS} as

$$\rho(z,t) = \rho_{\mathrm{nom}}\frac{f_{\mathrm{eff}}}{GR_{\mathrm{VS}}(z,t)}\,, \tag{4.15}$$

where ρ_{nom} is the nominal dopant density from planar growth calibration. Here, for simplicity, we assume that the re-desorption of Ga and dopant atoms from the mask surface is equivalent. Figure 4.8 shows the dopant density distribution as a function of radius and position along the NW axis for $\rho_{\mathrm{nom}} = 10^{19}$ cm^{-3}, $t_{\mathrm{g}} = 40$ min, and $R_{5/3} = 5$. Similar to the representation in Figure 4.4(a) the viewgraph shows the radial distribution of dopant atoms along its axis for a 3 µm long NW. The grey area represents the VLS-grown core with a constant dopant distribution scaled by the Ga/As ratio as discussed before, yielding a dopant density of $\rho_{\mathrm{VLS}} = \rho_{\mathrm{nom}}/R_{5/3} = 2\cdot 10^{18}\mathrm{cm}^{-3}$. The colored area represents the dopant density in the VS grown shell. The green area at the outer part of the VS shell shows a dopant density similar to the nominal value. Here, the radial GaAs growth rate has reached its maximum value. In contrast, at the interface to the VLS core, the dopant density increases to values more than an order of magnitude higher than the nominal density.

The Inset of Figure 4.8 shows the calculated dopant density as a function of VS grown thickness at a fixed position along the NW axis, for $\rho_{\mathrm{nom}} = 10^{19}$ cm^{-3} and varying Ga

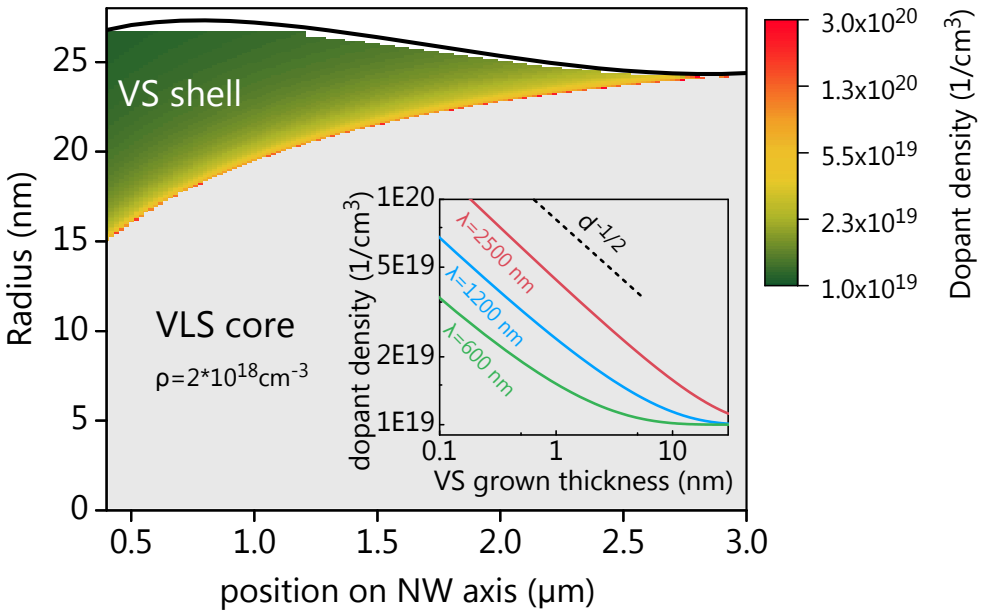

Figure 4.8: Map of calculated dopant density in the VLS and VS grown part of the NW. The grey area shows the VLS core with $\rho = 2 \cdot 10^{18}\text{cm}^{-3}$. The black line shows the calculated total NW radius, where the deviation from the colored area is due to the rasterization of the 2D data by the graphics software. Inset: Double logarithmic plot of dopant density calculated by Equation 4.15 as a function of VS grown thickness for different diffusion lengths indicated in the diagram. The dashed line indicates a $\rho \propto 1/\sqrt{d}$ dependence. The nominal dopant density is 10^{19}cm^{-3} for all calculations.

diffusion length. Here, the left side of the plot shows the interface to the VLS grown part. The double-logarithmic plot emphasizes the rapid decrease in dopant density within the first grown nanometers, corresponding to few monolayers as for the $(1\bar{1}0)$ sidefacets a monolayer of GaAs has a thickness of $a_{100}/(2\sqrt{2}) = 1.998$Å. Within this part, the dopant density decreases as $\rho \propto 1/\sqrt{d}$, as indicated by the dashed line. For the outer part of the shell (larger grown thickness) the dopant density reaches the nominal value, as the VS growth rate has reached its maximum value. For a larger Ga diffusion length, the dopant density is higher and the enriched area extends to larger thicknesses. In the case of $\lambda_{\text{Ga}} = 2500$ nm for example, even for a VS grown thickness of 10 nm the dopant density shows about twice the nominal value. This highly doped but thin region might act similar to what is known as delta-doping, where the dopant atoms are nominally confined within one ML.[127] Therefore, the high dopant density at the interface might lead to band bending due to the different dopant density in the core and Fermi-level pinning at the surface.

Based on this understanding of the theoretical dopant density profiles, we could potentially derive information about the adatom diffusion of dopant atoms from experimental data of the dopant distribution in a NW. A promising experimental technique is atom probe tomography (APT).[119] Here, the elemental 3D distribution in a NW segment can

be measured with high sensitivity. Samples grown under supply of different dopant species might show variations if the respective adatom diffusion length of the species is different. Our MBE system would offer Si and Be but more species are widely used, such as Sn, Te, C, and Zn. So far, APT has been used to study dopant profiles of Si NWs but also of GaAs NWs with varying results. It was shown that surface doping layers exist[118,123,128], but also homogeneous radial profiles have been observed[125]. The different observations are possibly related to differences in growth conditions, resulting in varying diffusion length and VS growth rate. Also the growth method and investigated material may have crucial impact. Therefore, for the investigation of different dopant species an experiment is necessary with samples grown under comparable conditions.

However, recently it was suggested that enhanced incorporation of dopant atoms at truncated facets at the droplet NW interface might lead to inhomogeneous dopant profiles[123,129]. Furthermore, during growth, diffusion of the dopant atoms into areas with lower dopant concentration might take place,[130,131] effectively reducing the peak of the density distribution. These effects might lead to difficulties for the interpretation of the data.

4.4 Conclusion

Our novel two-step growth approach enables simultaneous optimization of vertical yield and NW morphology. We show that increasing the V/III ratio during the second step leads to a clear reduction of the NW diameter, and the realization of untapered NWs with diameters of 45 nm at a length of 2.5 µm. This achievement serves as the ideal basis for the growth of strained shells on such thin cores and thus will be the basis for the growth experiments in the next chapters.

Despite the high growth temperature of 630 °C, radial VS growth is significant and leads to an increase in diameter during growth. On the basis of these findings we developed a comprehensive growth model that takes into account both factors influencing the NW diameter: droplet dynamics and radial VS growth. This model successfully describes the evolution of the NW morphology throughout the growth. An untapered NW shape requires a balance between droplet dynamics and radial VS growth, which can be achieved for given growth conditions only for a certain growth time and hence length. Very importantly, even in untapered NWs a large part of the NW volume can result from radial VS growth. This understanding of the factors that determine the NW shape now enabled its prediction over a large parameter range which will help in the precise engineering of different NW shapes, that are necessary for the realization of complex device structures.

This study used SAG in order to have a better control over NW growth. Our study is the first experimental confirmation of the shape of self-assisted GaAs NWs described by a theoretical model that describes the atomic processes on the NW sidefacet. At the

same time our comprehensive model is based on a consideration of the incorporation pathways and is therefore not restricted to SAG of NWs. As droplet dynamics and radial VS growth are fundamental processes for VLS NW growth, the basic ideas of our model can also be applied to other material systems. Furthermore, as the mechanisms discussed here are not limited to MBE, we think our insights should also apply to other growth methods like metal-organic vapour-phase epitaxy (MOVPE), where additional processes like the dissociation of pre-cursor molecules also play a role and need to be accounted for.[106,107,132]

Finally, we showed that depending on the respective adatom diffusion lengths of Ga atoms and dopant atoms, different dopant profiles may result in a GaAs NW. For the case of negligible surface diffusion of dopant atoms we showed that the length-dependent VS growth rate should have an impact on the dopant distribution in the VS grown shell. Here, a layer with an enhanced dopant density forms at the interface between VLS and VS grown parts. The layer of increased dopant density is only few nanometers wide but amounts to values that are more than an order of magnitude higher than the nominal dopant density. If compared to future experimental data of the dopant distribution in a NW, these results may give valuable insight into the adatom diffusion of dopant atoms, a fundamental property that has not been studied for planar layers as it is difficult to assess.

5 Growth and properties of (In,Ga)As shells on GaAs nanowires by molecular beam epitaxy

A key feature of nanostructures is their high surface to volume ratio. For NWs in particular, this feature can be exploited by fabricating devices in a core-shell structure to obtain a large effective area.[133,134] Furthermore, in such structures the strain is divided between the core and shell, thus enabling the combination of materials with high lattice mismatch.[135–138] In recent years, various core-shell structures have been realized, such as Si/Si:B,[133] InAs/GaSb,[139] C/Si[140] and GaAs/(Al,Ga)As,[15,141,142] all targeting different applications. An (In,Ga)As shell in a GaAs/(In,Ga)As/GaAs core-multishell structure is a model candidate for an optically active shell quantum well (QW) for light emission in the near-infrared. The strain in an (In,Ga)As QW increases with the In content as shown in Figure 5.1, thus, strain relaxation by formation of plastic dislocations takes place at high In contents for planar layers. The strain partitioning between core and shell is expected to enable the realization of coherent (In,Ga)As shells with higher In contents compared to planar layers. Thus, the emission energies can be extended into the telecommunication range as shown in Figure 5.1. Therefore, (In,Ga)As shells have attracted interest in recent years and have been synthesized by MBE[17,18,143] and MOVPE[16,19] and on InP NWs by MOVPE.[144,145] Recently, it was shown that (In,Ga)As shells can be grown pseudomorphically with In contents of up to 50%.[20]

For the growth of such three-dimensional structures with directional deposition techniques such as MBE, the directionality of the material fluxes needs to be taken into account. To avoid shadowing of the molecular beams by neighbouring NWs, we use NW cores grown in arrays with controlled separation as described in chapters 3 and 4. Due to the flux directionality, different materials are impinging on the NW sidewalls at different times, resulting in an inherent flux sequence. As we will show, this sequence governs the growth dynamics. This effect has been mostly neglected until now.[148]

In section 5.1, we introduce the growth of semiconductor shells by MBE in general and present our growth procedure. We discuss the microstructure of NW core-shell heterostructures and show that our samples show very symmetric cross-sectional shapes.

In section 5.2, we explore the impact of growth conditions on the luminescence properties of the (In,Ga)As shell. Optimum values for achieving high PL intensities comprise a relatively low growth temperature, a high V/III ratio and a combined Ga and In flux

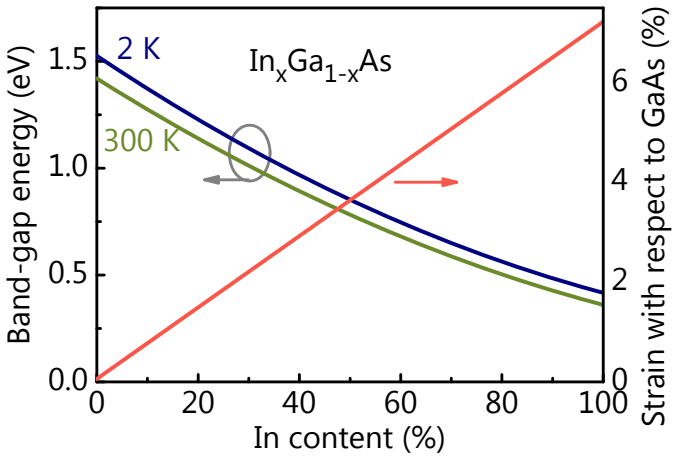

Figure 5.1: Band-gap energy at 2 K[146] (blue line) and 300 K[147] (green line) of relaxed (In,Ga)As and strain with respect to a rigid GaAs substrate as a function of In content for (In,Ga)As (red line). The strain is calculated as $\epsilon = (a_{(In,Ga)As} - a_{GaAs})/a_{GaAs}$ with lattice parameters $a_{(In,Ga)As}$ and a_{GaAs} for (In,Ga)As and GaAs, respectively.[146]

that results in the growth of a monolayer per revolution. CL linescans indicate that for increasing growth temperatures the luminescence is distributed inhomogeneously along the NW length.

In section 5.3, we show that the relative direction of the As and the group III fluxes has crucial impact on the material quality of (In,Ga)As shells. We grow shells using two different As cells, which results in different sequences of fluxes impinging on the same sidewall at the same time. The luminescence intensity of these samples differs by more than two orders of magnitude. No extended defects are indicated by transmission electron micrographs, suggesting that point defects are responsible for the low luminescence intensity. We show that for the case leading to high luminescence intensity, the flux sequence resembles migration enhanced epitaxy (MEE), which has been used widely to achieve layers with highest material qualities even at low growth temperatures. As a consequence of this effect, the growth rate and rotation speed have distinct impacts on the growth dynamics.

5.1 NW core-shell structures

5.1.1 Growth of NW core-shell structures

The axial growth of NWs relies on a high diffusion length of atoms on the NW sidewalls.[36,111] In chapter 4, we have shown that substantial VS growth happens also on the sidewall, resulting in non-uniform shells. Therefore, two main conditions need to be fullfilled for the conformal growth of NW shells. First, the preferential axial growth needs to be stopped by crystallizing the liquid droplet.[122] Otherwise, we have seen that even

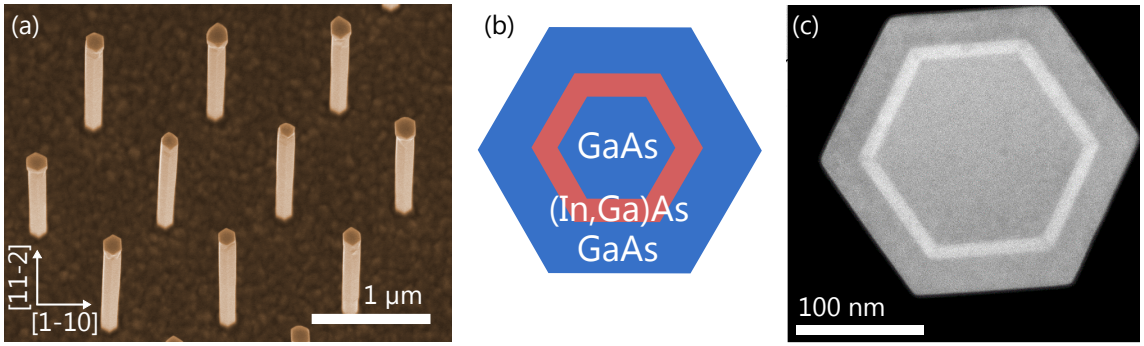

Figure 5.2: (a) SEM image of an ensemble of core-shell NW heterostructures. The image is taken under an angle of 15° from the substrate normal. (b) Cross-sectional structure of the core-shell NW heterostructure discussed in this chapter: A 50 nm thick core, a 10 nm thick (In,Ga)As shell, and a 30 nm GaAs cap. (c) Dark-field transmission electron micrograph in cross-section of a sample with a 130 nm thick core and the same shell structure as in (b). TEM measurement performed by Achim Trampert.

for shell growth of materials with low diffusion length, axial segments may form. This is in contrast to earlier reports of (Al,Ga)As shells grown at high temperature without consuming the Ga droplet.[56] Second, the adatom diffusion length on the sidewalls needs to be decreased to grow conformal shells around the NW core which can be achieved by decreasing the substrate temperature and increasing the As flux.[149]

Figure 5.2(a) shows a micrograph of a NW core-shell sample, typical of the samples investigated in this chapter. All samples were grown on pre-patterned substrates as described in chapters 3 and 4. Here, we focus our analysis on NW ensembles grown in arrays with a separation of 1 µm to avoid shadowing effects by neighbouring NWs while having a high enough density of NWs to facilitate PL investigations of NW ensembles. The GaAs NW core has a length of around 2.5 µm and a diameter of 50 nm. After growth of the core, the liquid Ga droplet is crystallized under exposure to a high As flux at 630 °C for 10 min. The As flux is selected such that it is later used for the growth of the shells (typically $f_{As} = 200$ nm/min). This crystallization procedure leads to the formation of flat top facets[122,150]. We note that crystallization at temperatures around 400 °C resulted in the formation of long spike-shaped structures at the top of the NW instead of flat top facets. Therefore, only after the droplet is crystallized, the temperature is decreased to the shell growth temperature under continuous As exposure. The (In,Ga)As and GaAs shells are grown at a constant substrate temperature which is measured by the pyrometer just before initiating shell growth. To finish shell growth, all material sources are closed and the substrate temperature is decreased to 100 °C at a rate of 1 °C/s.

5.1.2 Microstructure of core-shell structures

Figure 5.2(b) shows a schematic diagram of the cross-section of a core-shell NW heterostructure. The hexagonal GaAs core and the GaAs outer shell are drawn in blue, the

(In,Ga)As shell is drawn in red. All samples discussed in this thesis have a nominally 10 nm thick (In,Ga)As shell with an In content of 15%. Figure 5.2(c) shows a cross-sectional transmission electron micrograph of a sample which contains the same shell structure that we discussed before, but the core has a diameter of 130 nm. The image is acquired under dark-field conditions, which means that electrons that are diffracted by the specimen are detected out of the optical axis. This method is sensitive to the atomic mass of the species as the atomic number determines the scattering cross-section. As In (Z=49) has a higher atomic number than Ga (Z=31), the bright area in the micrograph corresponds to the (In,Ga)As shell. The micrograph demonstrates the hexagonal shape of the NW core which is adopted by the shells with its $\{1\bar{1}0\}$ sidefacets. The shape appears to be symmetric on all facets. This result is in contrast to previous investigations of NWs grown on unpatterned substrates, showing asymmetric structures and inhomogeneous shell thickness due to shadowing effects of neighbouring NWs[151]. This result shows the efficacy of using SAG for avoiding such shadowing effects.

The $In_{0.15}Ga_{0.85}As$ shell exhibits lower contrast stripes at the six edges, indicating a lower In content. For NWs in general, the small diameter and three-dimensional structure emphasize the importance of the edges connecting the $(1\bar{1}0)$ sidefacets. Similar to what has been observed in overgrown mesa-structures,[152,153] the incorporation of atoms at such edges can differ significantly from the planar layer. Here, the exchange of atoms by diffusion from one facet to the edge or vice versa leads to enrichment of the species with lower diffusion length on the forming edge facet. In the case of NW shells, such enriched edges extending in $\langle 11\bar{2}\rangle$ directions have been observed for (Al,Ga)As[154,155] and (Al,In)P.[156] In the case of (Al,Ga)As shells, clusters incorporated into these Al-rich edges have been proposed to lead to capture of charge carriers and strong optical emission.[154,157] Other results suggested that segregation layers on the (110) sidefacets are the origin for such emission from localized states.[158] Recently, these shell QDs have attracted much attention as potential single-photon emitters.[159,160] Such clusters might also form in (In,Ga)As shells, leading to emission from localized states.

5.2 Impact of growth parameters on luminescence properties of (In,Ga)As shells

The crystalline structure of real materials is disturbed to some extent by defects which can be point defects or line defects.[32] Line defects such as dislocations always have detrimental effects for devices. Point defects can be either native, such as vacancies, interstitials and antisites,[161] or extrinsic impurities such as dopants.[162] Such defects introduce distinct electronic states into the system, usually at energies within the band gap. These states give rise to specific optical emission energies or enhanced nonradiative recombination due to the Shockley-Read-Hall mechanism[163] particularly in the case of so-called deep states. Thus, luminescence experiments are a sensitive tool to analyze the

material quality concerning defects. Additionally the luminescence properties of QWs is affected by their structure. Important parameters are fluctuations in thickness[164,165] and alloy clustering[166] as well as inhomogeneous alloy composition profiles due to surface segregation during growth.[167] These structural properties as well as the incorporation of defects[168,169] depend crucially on the chosen growth parameters. In MBE the growth conditions can be controlled with high precision, enabling the exploration of optimized growth parameters for achieving materials of highest quality.

In this part, different sample series are discussed that were synthesized using either one of the two As cells installed at our MBE setup, called AsV1 and AsV2. In the exploration of the optimum growth parameters we focus on samples grown using AsV2 as these show significantly higher luminescence intensities. The role of the As sources is discussed in detail in the next section. However, for completeness we also show data of samples grown with AsV1. We note that the successful growth of (In,Ga)As shells has been shown previously including a discussion of the impact of the growth temperature,[17] but here we will discuss the impact of all growth conditions in more detail.

5.2.1 Growth temperature

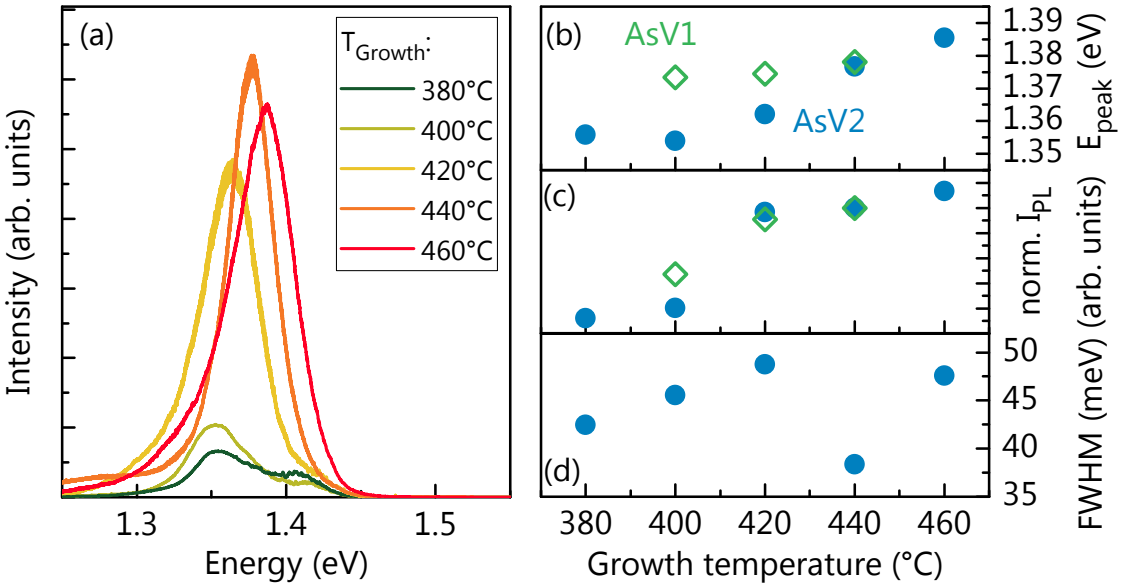

Figure 5.3: (a) PL spectra taken at 10 K and with excitation power P_{exc}=700 µW on samples with (In,Ga)As shells grown at different substrate temperatures using AsV2. Extracted values for (b) peak energy, (c) integrated intensity normalized to the value at 440 °C for both series, and (d) FWHM as function of growth temperature. Data points are shown for samples grown using AsV1 (green diamonds) and AsV2 (blue circles).

Figure 5.3(a) shows PL spectra taken at 10 K on samples with $In_{0.15}Ga_{0.85}As$ shells grown using AsV2 for different substrate temperatures as measured by the pyrometer.

The other growth parameters were maintained at $f_{Ga} = 6.8$ nm/min, $f_{In} = 1.3$ nm/min, and $R_{5/3} = 22$. All samples show main peaks at energies corresponding to luminescence from the $In_{0.15}Ga_{0.85}As$ shell and no luminescence is detected that might correspond to the GaAs core. However, for the samples with growth temperatures of 380 °C and 400 °C, a shoulder at energies higher than the main luminescence peak is detected. Figure 5.3(b) shows the peak energy for samples grown using both As sources. In both cases, the emission energy increases with increasing growth temperature, resulting in a blue-shift of 30 meV from 380 °C to 460 °C (for AsV2). This blue-shift might be related to surface segregation of In atoms on the growth front during shell growth. Instead of being incorporated, the In atoms remain on the growing surface leading to diffuse interfaces. It has been shown that this effect is temperature dependent, inducing a blue-shift with increasing temperature.[167] Figure 5.3(c) shows the normalized intensity as function of temperature. For both sample series, the intensity increases with increasing growth temperature. Figure 5.3(d) presents the FWHM of the PL spectra showing an optimum at 440 °C. The PL intensity of NW samples depends critically on the precise NW sizes (sample volume) and vertical yield, which might fluctuate slightly among samples. Therefore, we expect a significant error in the intensity values and we choose a growth temperature of 440 °C for most following experiments as this temperature results in high intensity and the best linewidth.

Homogeneity along the NW axis

Figure 5.4 shows cathodoluminescence (CL) spectroscopy line-scans along the axis of single NWs. The samples were grown at three different temperatures and for each sample, measurements of two NWs are presented. With this technique charge carriers are locally excited in the NW and the luminescence is measured globally. Figures 5.4(a) and (b) show scans on NWs from the sample grown at 400 °C. The luminescence is homogeneously distributed at the top 1 µm of the NW centred at 1.35 eV. The lower part of the NWs shows weak luminescence at slightly higher emission energy. Figures 5.4(c) and (d) show scans on NWs from the sample grown at 420 °C. In (c), the luminescence is centered at 1.34 eV for the top 1 µm. Also luminescence at lower energies is detected at the top. In (d), the luminescence is only intense at a localized spot at 1.5 µm height centred at 1.31 eV. Also luminescence at low energies is detected at the upper part of the NW. Figure 5.4(e) and (f) show scans on NWs from the sample with shell growth temperature of 440 °C. Here, only a weak luminescence signal is detected at the lower 1 µm of the NWs. At the upper part strong luminescence is detected centred at 1.37 eV. Additionally, in Figure 5.4(e), at the top of the NW strong luminescence at 1.32 eV is detected.

In summary, the CL measurements show that at the bottom 1 µm of all NWs only weak emission is detected at slightly higher emission energy compared to the rest of the NW. Also at the top of the NW (300–500 nm below tip) only weak luminescence is detected. The emission shift at the bottom of the NW and the low intensity at the top have been

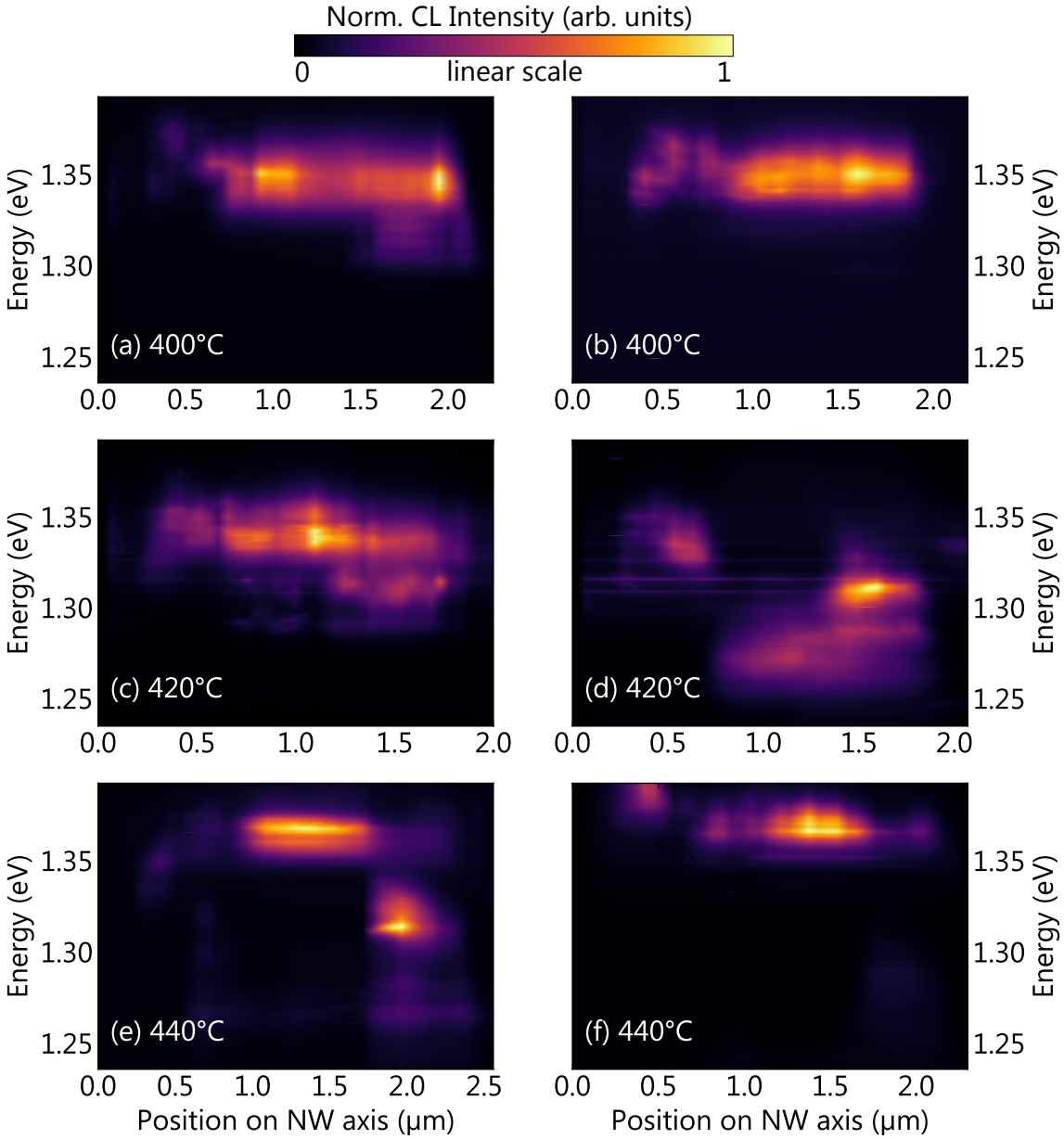

Figure 5.4: Cathodoluminescence scans taken at 10 K along the axis of two NWs each of three sample with shells grown at 400 °C (a,b), 420 °C (c,d), and 440 °C (e,f). The V/III ratio was 22 and the fluxes were $f_{In} = 440$ nm/h and $f_{Ga} = 78$ nm/h. All line scans are going from the bottom to the tip of the NW. The bright areas correspond to high intensity. Measurement performed by Uwe Jahn.

observed previously on similar samples[17]. The decrease in luminescence intensity at the bottom might be related to the bare facet at the bottom of the NW that was broken off from the substrate. Surface recombination might lead to rapid nonradiative recombination. In addition, typically many stacking faults are seen at the bottom and top part of NWs. These defects are not detrimental in itself but might induce the formation of defects during shell growth. Furthermore, for the highest growth temperature, the luminescence is detected at smaller parts of the NWs and variations of the emission energy along the NWs are detected. Additionally, the detected luminescence peaks seem to be narrower for higher growth temperatures compared to lower growth temperatures. These results indicate that for low growth temperatures the samples exhibit broad luminescence which is homogeneously distributed along the NW. In contrast, for high growth temperature, the samples show different sections over the NW length that have varying central energies but individually exhibit narrow luminescence peaks. In the PL of an ensemble of NWs, the FWHM was smallest for the sample grown at 440 °C, which is in agreement with the CL results, showing narrowest emission peaks. Also the sample grown at 420 °C shows varying emission energies in CL and the largest FWHM in PL. However, the FWHM for all samples was rather broad in the PL measurements with values of 38–48 meV. The results from the CL measurements suggest that the broad ensemble peaks are due to broad individual peaks for samples grown at low temperatures or varying central energies over the NW for samples grown at high temperatures. However, we want to remark that these measurements were done only on few single NWs that already show slight variations within a single sample, and therefore it might be too few to draw strong conclusions from these results.

5.2.2 As flux

Figure 5.5(a) shows PL spectra of samples grown using AsV2 at varying As fluxes resulting in different V/III ratios. The other growth parameters were maintained at $T_{growth} = 440$ °C, $f_{Ga} = 6.8$ nm/min, and $f_{In} = 1.3$ nm/min. All spectra show a single peak with varying intensity and position. Figure 5.5(b) shows the extracted peak positions from Gaussian fits to the main peaks. Values for samples grown using AsV1 are also shown, although for this series higher V/III ratios were used. However, for both series the maximum emission energy is detected at a $R_{5/3} = 30$. Figure 5.5(c) shows integrated intensities for both sample series. Here, the intensity of both series is normalized to the value at V/III ratio of 30, which is present in both series. As seen in the spectra, the intensity is highest for the sample with $R_{5/3} = 22$. Figure 5.5(d) shows the FWHM of the series grown with AsV2. There is a small variation showing the smallest linewidth at V/III of 22. Consequently, $R_{5/3} = 22$ was taken as the optimum value for highest intensity and narrowest peak width.

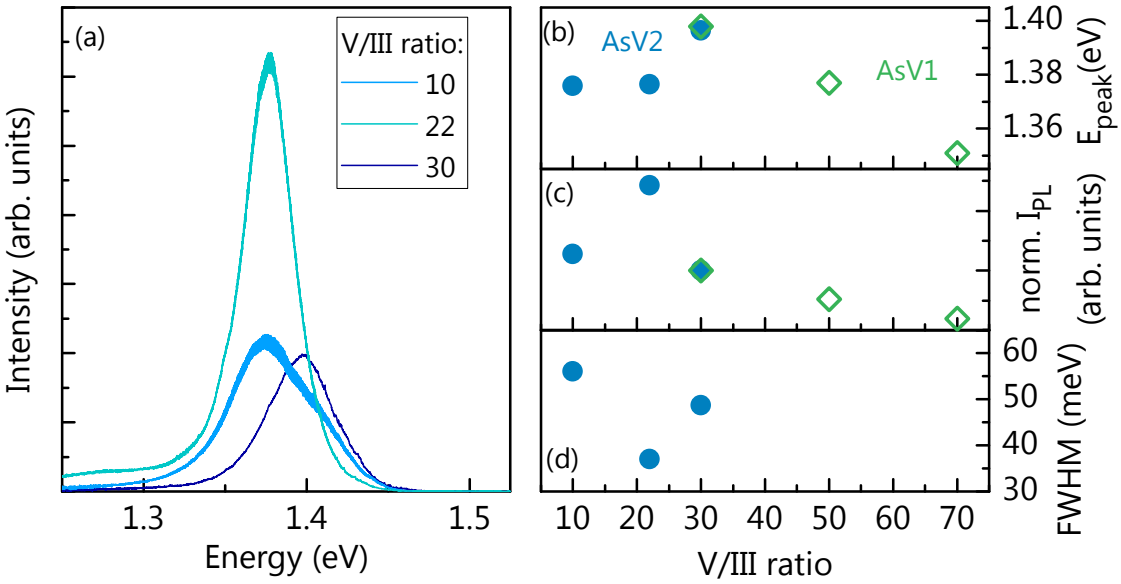

Figure 5.5: (a) PL spectra taken at 10 K and $P_{exc} = 700$ µW on samples with (In,Ga)As shells grown at different V/III flux ratios resulting from variation of the As flux using AsV2. The growth temperature was 440 °C for all samples. Extracted values for (b) peak energy, (c) integrated intensity normalized to $R_{5/3} = 30$ for both series, and (d) FWHM as function of V/III ratio. Data points are shown for samples grown using AsV1 (green diamonds) and AsV2 (blue circles).

5.2.3 Ga and In flux

Figure 5.6(a) shows PL spectra taken on samples grown using AsV2 and different Ga and In fluxes for the $In_{0.15}Ga_{0.85}As$ shell. The other growth parameters were maintained at $T_{growth} = 440$ °C and $R_{5/3} = 22$. The varying growth rate corresponds to varying amounts of deposited material per rotation of the substrate. The values are given in MLs on the (110) surface, taking into account the angle of the sources with respect to the substrate and the substrate rotation. The growth duration was adjusted such that the nominal thickness of all samples was equal. All spectra show a single peak with peak energies shown in Figure 5.6(b). Here, only a small variation is detected compared to the variation of the emission energy with growth temperature and V/III ratio. Figure 5.6(c) shows the integrated intensity of the spectra, exhibiting an insignificant variation among the different samples. Figure 5.6(d) shows the FWHM of the peaks, which decreases with increasing growth rate and seems to be optimal for the deposition of slightly below a full monolayer. The varying emission width implies that the $In_{0.15}Ga_{0.85}As$ shells are most homogeneous in terms of composition and roughness for the deposition of an almost complete monolayer per cycle (cf. chapter 2.1).

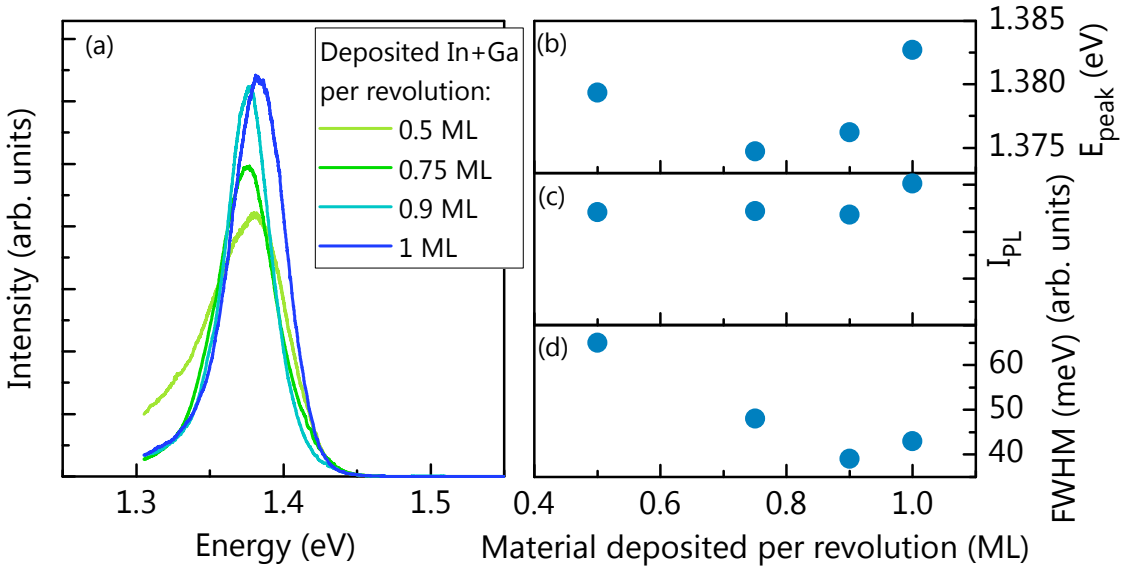

Figure 5.6: (a) PL spectra taken at 10 K and $P_{exc} = 700$ µW on samples with (In,Ga)As shells grown at different growth rates, corresponding to different amounts of material deposited on the NW sidewalls per substrate rotation using AsV2. A flux of 9.5 nm/min corresponds to one (110) monolayer per rotation on the sidewall. The growth temperature was 440 °C, the V/III ratio was 22 and the rotation speed 6 rpm. Extracted values for (b) peak energy, (c) integrated intensity, and (d) FWHM as function of deposited material per revolution.

5.2.4 Discussion of optimum growth conditions

As explained before, conformal growth of NW shells requires a low substrate temperature and a high V/III ratio. We found that a growth temperature of 440 °C and flux ratio of $R_{5/3} = 22$ result in optimal luminescence properties. These results agree with optimum growth conditions reported for growth on planar (110) substrates. These comprise a lower growth temperature and higher V/III flux compared to the typical growth conditions for axial NW growth and planar GaAs growth on (100) substrates (T_{growth} around 600 °C, V/III ratio below 10). We remind that also the six NW sidefacets of NWs grown in the Ga-assisted mode have $\{1\bar{1}0\}$ orientations. Figure 5.7 shows schematic diagrams of low index facets of zincblende GaAs.[170] These different facets have varying densities of atoms at the surface and different surface energies. The most typical substrate surface is the (100) facet, which is widely used for planar growth. The (111)B direction is the growth direction for GaAs NWs. Both of these facets show separate layers of Ga and As atoms and directed bonds. In contrast, for the (110) surface, Ga and As atoms are located stoichiometrically next to each other in each monolayer and no polar bonds to the next layer exist. Consequently, it has a low surface energy and is the cleavage plane of III-V semiconductors.[170] It was shown that this non-polar nature of the (110) surface leads to low sticking of As, impeding the growth of high quality material.[171,172] Two different solutions to this problem have been reported. First, substrates were used with a high offcut

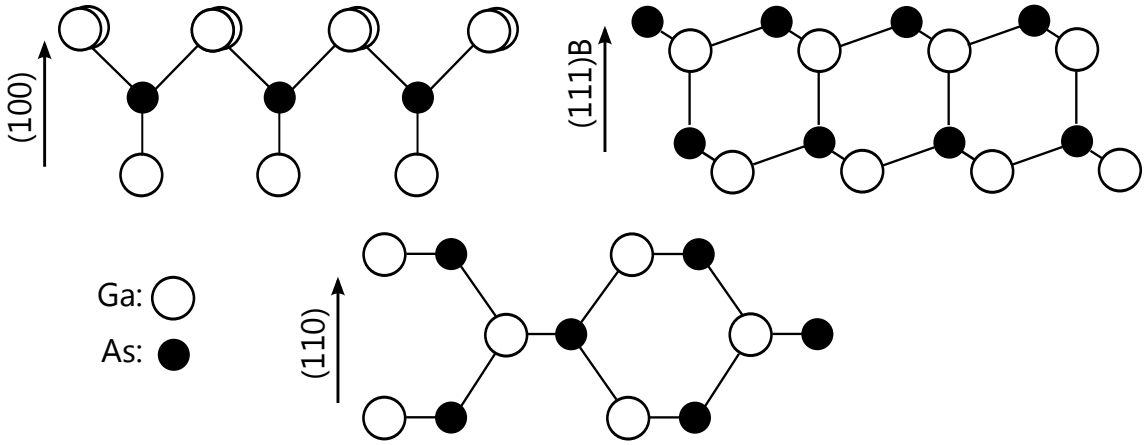

Figure 5.7: Ball and stick models of low index surfaces of the zincblende GaAs crystal in side-view: (100), (111)B, and (110). The white balls correspond to Ga atoms, the black balls to As atoms.

angle of several degrees in such a direction that Ga ledges were exposed. These ledges accommodate As atoms leading to a higher sticking factor and the small terrace width due to the high offcut angle suppresses island nucleation, both resulting in layers of high quality.[173–175] The second approach showed that by decreasing the growth temperature and increasing the As flux, GaAs layers of high quality could be realized on exact (110) surfaces.[176,177] Here, diffusion is reduced and surface roughening is minimized. Furthermore, additional growth interruptions with annealing cycles have been shown to improve the surface smoothness.[178] For the growth of NW shells, comparably low growth temperatures and high V/III ratios have been reported for doped GaAs[122] and (Al,Ga)As.[179] For (In,Ga)As shells it was shown that increasing growth temperatures result additional emission at lower temperatures, in agreement with our results, and an optimum growth temperature of 390 °C was concluded from an optimization of the luminescence characteristics measured by CL.[122] However, the synthesis of (In,Ga)As shells by MBE at substrate temperatures of 500 °C[143] and 570 °C[18] has also been shown but the resulting samples show broad luminescence peaks. In conclusion, we showed that a growth temperature of 440 °C and a V/III flux ratio of 22 are necessary to obtain best luminescence properties of (In,Ga)As shell samples.

We showed that the optimum combined flux of In and Ga was found to correspond to slightly less than one monolayer deposited per substrate rotation. For the growth of planar layers on (110) substrates it was shown that random nucleation of new islands is a crucial factor in the formation of rough surfaces.[180,181] In this context, it was presented that growth with low growth rates suppresses island nucleation, leading to smooth surfaces.[182] This understanding is in contrast to our results showing optimum luminescence properties for higher growth rates, which might indicate that the processes during shell growth are different from what is known for planar MBE growth.

5.3 Role of the flux directionality in MBE

The material fluxes in MBE impinge from different directions onto the substrate. While this characteristic has no effect on the growth dynamics for planar growth, for the growth of three-dimensional nanostructures, like nanowires, the sidefacets are exposed to different fluxes at different points in time.[148] This fundamental difference has been widely ignored so far. A year before starting the work on this thesis, the growth activities involving GaAs NWs at the Paul-Drude-Institut were transferred to a new MBE system. Even though experiments involving the growth of GaAs NWs and core-shell heterostructures showed favourable results in terms of microstructure, we could not reproduce the luminescence properties of the GaAs/(In,Ga)As core-shell structures obtained on samples grown in the previously used MBE system.[17] Only when we had the opportunity to install a second As source in the MBE system, we could explore the crucial impact of the flux directionality on the material quality of NW shells.

5.3.1 Growth with different As cells

Figure 5.8(a) shows PL spectra taken at 10 K on two NW core-shell samples with the same structure as discussed before. Both samples were grown using the exact same growth conditions, meaning the same growth procedure for the NW core template and the same growth temperature and fluxes for the growth of the shells (optimum values $T_{\mathrm{growth}} = 440\ ^{\circ}\mathrm{C}$, $f_{\mathrm{Ga}} = 6.8$ nm/min, $f_{\mathrm{In}} = 1.3$ nm/min, $R_{5/3} = 22$). The only difference between the two samples is the choice of As cell during shell growth. The PL spectra taken on these samples are strikingly different: For the sample grown with AsV2, an intense peak is detected at 1.37 eV. For the sample grown with AsV1, the spectrum consists of sharp lines in the spectral range of 1.30 eV to 1.40 eV. Furthermore, the intensity at the same excitation power is more than two orders of magnitude lower, as indicated by the magnification factor of 200 times that was necessary to present the spectrum in the viewgraph.

Figure 5.8 (b) shows spectra of two planar reference samples grown on n-type GaAs(110) substrates, containing an $In_{0.15}Ga_{0.85}As$ quantum well with the same thickness as the shell of the NW samples. These two samples were grown using the same growth conditions as for the NW shell growth. First, a 100 nm thick GaAs buffer was grown, then a 10 nm thick $In_{0.15}Ga_{0.85}As$ layer was grown at a growth rate of 340 nm/h, corresponding to the total incident flux on the NW sidewall during shell growth. Finally, a GaAs cap layer of 30 nm was grown. For all layers the substrate temperature was 440 °C and the V/III ratio was 20. In stark contrast to the NW samples, these spectra are very similar and show a peak at 1.34 eV with a FWHM of 20 meV and a broad peak centred at 1.50 eV. The first peak can be attributed to the $In_{0.15}Ga_{0.85}As$ QW, exhibiting a broad linewidth compared to planar (100) QWs as attributed to higher interface roughness and alloy clustering.[183,184] The second broader peak corresponds to luminescence from the n-type GaAs substrate. The

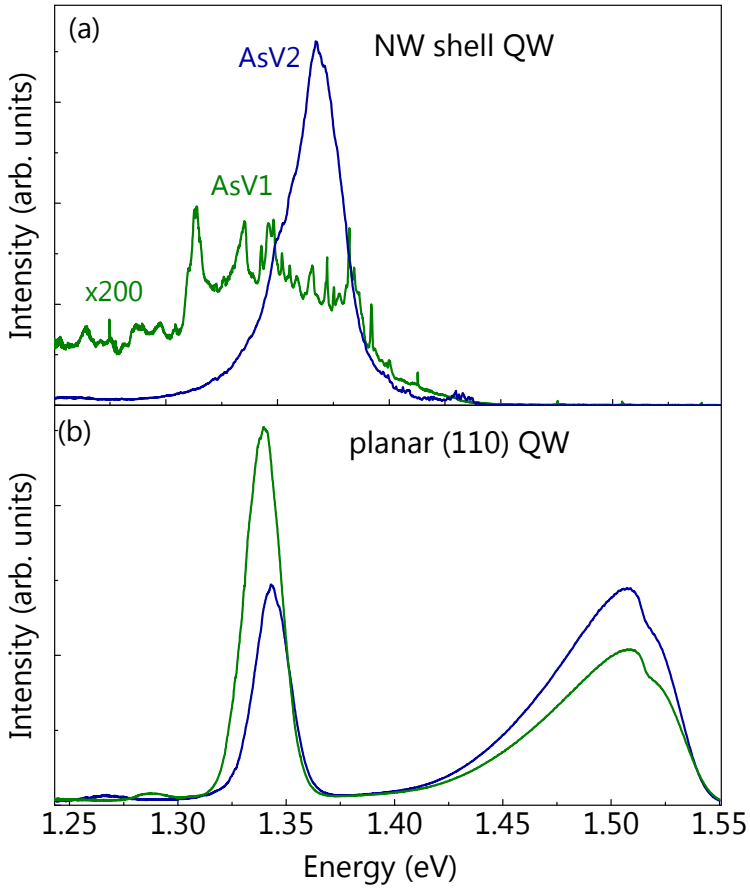

Figure 5.8: PL spectra taken at 10 K and $P_{exc} = 66$ µW on NW and planar structures grown with different cell configurations: (a) PL spectra taken on NW core-shell structures grown using the As sources AsV1 (green curve) and AsV2 (blue curve), respectively. The spectrum of the sample grown with the AsV1 is increased by a factor of 200. (b) PL spectra taken on planar (110) QW samples with a structure comparable to the shells of the NW samples. Also these samples were grown using AsV1 (green curve) and AsV2 (blue curve), respectively.

similarity of the two samples rules out a possible contamination of one of the As sources and indicates that the difference of the NW samples is inherent to shell growth.

Figure 5.9(a) shows a transmission electron micrograph of a single core-shell NW grown with AsV1. The image is acquired under dark-field conditions using the cubic (220) diffraction spot. The left side corresponds to the bottom part of the NW and on the right side the faceted top is visible. At the bottom of the NW, axial contrast features with high frequency are detected. These features are attributed to the presence of stacking faults and thin slabs of different crystal phases. In contrast, the upper part of the NW does not show clear axial contrast. Only the top of the NW shows deviations from a single crystal phase (like the bottom) due to the droplet consumption procedure. 5.9(b)–(d) show selective area electron diffraction measurements that were acquired to identify the different crystal phases. For the measurement at the bottom shown in Figure 5.9(b), diffraction

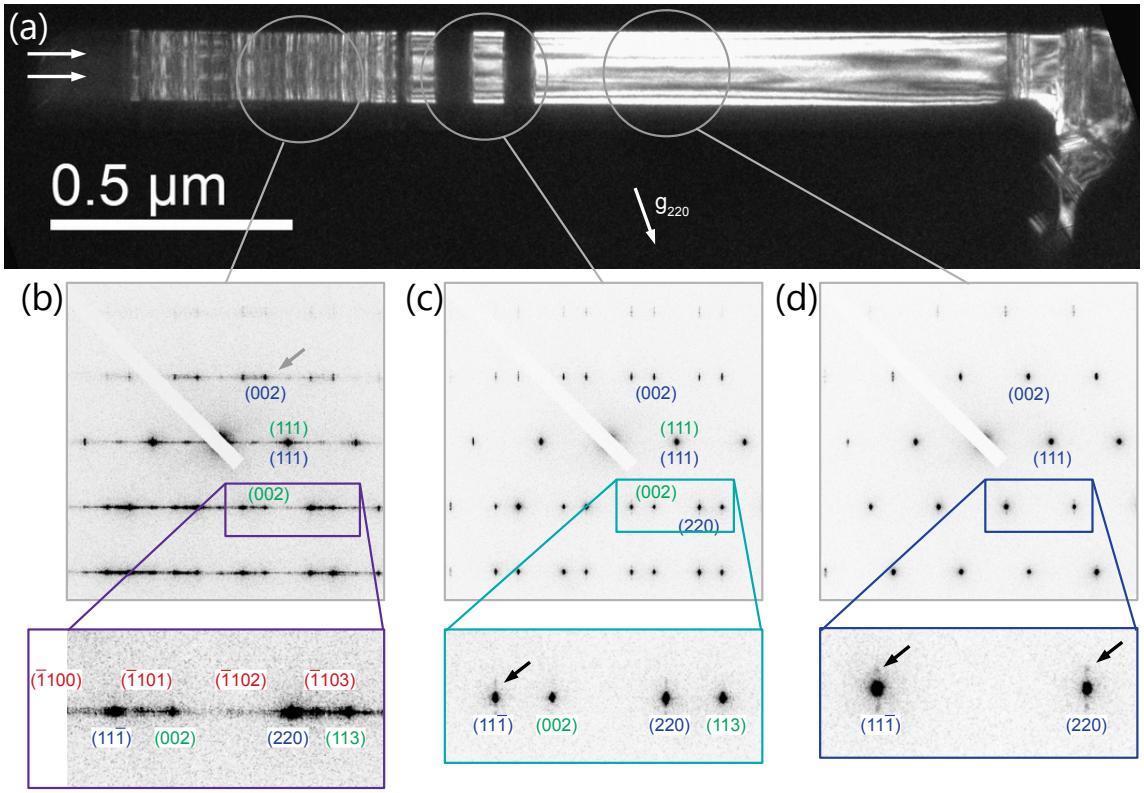

Figure 5.9: (a) Transmission electron micrograph taken in dark-field mode on a core-shell NW grown using AsV1. The three panels in (b), (c), and (d) show electron diffraction measurements at different positions of the NW. Here, the labels indicate the respective lattice vector in reciprocal space and the arrows indicate diffraction spots suggesting a coherently strained shell. Measurement and analysis performed by Achim Trampert and Michael Niehle.

from twinned cubic zincblende structure (blue and green notations), hexagonal wurtzite structure (red notations), and streaks along [111] are detected, that are attributed to stacking faults or thin slabs. Figure 5.9(c) shows the measurement at the central part, exhibiting diffraction from twinned zincblende segments (blue and green). Figure 5.9(d) shows the measurement at the top part of the NW where only a single zincblende phase is detected (blue). Interestingly, the magnifications of the electron diffraction images indicate that secondary spots above and below the $(11\bar{1})$ and (220) zincblende spots exist in Figure 5.9(c) and (d). Their position exactly above and below the main peaks corresponding to the radial direction indicate a coherent, elastically strained shell. Furthermore, no sufficient indications for plastic relaxation by dislocations are indicated in the micrograph, as the contrast along the NW width corresponds to thickness fringes due to the hexagonal shape of the NW. These results imply that dislocations are not causing the low luminescence intensity of the sample grown with co-deposition and therefore, we propose that a high density of point defects might be the origin for the low luminescence intensity. However, this result is only based on few TEM measurements and more work needs to

be done to distinguish the nature of the defects.

5.3.2 Inherent flux sequences

The two As sources are both VEECO 500 CC valved As crackers calibrated with the same procedure as discussed in section 2.1. The difference between the two As sources is only their location in the MBE system. Figure 5.10(a) shows a schematic diagram of the locations of the relevant cells in the MBE system. The In and Ga cells are located next to each other. The first As cell (AsV1) is the next neighbour of the In cell whereas the second As cell (AsV2) is exactly opposite of the In cell. The direction of the impinging fluxes relative to the sidefacet is defined by two angles: The first angle α is the azimuthal angle in the substrate plane between the normal of the NW sidewall and the direction of the effusion as shown in Figure 5.10(a). This angle α varies continuously due to the substrate rotation. The second angle β is the inclination angle of the cells with respect to the substrate normal, shown in Figure 5.10(b), which is fixed at 33.5° . The impinging flux on one sidefacet is calculated as

$$f_{\text{facet}}(t) = \begin{cases} f_{2D} \tan(\beta) \cos(\alpha(t) - \alpha_i) & \text{for } -90^\circ < \alpha < 90^\circ \\ 0 & \text{for } 90^\circ \leq \alpha \leq 270^\circ \,, \end{cases} \tag{5.1}$$

with the equivalent flux for planar growth f_{2D} and cell-dependent angle α_i to account for the relative positions of the sources. Figure 5.10(c) and (d) show the calculated fluxes, using the nominal fluxes as f_{2D} impinging on one sidefacet as a function of time for (c) AsV1 and (d) AsV2, with a constant rotation speed $\dot{\alpha} = 6\,\text{rpm} = 36^\circ/\text{s}$. In both sequences the Ga and In fluxes overlap widely due to the cells' location next to each other. Using AsV1 (c), there is also a large overlap of the As flux with the In and Ga fluxes. On the contrary, for AsV2 (d), there is no overlap of the As and In fluxes due to the opposite location of the cells to each other. Only for the Ga cell there is a small overlap with the As flux. Consequently, using AsV1 the material is mostly co-deposited, whereas using AsV2, As and In are never co-deposited.

The flux sequence with separate deposition of group III and As material [Figure 5.10 (d)] resembles shutter sequences that were used in migration enhanced epitaxy (MEE) of planar layers, where group III and group V fluxes are deposited after each other to increase the diffusion of the group III adatoms[185]. Particularly for growth on GaAs(110), the low As sticking factor demands low substrate temperatures and high V/III ratios[172,174,182] as discussed before. Here, MEE was employed succesfully for the growth of GaAs[186] and (In,Ga)As[187] layers on GaAs(110) with improved morphology and luminescence compared to layers grown by co-deposition. In particular, for the growth of (In,Ga)As (110) QWs it was shown that MEE can improve the compositional homogeneity.[184] It was suggested that the separate supply of group III species and As in MEE leads to the desorption of excess As and thereby avoiding the formation of (111) microfacets.[186] Fur-

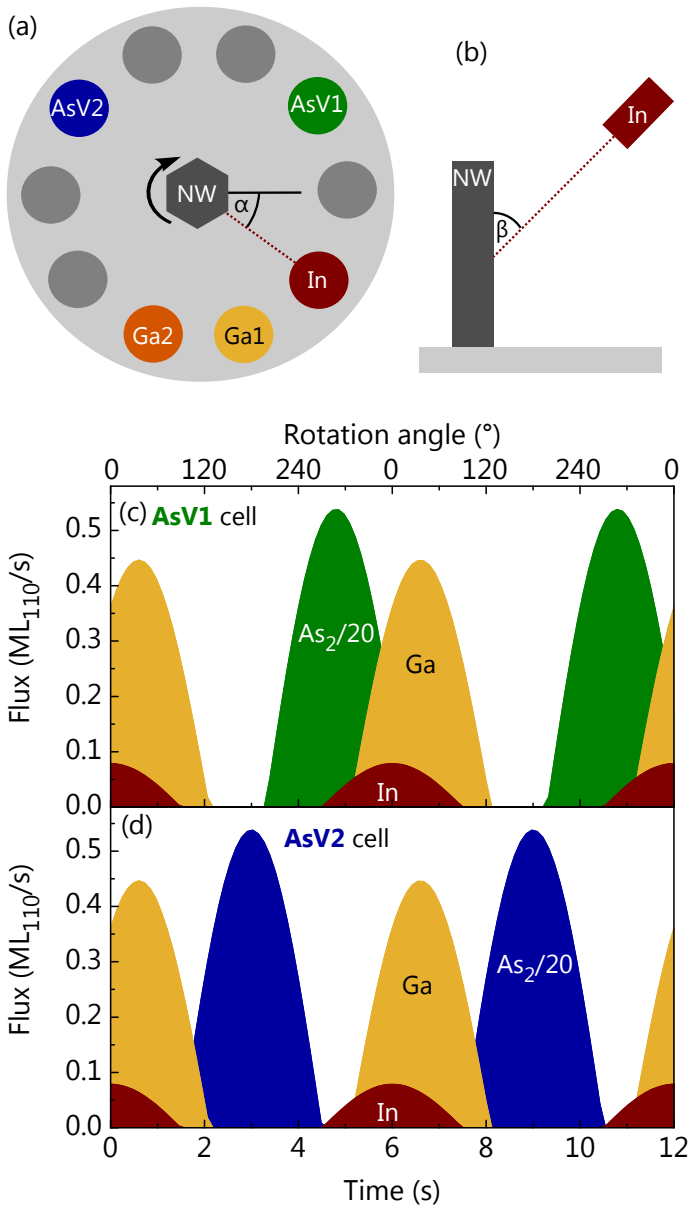

Figure 5.10: (a) Schematic of the cell configuration of the MBE system used for this study, as seen normal to the growth flange. (b) Schematic diagram of the flux impinging on the NW sidewall as seen from the side normal to the plane of NW and source. (c,d) Material fluxes impinging on a given side facet as a function of time and rotation angle as calculated by Equation 5.1, using (c) AsV1 and (d) AsV2.

thermore, it was proposed that the surface migration of As is also enhanced in MEE.[188] Here, the enhanced diffusion of Ga, In and also As might reduce the formation of native defects such as As antisites and Ga vacancies, that have been observed particularly for GaAs layers and NW shells grown at temperatures below 400 °C.[169,189] However, the exact mechanism that is responsible for the improvement by MEE and in particular for shell growth is not completely understood.

The similarity to MEE may also explain the impact of the growth rate on the material quality discussed in the previous section. For the growth of planar layers by MEE it was shown that the recovery of the intensity in RHEED during growth was fastest for deposition of complete MLs per cycle and oscillations were observed for incommensurate deposition, which indicated that the growth proceeds layer by layer.[190] Therefore, deposition of a full monolayer might lead to the smoothest layers. This result is in agreement with our observation of most homogeneous emission from samples grown with almost a complete layer deposited per rotation.

Our results suggest, that the co-deposition of materials during growth of NW shells could result in a high density of point defects, which has not been considered before. The remarkable difference of the samples grown with different As cells is much more drastic than reported differences between planar layers grown by continous MBE and MEE. Furthermore, the impact of the flux sequence is stronger than that of a change in growth conditions where only gradual variations were observed (cf. section 5.2). This result suggests that the growth of NW shells is inherently different from planar growth on defined surfaces. The biggest difference of NW sidewalls compared to planar substrates are the six NW edges. These edges have a surface bonding that differs from the (110) surface and most possibly lead to different growth kinetics. For the growth of (In,Ga)As shells with high In contents, it was shown that plastically relaxed clusters nucleate preferentially at these edges,[20] emphasizing the role of these edges. For the NWs discussed here, the edges always point in the $\langle 11\bar{2} \rangle$ directions. During shell growth, these edges may adopt the corresponding $\{11\bar{2}\}$ surfaces, as it was reported for (Al,Ga)As, (In,As)P, and InP shells.[154,191–193] This surface is polar, so a NW may exhibit three $\{112\}$A and three $\{112\}$B surfaces. For GaAs it was shown that these surfaces are unstable due to their high surface energy and decompose into lower energy facets, either into a combination of $\{111\}$ and $\{113\}$ facets or into $\{110\}$ facets.[194] The choice of the facets depends on the crystal polarity and the chemical potential. The (112)A facet transforms into $\{111\}$ and $\{113\}$ facets under Ga-rich conditions and into $\{110\}$ facets under As-rich conditions. For the (112)B facet it is the opposite behaviour. For such facets on the edges of the NWs, it means that during shell growth with co-deposition (using AsV1) the surface is always As-rich and the $\{112\}$A/B facets constantly favour either $\{110\}$ facets or $\{111\}$ and $\{113\}$ facets. This constant preference for certain facets might lead to the formation of microfacets leading to rough surfaces and the formation of defects. In contrast, during shell growth with separate deposition of group III materials and As (using AsV2) the surface conditions change continuously from group III-rich to As-rich. Under these

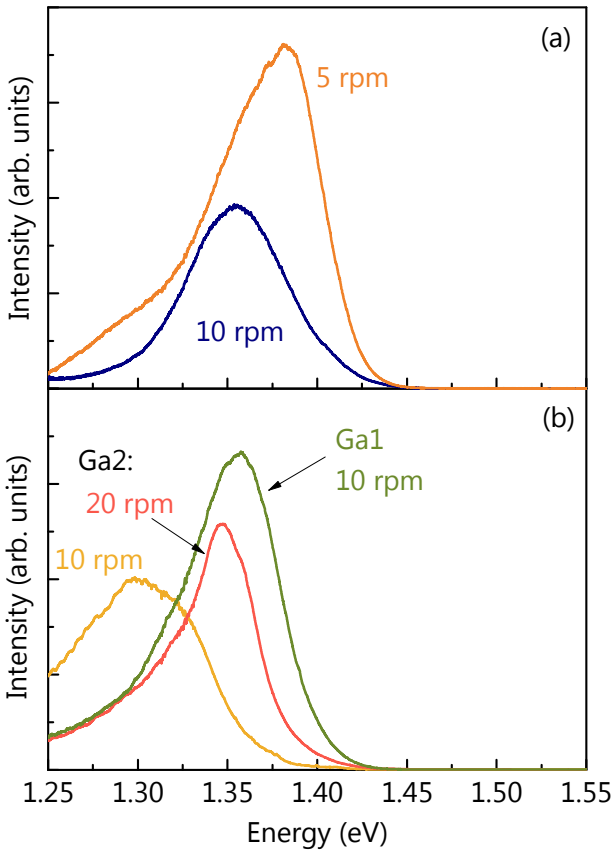

Figure 5.11: (a) PL spectra taken at 10 K and $P_{exc} = 700$ µW on samples with (In,Ga)As shells grown at varying rotation speed as indicated next to the curves. (b) PL spectra taken at 10 K and $P_{exc} = 700$ µW on samples with (In,Ga)As shells grown using different Ga sources (Ga1: green curve, Ga2: yellow and red curves) and varying rotation speeds (10 rpm: green and yellow curves, 20 rpm: red curve).

conditions, the energetically preferred facets alternate with the flux sequence, possibly suppressing their formation. This dependence of the facets on the flux sequence might be a possible explanation for the dramatic difference we observe in the experiment. A detailed investigation by TEM might elucidate the role of edge facets during growth.

5.3.3 Role of rotation speed and configuration of group III cells

Figure 5.11(a) shows PL spectra taken on $In_{0.15}Ga_{0.85}As$ shell samples grown with different rotation speeds. We note that the growth temperature and deposition rate are slightly lower than for the previously discussed samples ($T_{growth} = 420$ °C, $f_{Ga} = 2.9$ nm/min, $f_{In} = 0.5$ nm/min, $R_{5/3} = 22$). However, the sample grown with 10 rpm, the typical rotation speed used for all previously discussed samples, shows a symmetric peak centred at 1.35 eV. The sample grown at lower rotation speed of 5 rpm shows a peak centred at 1.38 eV with higher intensity compared to the first sample and a pronounced low-energy shoulder. By decreasing the rotation speed the amount of deposited material per rotation

increases from 0.36 ML for 10 rpm to 0.72 ML for 5 rpm. Thus, the sample with deposition closer to a complete layer exhibits the more inhomogeneous emission. This behaviour is in contrast to what we have seen for the samples grown with varying growth rate and constant rotation speed, shown in Figure 5.6. Consequently, we cannot attribute the observed changes in Figure 5.11(a) to the change in deposited material per rotation. Therefore, we suppose that the change in sequence length itself affects the growth dynamics during shell growth significantly. During In and Ga deposition, the adatoms diffuse on the growth surface to reach energetically favourable locations. If this period is too long, In-rich clusters may form, giving rise to a wider range of emission energies, as seen in the spectra. This result suggests, that even though the deposited amount per rotation and the rotation speed are connected, both parameters have a distinct impact on the growth dynamics.

Figure 5.11(b) shows PL spectra taken on samples with $In_{0.15}Ga_{0.85}As$ shells grown using Ga sources located at different cell ports. All fluxes and growth temperatures were the same for both samples ($T_{growth} = 440\ ^{\circ}C$, $f_{Ga} = 6.8$ nm/min, $f_{In} = 1.3$ nm/min, $R_{5/3} = 22$), but the samples were grown in a later growth campaign compared to the samples shown in section 5.2. Besides the Ga source that was used in all previous shell growth experiments, the system contains a second source for Ga, which we call Ga2 in the following discussion. The green curve shows the spectrum of the sample grown with source Ga1. It shows a central peak centred at 1.360 eV and a slight shoulder at lower energies. The yellow curve shows a spectrum of a sample grown with the same growth conditions using source Ga2. The spectrum shows a broad peak centred at 1.30 eV which corresponds to a red-shift of 60 meV relative to the sample grown with the source Ga1. The red curve shows the spectrum taken on a sample grown with the Ga2 source but with a higher rotation speed of 20 rpm. The spectrum shows a narrower peak centred at 1.345 eV which is shifted to higher energy by 45 meV compared to the sample grown with lower rotation speed.

The source Ga1 is located next to the In source whereas Ga2 is located next to Ga1 as visualized in Figure 5.10(a). Depending on which Ga source is used for the growth of (In,Ga)As shells, the flux sequence on the sidefacets changes. When using Ga2, the overlap of In and Ga fluxes is smaller than for using Ga1. The separate supply of In and Ga may lead to more segregation effects leading to cluster formation. Here, the separation is still small as the In and Ga2 sources are next-neighbours. For the hypothetical extreme case in which the Ga and In sources are located opposite of each other and Ga and In are never co-deposited, a strong clustering effect would be obvious. This effect might explain the red-shift in the PL spectra. By increasing the rotation speed the durations of the separate supplies are reduced which might lead to more intermixing and thus, potentially explaining the blue-shift of the sample grown with higher rotation speed. These results indicate that not only the relative location of group III and group V cells is crucial for the material quality but also the relative location of the group III cells to each other is important for achieving a homogeneous alloy.

5.4 Conclusion

We have explored the optimum growth conditions to achieve $In_{0.15}Ga_{0.85}As$ shells of highest material quality. A low growth temperature and high V/III ratio are necessary to achieve conformal shell growth and high luminescence intensity. These results are in agreement with the requirements for growth of planar layers on (110) substrates. Additionally, we have shown that a trade-off exists between luminescence intensity and homogeneity along the axis. It seems that for increasing growth temperature separate segments along the NW axis give rise to luminescence at varying emission energies, whereas samples grown at lower temperature show constant emission energies along the NW. However, in ensemble PL measurements, the emission width is comparable.

Furthermore, we have shown that the directionality of the material fluxes in MBE has a crucial impact on the quality of core-shell structures. Only in the case of oppositely located group III and As cells we could achieve samples with good luminescence properties. For this case we expect a flux sequence on the NW sidefacets that resembles MEE, which is known to improve layer smoothness and homogeneity. However, the effect is much stronger for NW shells than for planar layers. Furthermore, we showed that also the growth rate and rotation speed have significant impact on the growth dynamics. These results suggest that the growth of NW shells in MBE is drastically affected by the inherent flux sequence. Therefore, parameters become crucial that have no relevance for the growth of planar layers. We expect that these effects are present for growth of NW shells of all material systems, but the consequences may vary depending on the specific material properties. Not only adatom diffusion but also desorption might be affected, changing growth dynamics and material quality.

6 Impact of outer shell structure and localization effects on charge carrier dynamics in (In,Ga)As shell quantum wells

The large surface to volume ratio of NW structures emphasizes the importance of the surface for the electronic properties of such structures. At semiconductor surfaces, dangling bonds are formed which may result in distinct electronic levels within the band gap, so-called surface states.[32] In the case of GaAs, surface states are enhanced by oxidation under air exposure.[195,196] As surface states may lead to rapid recombination of charge carriers due to Shockley-Read-Hall recombination, they are detrimental for electronic and optical properties. Therefore, the passivation of surface states is particularly crucial in the case of NWs. This can be done by surface nitridation in wet chemistry[197] or by the epitaxial growth of shells of materials with a higher band-gap energy which typically yields a better sample quality. These shells act as barriers for the charge carriers in the NW core and prevent them from reaching the surface. In recent years, barrier shells of different materials have been explored for the surface passivation of GaAs NW, such as (Al,Ga)As,[198–200] Ga(As,P),[9] GaP,[201] (In,Ga)P,[202] and (In,Al)As on (In,Ga)As NWs,[193] typically yielding an improvement of the luminescence intensity in the range of one to two orders of magnitude. Also for the case of shell QWs, it can be expected that their luminescence efficiency is crucially affected by passivating outer shells. Therefore, we explore in this chapter the impact of different outer shells on the charge carrier dynamics in (In,Ga)As shell QWs.

In section 6.1, we show that at low temperatures, PL spectra are dominated by recombination of localized excitons. We attribute the localization to alloy clusters and thickness fluctuations discussed in the previous chapter.

In section 6.2, we show that due to the large surface-to-volume ratio, thermal emission of carriers from the QW and subsequent recombination at the surface is the major path of nonradiative recombination at elevated temperatures. By adding AlAs barriers we suppress this channel efficiently and achieve strong room-temperature luminescence.

In section 6.3, we present time-resolved PL experiments which show that the interface between the (In,Ga)As shell and the barrier determines the nonradiative decay of charge carriers at low temperatures. Therefore, a GaAs spacer shell of sufficient thickness is

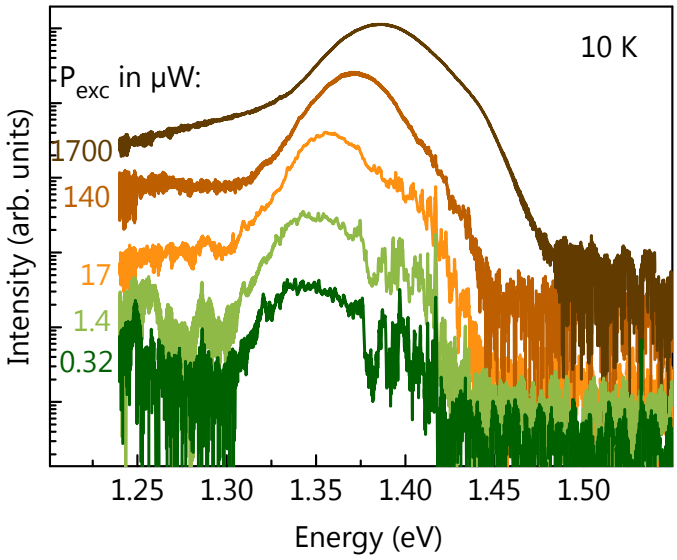

Figure 6.1: Low-temperature PL spectra taken on a sample with outer GaAs shell at different excitation powers as indicated next to the respective curves.

necessary to separate the QW from the barrier.

6.1 Localized states in the (In,Ga)As shell quantum well

Figure 6.1 shows PL spectra of a NW core-shell sample with $In_{0.15}Ga_{0.85}As$ shell quantum well taken at 10 K for various excitation powers. The structure is similar to what has been discussed in chapter 5, i.e. a 50 nm thick GaAs core, grown on a patterned Si substrate, a 10 nm thick $In_{0.15}Ga_{0.85}As$ shell, and a 30 nm thick GaAs shell. The shells were grown at the optimized growth conditions for optimum luminescence properties ($T_{growth} = 440\ ^{\circ}C$, $f_{Ga} = 6.8$ nm/min, $f_{In} = 1.3$ nm/min, $R_{5/3} = 22$). For low excitation power, the spectra consist of a continuous band centered at 1.35 eV and another band of spectrally resolved narrow lines centered at 1.40 eV. Both bands shift to higher energies with increasing excitation power. For the highest excitation power, the two bands evolve into a single peak with FWHM of 50 meV centered at 1.39 eV and a shoulder at 1.44 eV. No luminescence from GaAs is detected, not even at high excitation power, indicating an efficient transfer of charge carriers from the GaAs core to the (In,Ga)As shell QW as observed previously[5].

We attribute the first band to luminescence from localized and free excitons in the $In_{0.15}Ga_{0.85}As$ shell QW. The sharp transitions (FWHM < 1 meV) detected at low excitation power indicate localization by potential minima in the shell QW, typically either due to fluctuations in QW thickness or alloy composition. The band at higher energy is due to localized excitons as well, located at shell QWs with lower In content either at different facets of a single NW or a different NW. Such differences in In content of few percent have been shown to occur in similar structures.[151] For (Al,Ga)As shells, local-

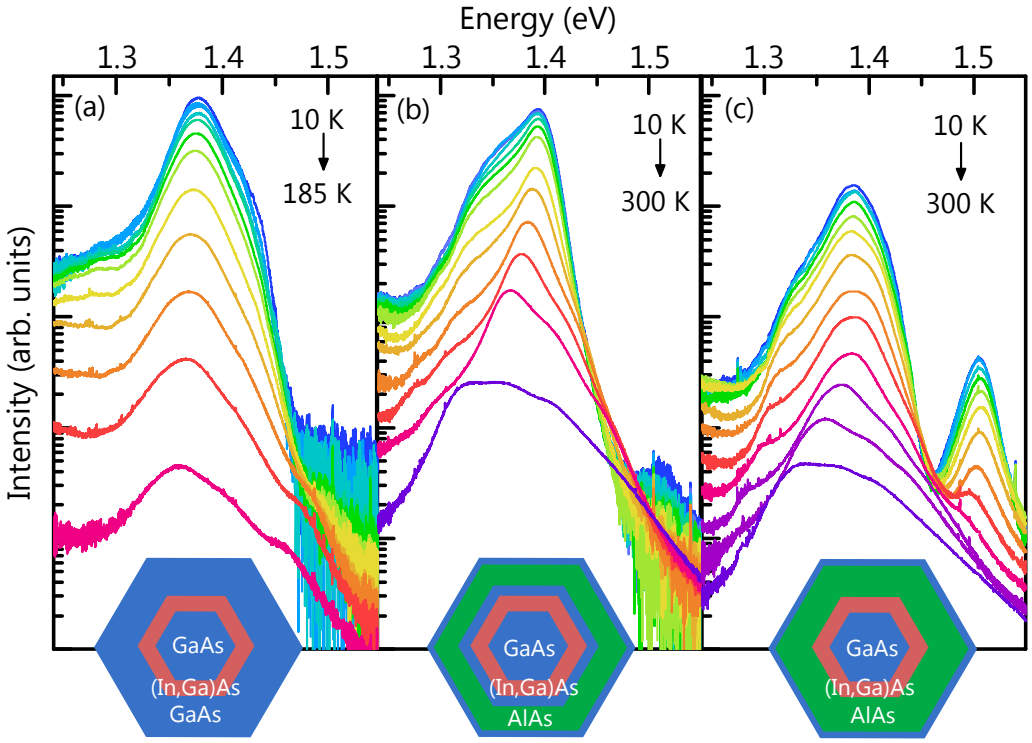

Figure 6.2: PL spectra taken at varying temperature on three samples with different structures as shown by the schematics at the bottom: (a) GaAs outer shell, (b) GaAs/AlAs/GaAs outer shells, and (c) AlAs/GaAs outer shell. The core and (In,Ga)As shell is the same for all samples. The intensity scale is the same for all three viewgraphs.

ization by potential minima due to segregation effects beyond random alloy fluctuations has been studied in great detail.[154,160,203] Also for the growth of planar (In,Ga)As QWs by MBE it was shown that roughness and compositional inhomogeneity are stronger for growth on the (110) plane compared to the more common (100) plane.[183,184] Another source for localization sites might be crystal-phase-quantum-rings (CPQRs) which form at the intersection of the QW and zincblende/wurtzite (ZB/WZ) interfaces given by a polytypic NW core.[5]

6.2 Thermal quenching of luminescence intensity

Figure 6.2(a) presents PL spectra taken on the same sample as in Figure 6.1 at temperatures between 10 and 185 K at an excitation power of 700 µW. For this excitation power, no PL could be detected at temperatures above 185 K. The structure of the NW cross-section of this sample is shown at the bottom. For all temperatures up to 185 K, a single peak dominates the spectrum, which is centered at 1.375 eV at 10 K. The shoulder at slightly higher energies is detected up to 100 K.

Figure 6.2(b) and 6.2(c) show PL spectra taken on samples with AlAs shell containing

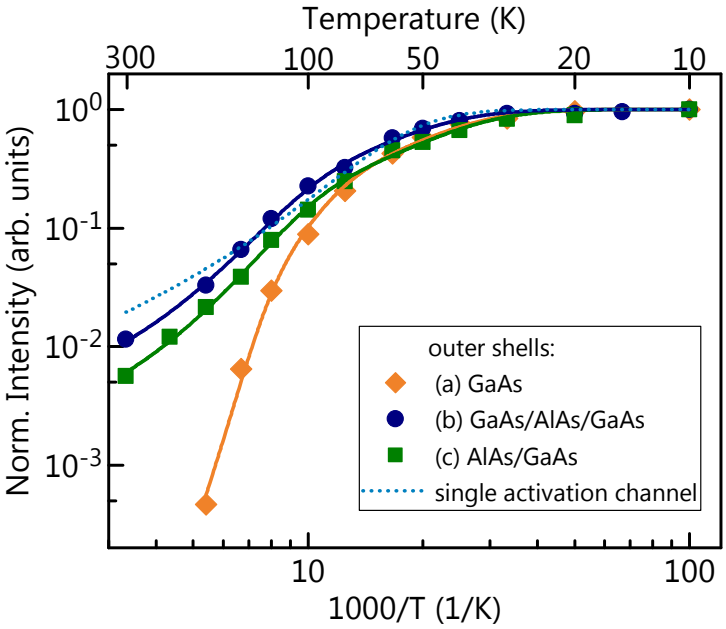

Figure 6.3: Normalized integrated intensity of the spectra shown in Figure 6.2 of the three different samples as a function of temperature. The lines show fits to Equation 6.1, yielding different activation energies as shown in Table 6.1.

structures for temperatures between 10 K and 300 K. Here, the core and $In_{0.15}Ga_{0.85}As$ shell are nominally the same as for the sample discussed so far, only different outer shells were grown around the $In_{0.15}Ga_{0.85}As$ shells at similar growth conditions (T_{growth} = 440 °C, f_{Ga} = 6.8 nm/min, f_{Al} = 3.4 nm/min, $R_{5/3}$ = 20): (b) a stack of 5 nm GaAs, 20 nm AlAs, and 10 nm GaAs, and (c) 20 nm AlAs and 10 nm GaAs. The respective core-shell cross-sectional structures are shown at the bottom of the viewgraphs. Here, we chose the binary compound AlAs to avoid additional localization effects in (Al,Ga)As shells.[154,203] For the sample with GaAs spacer in Figure 6.2(b), the spectra show a dominant peak centered at 1.39 eV, corresponding to emission from the (In,Ga)As shell QW. Also a shoulder at lower energies exists. For the sample without GaAs barrier shown in Figure 6.2(c), the spectra are also dominated by a peak at around 1.38 eV, corresponding to emission from the (In,Ga)As shell QW. This transition is slightly broader and almost one order of magnitude weaker than for the sample with GaAs spacer. For this sample, an additional peak at around 1.50 eV is detected, which most probably corresponds to emission from the strained GaAs core. Only for this sample emission from the core is detected, indicating that the carrier transfer from the core to the shell QW is less efficient in this structure. A possible explanation for this phenomenon is that for this sample the AlAs is next to the QW shell, changing the confinement of charge carriers in the QW due to its high band-gap energy and their wavefunctions are pushed further into the GaAs core. This might give rise a less efficient transfer into the shell and luminescence from the GaAs core.

Sample	E_1 (meV)	E_2 (meV)	E_3 (meV)
AlAs/GaAs	5 ± 1	38 ± 2	
GaAs/AlAs/GaAs	7 ± 2	35 ± 3	
GaAs	6	37	150

Table 6.1: Parameters obtained by the analysis of the intensity shown in Figure 6.3 using Equation 6.1. For the sample with GaAs outer shell no errors are given as these values were not obtained by a fit.

Figure 6.3 shows the normalized intensities, integrated over the entire emission band, for the three samples as a function of temperature. For temperatures from 10 to 80 K the intensity decreases in a similar way for all samples: The intensity is almost constant at low temperatures, and starts to decrease more rapidly for temperatures above 40 K. Above 80 K the sample with GaAs outer shell shows a strong, thermally activated quenching of the PL intensity. At 185 K the intensity has decreased by more than three orders of magnitude. In contrast, for samples with AlAs outer shells (green and blue data points), the intensity decreases much less compared to the sample with GaAs shell for temperatures above 80 K. Even at room-temperature the intensity is still 1% of the low-temperature intensity. This value is comparable to what has been shown for planar (100) (In,Ga)As QWs surrounded by (Al,Ga)As barriers[204] and GaAs/(Al,Ga)As core-shell NWs.[203,205] This result shows, that the incorporation of an AlAs shell in the outer shell structure drastically improves the luminous efficiency at room temperature.

A thermally activated quenching of the PL intensity can be written as

$$I(T) = 1/[1 + \sum_i a_i T \exp(-E_i/\mathrm{k_B}T)] \tag{6.1}$$

with the activation energies E_i of different nonradiative recombination channels, the prefactors a_i and the Boltzmann constant k_B.[206] Here, we have taken into account the linear temperature dependence of the radiative lifetime of carriers in QWs.[207] The lines in Figure 6.3 show fits of Equation 6.1 to the data, yielding activation energies presented in Table 6.1. The dotted line shows a fit using only one activation channel, deviating significantly from the experimental data. Therefore, for the samples with AlAs barriers, the analysis requires two recombination channels with distinct activation energies: At low temperature an activation energy of around $E_1 = 6 \pm 2$ meV and for elevated temperatures a second activation energy of $E_2 = 37 \pm 3$ meV.

The first recombination channel at low temperatures might originate from dissociation of free excitons, whose binding energy in such QWs is similar to E_1,[208,209] or a thermally activated delocalization of excitons localized by potential fluctuations. The activation energy of $E_1 = 6$ meV, corresponds to fluctuations of the In content of around 0.6%. Such variations in In content have been shown by a microstructural investigation of similar

structures.[151] Segregation effects that are beyond random alloy fluctuations are known to exist for growth in the (110) direction[184] and can partly explain the broad peaks with full-width at half maximum of above 30 meV for all samples.

The second channel with $E_2 = 37$ meV is more difficult to interpret. The value of the activation energy is about twice as large as those reported for closely lattice-matched GaAs/(Al,Ga)As[142,203,205] and (In,Ga)As/(In,Al)As[193] core-shell NWs, which was speculated to be related to a specific recombination center at the $\{110\}$ interfaces. In the present case, it seems unlikely that this nonradiative channel is related to an interfacial defect, since we obtain exactly the same value for E_2 for samples with an interface to an outer GaAs or AlAs shell. Rather, we believe this activation energy to be characteristic for $In_{0.15}Ga_{0.85}As$ grown under the conditions employed in the present study (low temperature, high V/III ratio).

For the sample with GaAs outer shell, a third activation channel is required to reproduce the experimental data, as the intensity is quenched more strongly at higher temperatures. This strong thermal quenching is adequately described by a channel with an activation energy of $E_3 = 150$ meV, with E_1 and E_2 having the same values as for the samples with an outer AlAs shell as the corresponding channels comprise effects that originate from the core and (In,Ga)As shell QW. The value of E_3 is close to the energy difference between the GaAs band gap and the peak energy of the emission from the $In_{0.15}Ga_{0.85}As$ shell QW. Therefore, we assume that the this recombination channel is due to thermal transfer of carriers from the (In,Ga)As shell QW to the outer GaAs shell, leading to rapid nonradiative recombination at the outer surface, analogously to planar QWs.[204,210] These results show that by introducing a high energy barrier around the (In,Ga)As shell QW the carrier transfer to the outer shell effectively decreases, resulting in a high room temperature luminescence intensity.

6.3 Exciton dynamics in the shell quantum well at low temperature

To explore the carrier dynamics at low temperatures in more detail we measured time-resolved PL. Figure 6.4(a) shows normalized intensity transients of the spectrally integrated PL bands from the $In_{0.15}Ga_{0.85}As$ shell QWs for all three samples at 10 K. The excitation wavelength was 750 nm and excitation power 250 µW. For excitation and collection the same objective was used as for cw experiments. All transients show a non-exponential decay, characterized by a fast decay during the first 500 ps and a slower decay for longer times. We assume that the fast decay is due to nonradiative decay with varying decay times for the different samples. In order to corroborate this assumption, we build a model which is based on the understanding obtained by the analysis of the cw-PL data. We assume that the luminescence is dominated by excitons, given the exciton binding energy of around 8 meV for such a QW[209] and the low temperature of 10 K.

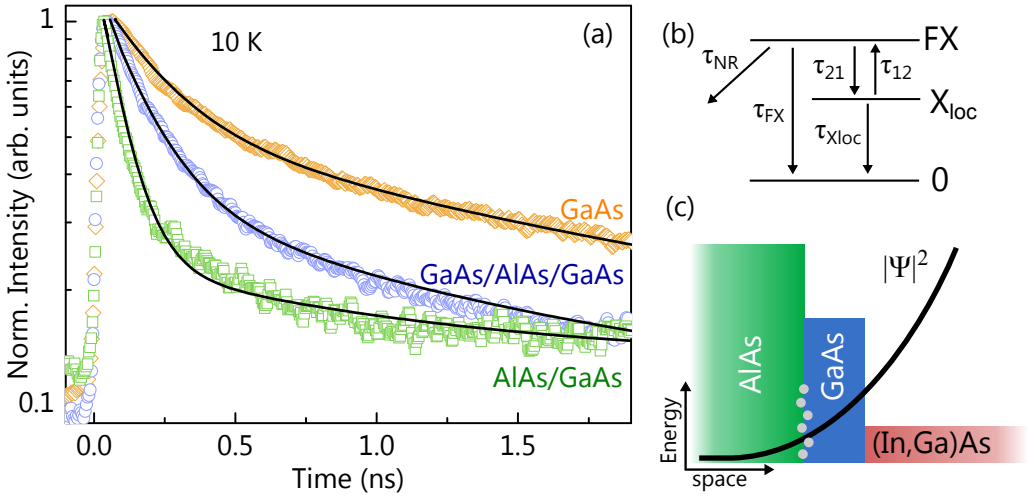

Figure 6.4: (a) Transients of the low temperature PL intensity taken on different samples as indicated next to the data points. The lines are simulations of Equation 6.4 to the experimental data, yielding parameters given in Table 6.1. (b) Schematic of the model of exciton states used to describe the transients. (c) Sketch of the exciton probability distribution at the outer interface region of the (In,Ga)As shell QW. The exciton penetrates into the defective AlAs/GaAs interface region leading to enhanced nonradiative decay.

We only consider heavy-hole excitons. Figure 6.4(b) shows a schematic of our model: As we have seen, at low temperatures the PL is determined by excitons localized at potential fluctuations (X_{loc}) as well as free excitons in the (In,Ga)As shell QW (FX). Free excitons are captured by the localized states with rate $1/\tau_{21}$. Also, localized excitons can transfer to free states with rate $1/\tau_{12}$. Excitons of both states contribute to emission of light, characterized by the radiative lifetimes τ_{FX} and τ_{Xloc}. Finally, we suppose that only the free excitons can recombine nonradiatively with nonradiative lifetime τ_{NR}. The corresponding rate-equations are given by

$$\frac{dn_{FX}}{dt} = -\frac{n_{FX}}{\tau_{FX}} - \frac{n_{FX}}{\tau_{NR}} + \frac{n_{Xloc}}{\tau_{12}} - \frac{n_{FX}}{\tau_{21}} \tag{6.2}$$

$$\frac{dn_{Xloc}}{dt} = -\frac{n_{Xloc}}{\tau_{Xloc}} - \frac{n_{Xloc}}{\tau_{12}} + \frac{n_{FX}}{\tau_{21}} \tag{6.3}$$

giving rise to the detected luminescence which depends on the radiative lifetimes

$$I_{PL}(t) \propto \frac{n_{FX}}{\tau_{FX}} + \frac{n_{Xloc}}{\tau_{Xloc}}, \tag{6.4}$$

with number density of free excitons n_{FX} and localized excitons n_{Xloc}, and time-dependent PL intensity $I_{PL}(t)$. The lines in Figure 6.4(a) show simulations of Equation 6.4 with the parameters shown in Table 6.2, with $n_{FX}(0) = 1$ and $n_{loc}(0) = 0$. For the simulations, we assumed that only τ_{NR} changes between the different samples and all other lifetimes and transfer times are constant. Both radiative lifetimes are the same for all samples as

Sample	τ_{NR}	τ_{FX}	τ_{Xloc}	τ_{12}	τ_{21}
GaAs	1.8	1.3	3.5	1.2	0.5
GaAs/AlAs/GaAs	0.33	1.3	3.5	1.2	0.5
AlAs/GaAs	0.11	1.3	3.5	1.2	0.5

Table 6.2: Lifetimes and transfer times (all in ns) obtained by the analysis of the transients in Figure 6.4(a), corresponding to the system shown in Figure 6.4(b) and the Equations 6.2–6.4.

they only depend on In content and clustering in the (In,Ga)As shell QW[211,212], which is the same for all samples. Despite the simplicity of the model and the fact that we have varied only one parameter, the experimental data are reproduced fairly well, thus confirming our hypothesis.

Regarding the accuracy of the model we estimate that similar results can be achieved with parameter values estimated within $\pm$20% of the values presented in Table 6.2. The extracted radiative lifetime of free excitons is 1.3 ns, noticeably longer than typical values of about 400 ps reported for planar (In,Ga)As/GaAs(100) QWs,[209,213,214] indicating an increased spread of excitons in *k*-space that hinders the effective radiative recombination[212], possibly due to a high carrier temperature that was reported previously for different NWs.[215] The radiative lifetime of the localized exciton is 3.5 ns, a value also longer than lifetimes reported for GaAs/(Al,Ga)As shell QDs ranging between 450 ps[154] and 1.7 ns.[5] For unintentionally grown (In,Ga)As shells around nanopillars grown by MOCVD lifetimes of below 500 ps were reported, not differentiating between radiative and nonradiative decay.[216]

The transition time τ_{12} is 1.2 ns, which is reasonably long, as the thermal transfer from the localized to the free state is impeded at low temperatures. The capture time τ_{21} on the other hand is 0.5 ns, which is shorter than expected, as such capture times in GaAs QWs have been shown to be only 250 ps for samples of highest quality.[217] This effect might be related to the slow relaxation dynamics reported for NWs[203,215].

As we have assumed, the different transients can be explained by a variation of τ_{NR}. We attribute this variation to different recombination velocities at the interface of the (In,Ga)As shell QW with the outer shell. In particular, we expect a high density of point defects at the $In_{0.15}Ga_{0.85}As$/AlAs interface because of the low growth temperature. Remarkably, also for the sample with the 5 nm GaAs spacer between the $In_{0.15}Ga_{0.85}As$ and AlAs shells, τ_{NR} is significantly lower than for the samples with pure GaAs shell. Figure 6.4(c) shows a sketch of the exciton probability distribution in the outer interface region of the $In_{0.15}Ga_{0.85}As$ shell QW. Here we suppose that the exciton penetrates through the thin GaAs spacer shell and into the defective GaAs/AlAs interface region. This effect can explain the smaller τ_{NR} compared to the sample with pure GaAs outer shell.

6.4 Conclusion

We have shown that the low temperature luminescence of (In,Ga)As shell QWs is strongly affected by emission from localized states. The extracted activation energies for delocalization suggest that In content fluctuations that are beyond random alloy fluctuations are the origin. To understand the structure of these localization sites in more detail and compare them to what is known for (Al,Ga)As shell QDs further investigations are necessary. Furthermore, we showed that by adding an AlAs barrier shell the room temperature luminescence of the shell QWs increases dramatically. However, the interface to the AlAs shell is found to introduce an additional nonradiative recombination channel that is active already at low temperatures. This result emphasizes the importance of interfaces for carrier recombination in core-shell heterostructures. Here, the introduction of a thin GaAs spacer shell between the QW shell and the barrier increases the nonradiative lifetime but the exciton wavefunction still penetrates the 5 nm thick spacer shell, limiting the improvement. Hence, our study illustrates competing factors limiting the PL intensity in NW shell QWs. Using a multishell design, we demonstrate a way to reduce the impact of this interface and to achieve NW shell QWs with high luminous efficiency, enabling efficient devices operating at room-temperature.

7 Ex-situ annealing of core-shell nanowires

In the previous chapter, we have shown that $In_{0.15}Ga_{0.85}As$ shells exhibit alloy clustering, leading to localization of carriers at low temperatures and broad luminescence peaks. This clustering, which is beyond random alloy fluctuations, is partially related to the distinct growth mode based on the inherent flux sequence that we have discussed in chapter 5. Furthermore, the nature of the (110) surface that is present at the NW sidefacets leads to rough facets and segregation effects in general.[175,180,183,184] These limitations are inherent to the material system and the growth on NW sidewalls. Therefore, the optimization of the growth parameters in chapter 5 was limited in obtaining highest optical properties. A prominent approach to improve the homogeneity of materials and reduce the density of defects after growth is ex-situ rapid thermal annealing (RTA).[218–221] By applying annealing temperatures much higher than temperatures used during growth the migration of defects and intermixing of alloys is thermally activated.[222] However, in the case of NWs this process has not been used in a wide range[223] because the large surface to volume ratio leads to enhanced evaporation at the surface for high temperatures.[224] In the case of planar layers, this effect was typically avoided by using an additional substrate on top of the grown layer to prevent excessive evaporation from the grown layer but this method cannot be used for NWs. Here, we present a successful strategy to protect the NWs by a thin SiN_x layer during ex-situ annealing at temperatures of up to 900 °C.

In section 7.1, we present the processing steps involved in the annealing of the NW core-shell structures. We show that the SiN_x is deposited conformally around the NW and is thermally stable up to at least 900 °C. After annealing this SiN_x cap is etched selectively to the GaAs and the NWs exhibit similar morphologies to the as-grown sample.

In section 7.2, we explore the impact of the annealing process and different annealing temperatures on the luminescence properties of the samples. We show that the dielectric SiN_x cap improves the light-coupling of the laser to the NW, resulting in a higher luminescence intensity. Furthermore, the FWHM of the luminescence peak corresponding to the (In,Ga)As shell decreases with increasing annealing temperature from 40 meV to 14 meV, indicating alloy homogenization in the $In_{0.15}Ga_{0.85}As$ shell.

In section 7.3, we explore the role of the SiN_x cap in the annealing process. We show by x-ray diffraction measurements that the SiN_x shell imposes strain on the NW structure. By annealing, this strain increases due to out-diffusion of residual hydrogen from the SiN_x. This strain partly explains the shift of emission energies seen in the PL investigation.

In section 7.4, we discuss the luminescence properties of the annealed structure in more

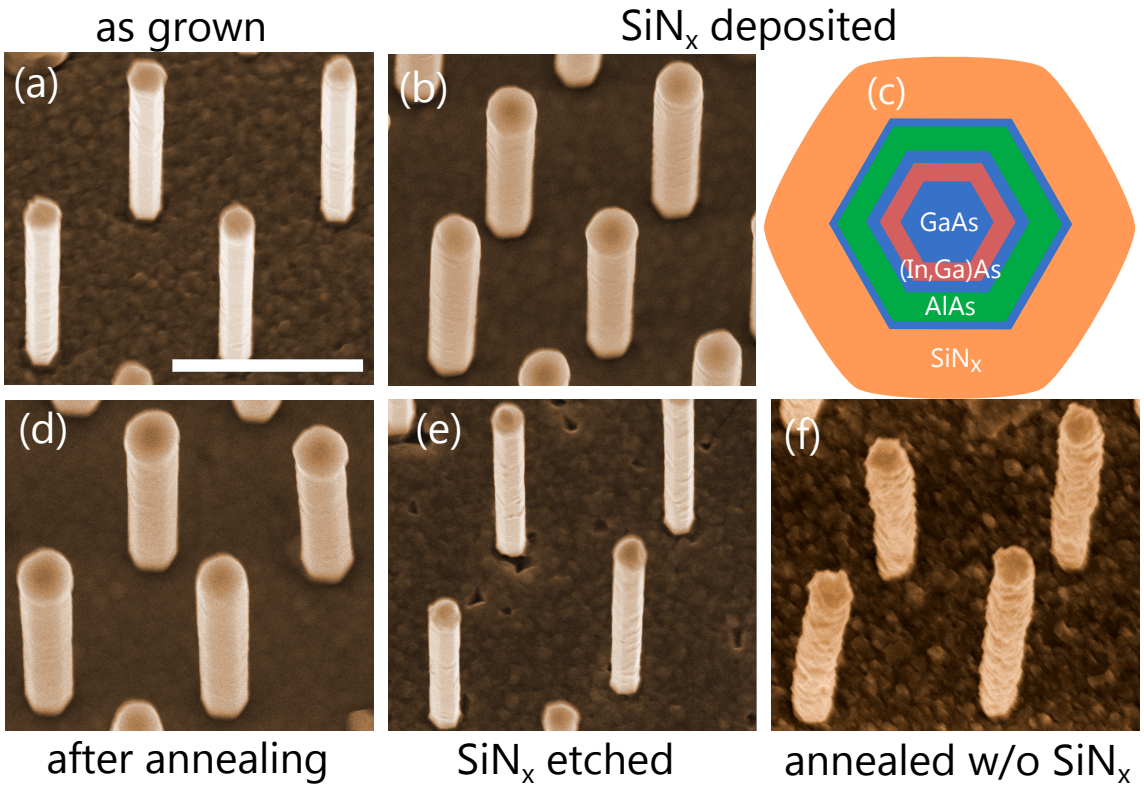

Figure 7.1: Different stages of the annealing procedure: (a) after growth, (b) after depositing SiN_x cap, (c) visualization of the cross-sectional structure of the core-shell NW heterostructure with SiN_x cap, (d) after annealing at 900 °C, and (e) after etching the SiN_x cap. (f) Micrograph of a sample annealed at 900 °C without SiN_x cap. The scale bar corresponds to 1 µm in all micrographs. All micrographs are taken under an angle of 15° from the substrate normal.

detail. We show that in PL the emission shifts to higher energies with increasing excitation power, similar to the as-grown sample. This result might indicate band filling effects. We show that localization of carriers at low temperatures is insignificant compared to what we have shown in chapter 6 for the as-grown sample. Furthermore, the thermal quenching of the PL intensity exhibits an activation energy of 40 meV which is similar to the activation energy observed for the as-grown sample indicating a specific recombination channel which cannot be reduced by thermal annealing.

7.1 Description of the annealing process

Figure 7.1(a) shows a NW core-shell sample after growth, with NWs having a length of 2.5 µm and a total diameter of 160 nm. The core-shell structure consists of a 60 nm thick core, a 10 nm $In_{0.15}Ga_{0.85}As$ shell, a 10 nm GaAs spacer shell, a 20 nm AlAs barrier shell and a 10 nm cap shell (optimum growth conditions for the $In_{0.15}Ga_{0.85}As$ shell T_{growth}=440 °C, $f_{\text{Ga}} = 6.8$ nm/min, $f_{\text{In}} = 1.3$ nm/min, $R_{5/3} = 20$, for GaAs and AlAs

shells same T_{growth} and $R_{5/3}$ using fluxes $f_{\mathrm{Ga}} = 6.8$ nm/min and $f_{\mathrm{Al}} = 3.4$ nm/min, respectively). The dimensions, in particular the thickness of the spacer shell, are chosen as a consequence of the results in chapter 6, where we showed that a 5 nm thick spacer shell is not thick enough to prevent nonradiative decay at the AlAs interface. Figure 7.1(b) shows the sample after deposition of SiN_x with a planar thickness of 100 nm. The layer of amorphous SiN_x was deposited using plasma-enhanced chemical vapour deposition (PECVD) at a deposition temperature of 345 °C by Ina Ostermay (Ferdinand-Braun-Institut Leibniz-Institut für Höchstfrequenztechnik). From SEM images we measured a thickness of the cap of 70 nm on the NW sidewalls. This thickness corresponds to 70% of the planar thickness on the substrate surface. Furthermore, the micrograph confirms the conformal growth of a continuous layer of SiN_x around the NW, which has not been reported before. We note that previously SiN_x layers have been used for surface passivation and anti-reflection coating on InP NW based solar cells after device processing.[225] Our result is comparable to what has been shown for SiO_2 deposition around NWs.[226,227] Here, we used SiN_x because it was reported to be a good material for protection of GaAs layers during high temperature annealing, as it reduces the out-diffusion of Ga more efficiently than SiO_2 layers.[218,228–230] Figure 7.1(c) shows the final structure in cross-section with the rounded edges of the SiN_x layer as seen in the micrograph.

Figure 7.1(d) shows a micrograph of the sample after annealing in an RTA oven for 30 s at 900 °C under N_2 atmosphere. The NW morphology appears to be similar to that of the sample before annealing, only a slight increase in tilting of the NWs can be seen. This result proves that the SiN_x layer is thermally stable up to such high annealing temperatures. Figure 7.1(e) shows the sample after annealing and removing the SiN_x layer. The NW morphology appears to be comparable to the as-grown sample in Figure 7.1(a). However, the NW sidefacets seem to be rougher, possibly from unetched parts of the SiN_x. The SiN_x was etched in concentrated buffered HF (BHF) solution (NH_4F : HF : H_2O, 5 : 1 : 8). The etching rate for as-deposited SiN_x is typically 35–40 nm/min. However, by measuring the thickness of the layer on the substrate before and after etching, we found an etching rate of around 4 nm/min. Previous studies have shown that residual H atoms in PECVD grown SiN_x diffuse out of the material at temperatures above 600 °C, leading to a denser material and a lower etching rate.[231,232] To assure that the 70 nm thick SiN_x cap is removed completely, the sample was etched for 45 min, without the potential risk of etching the GaAs because undoped GaAs is not etched by BHF (Etching experiments conducted by Abbes Tahraoui and Walid Anders). We note that on the substrate surface residual SiN_x might have remained as the layer thickness was larger.

Figure 7.1(f) shows a micrograph of a sample annealed at 900 °C for 30 s without a SiN_x cap. The NWs exhibit a very rough surface and are slightly bent in random directions. For this sample no luminescence could be detected. Interestingly, the NWs of this sample appear to be thicker than the as-grown sample. However, this result shows the efficacy of the SiN_x cap to protect the GaAs material during the high temperature annealing.

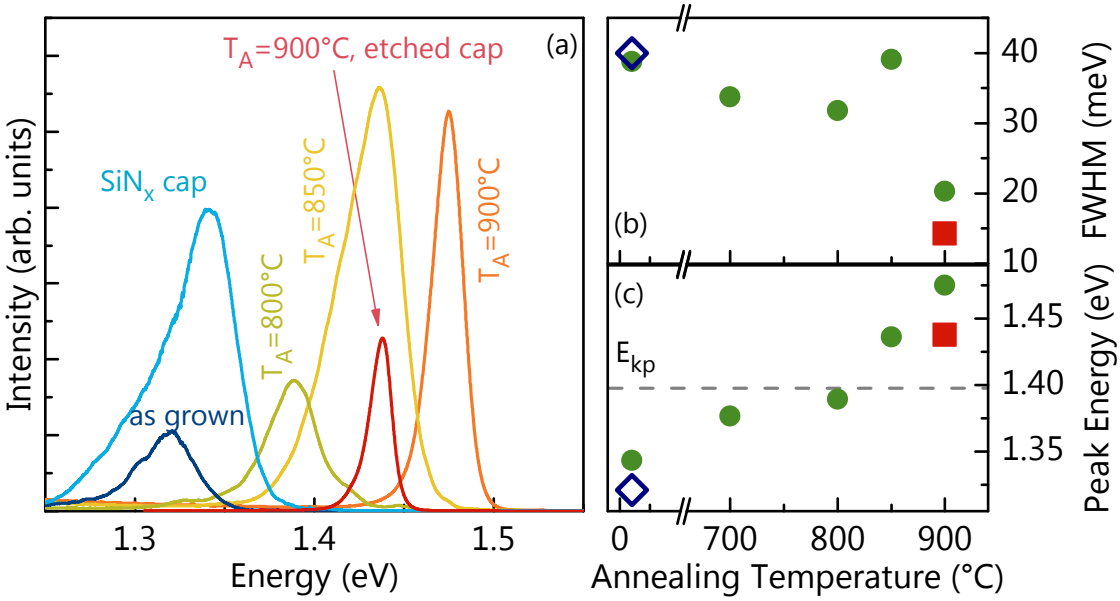

Figure 7.2: (a) PL spectra of samples of the annealing series taken at 10 K and P_{exc}=52µW: The as-grown sample (dark blue), SiN_x capped sample (bright blue), annealed samples at different annealing temperatures (green, yellow and orange lines), and the annealed sample after etching the SiN_x cap (red line). (b) Full-width-half-maximum of the spectra in (a) as a function of annealing temperature. (c) Extracted peak energies of the spectra in (a) as a function of annealing temperature. The dashed line shows the calculated energy for the nominal core-shell structure. In (b) and (c), the as-grown (blue diamond) and capped sample are shown at 20 °C and the red square represents the annealed sample after removing the SiN_x cap.

7.2 Impact of annealing process on luminescence properties

Figure 7.2(a) shows PL spectra taken at 10 K on different samples of the annealing series. The spectrum taken on the as-grown sample (dark blue curve) shows a peak centred at 1.32 eV. The sample was grown using Ga source Ga2 because Ga1 was damaged at that time. As discussed in chapter 5.3.3, this condition may lead to lower emission energies compared to samples discussed before. The spectrum taken on the sample with deposited SiN_x cap (light blue) shows a main peak centered at around 1.34 eV with an intensity which is 5 times the intensity of the uncapped sample. The increase in intensity indicates an enhanced light coupling due to the dielectric SiN_x cap. Here, the SiN_x cap has an intermediate refractive index (n_{GaAs} = 3.95,[233] n_{SiN_x} = 2.05,[234] n_{vacuum} = 1) which has been shown to decrease the screening of the electro-magnetic field of the exciting light inside the NW.[235] Thus, more electron-hole pairs are generated leading to light emission which is detected by PL.

The yellow and orange curves show the spectra of samples annealed at different temperatures. For 800 °C, the intensity decreases compared to the not-annealed sample. For higher annealing temperatures the intensity increases again. For a sample annealed at

950 °C (not shown), no luminescence could be detected, indicating a destruction of the sample structure. The red curve shows the spectrum of the sample annealed at 900 °C after removing the SiN_x cap. The linewidth is even smaller and the emission is shifted to lower energies compared to the sample with SiN_x cap.

Figure 7.2(b) shows the FWHM of the emission peaks as a function of annealing temperature as blue circles. The not-annealed samples are shown at $T_{anneal} = 20$ °C. The FWHM shows a decreasing trend with increasing temperature with the exception of 850 °C. For this temperature migration processes might get activated leading to an intermediate state with strong disorder. After removing the SiN_x cap of the sample annealed at 900 °C (red square), the FWHM further decreases to 14 meV for an ensemble of NWs. This improvement in the emission homogeneity shows the efficacy of the annealing process. However, it is still larger than the linewidth of optimized planar (In,Ga)As QWs (on (100) substrates or grown by MEE), which is typically only few meV[187,236] but smaller than for the planar (110) QWs presented in Figure 5.8.

Figure 7.2(c) shows the emission energy of the main peak as a function of annealing temperature. The bright blue diamond represents the as-grown sample and the red square represents the annealed sample after removing the SiN_x cap. In general, the emission energy increases gradually for increasing annealing temperature. Interestingly, by removing the SiN_x cap of the sample annealed at 900 °C, the peak energy decreases, indicating strain imposed by the SiN_x cap which will be discussed in detail in the next section. The increase of emission energy of the (In,Ga)As shell QW with increasing annealing temperature might have different reasons: First, the In distribution in the QW gets homogenized due to thermal activation of diffusion which removes alloy clusters.[237,238] The dashed horizontal line shows the emission energy as calculated for a structure with the same nominal parameters by $\mathbf{k} \cdot \mathbf{p}$ calculations ($E_{\mathbf{kp}} = 1.396$ eV, calculations done by Oliver Marquardt). The as-grown sample shows luminescence at a significantly lower energy compared to the theoretical value. As discussed in chapter 5, the $In_{0.15}Ga_{0.85}As$ shell shows alloy clustering beyond random alloy fluctuations leading to localization of carriers in potential minima. Additionally, this clustering effect is enhanced for samples grown using the Ga2 source as discussed in chapter 5.3.3. This strong clustering in the as-grown sample might lead to strong homogenization of the In distribution in the $In_{0.15}Ga_{0.85}As$ during annealing, possibly explaining the strong shift in emission energy. Second, the QW intermixes with the barrier material leading to diffuse interfaces. For planar (110) $In_{0.1}Ga_{0.9}As$ QWs grown in the continuous MBE mode a blue-shift of the emission of 40 meV by annealing to 900 °C was reported.[184] In our experiments, we observed a blue-shift of 115 meV for the sample annealed at 900 °C and removed cap, which is significantly larger even taking into account the higher In content. We suggest that the stronger initial clustering in the $In_{0.15}Ga_{0.85}As$ shell might be the reason for the stronger change of the distribution of the In content during annealing. However, this is the first study to address the annealing of NW structures at such high-temperatures, thus for understanding the intermixing in NW core-shell structures in detail more work

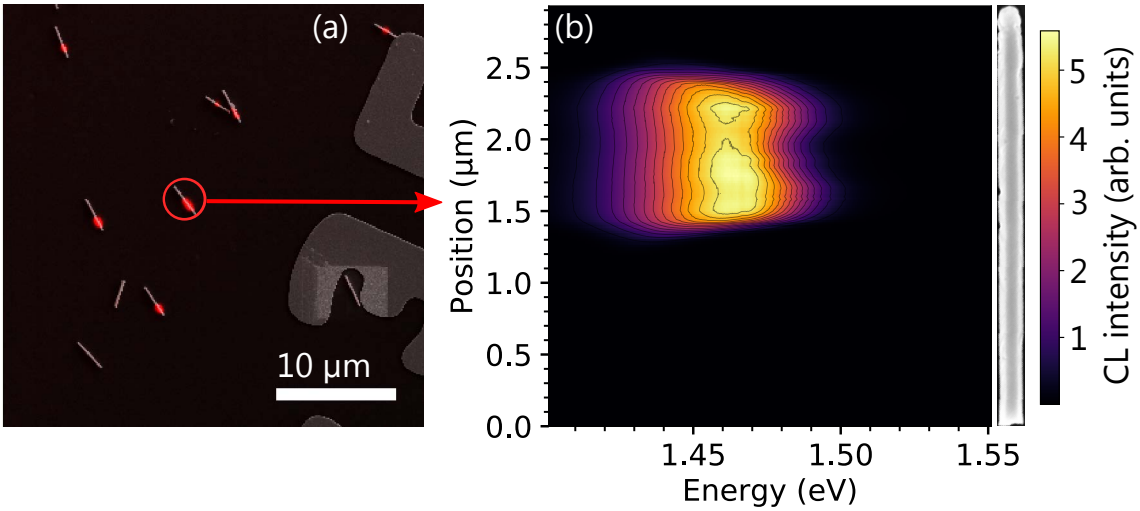

Figure 7.3: (a) Pan-chromatic image of cathodoluminescence of annealed NWs dispersed on a TEM grid. The red areas indicate high luminescence intensity. (b) CL line scan along the axis of a single annealed NW. A high resolution SEM image of the same NW is shown at the right side. All measurements done by Jonas Lähnemann.

is necessary.

Figure 7.3(a) shows a CL panchromatic measurement of dispersed NWs of the annealed sample after removing the SiN_x cap. Here, emitted light is detected over a broad spectral range and the red color indicates locations exhibiting high luminescence intensities. This information is overlayed on a SEM image of the respective sample. Most NWs show strong emission at a segment on one end of the NW. Figure 7.3(b) shows a CL linescan along the axis of a single NW with intensity in logarithmic scale. Similar to the observation in Figure 7.3(a), the luminescence is only located in a segment of the NW. Here, we find that it is in the top part of the NW, from 1.4–2.4 µm length, whereas the 500 nm long part below the tip does not show luminescence. The luminescence distribution exhibits a high intensity and is centred at a constant peak energy of E_{peak}=1.460 meV over the entire segment. This energy is higher than the peak energy detected in ensemble PL measurements, possibly due to the higher excitation intensity in CL compared to PL, as we will discuss in detail in the following part. The constant emission energy is in contrast to the results on as-grown NWs (grown using Ga1) shown in Figure 5.4(e) and (f), where fluctuations of the emission energy over the NW length were and peaks at low energy were observed. We note, that the annealed sample was grown using Ga2 where even stronger fluctuations in the as-grown sample are expected. This result underlines the efficacy of the annealing process in leading to a more homogeneous emission of the (In,Ga)As shell. Interestingly, the high resolution SEM image of the dispersed NW in Figure 7.3(c) shows a rough NW surface which was not observed in the lower magnification images in Figure 7.1(e). This roughening might be due to the annealing process but no detrimental impact on the luminescence properties is seen in this part, for example

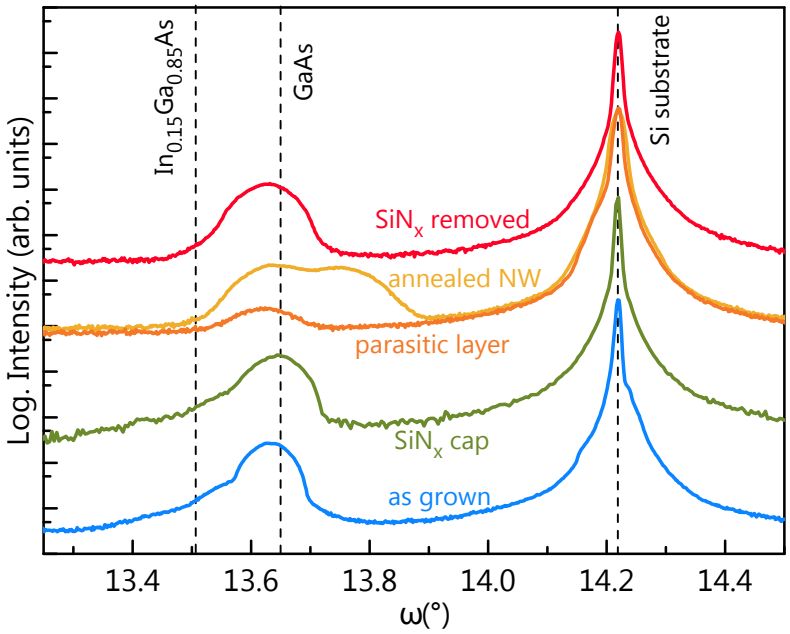

Figure 7.4: (111) X-ray diffraction $\omega/2\theta$ scans for samples at different stages of the annealing process. The vertical lines indicate the expected position of fully relaxed $In_{0.15}Ga_{0.85}As$ and GaAs, and the Si substrate, respectively.

at a height of 1.6 µm, indicating that the shell QW is not affected. Furthermore, the low emission intensity detected at the lower part of the NW in Figure 7.3(b) has also been observed for the as-grown NWs in Figure 5.4. Consequently, we suppose that the NW bottom exhibits defects that result in a strong nonradiative recombination of charge carriers. These defects cannot be removed by the annealing procedure. We speculate that the defects are related to the high density of stacking faults at the bottom of the NW observed in the TEM micrograph in Figure 5.9. Here, the surface of the GaAs with a high density of axial stacking faults and twins might exhibit microscopic roughness, possibly acting as a non-ideal substrate for the shell growth. In that context, it has been shown by scanning tunneling microscopy experiments that the surface atoms in the (110) sidefacet close to a twin plane get displaced due to different atomic configuration of the twins.[239] However, so far, studies have focused on the extension of axial defects into the shell but no results have indicated additional defect formation at the interface.[240,241]

7.3 Strain in the capped core-shell system

Figure 7.4 shows X-ray diffraction $\omega/2\theta$ scans in out of plane geometry using a slit of 1 mm in detection of samples at different stages of the annealing process. The Bragg peaks detected in this measurement correspond to the (111) lattice spacing of the respective sample, presented in Table 7.1. The blue curve shows the as-grown sample. Apart from the Si substrate peak, a broad peak is detected corresponding to a lattice spacing of

sample condition	a_{111} (Å)	$\epsilon_{(In,Ga)As}$ (%)
as grown	3.267	-0.92
SiN_x cap deposited	3.262	-1.08
annealed at 900 °C	3.238	-1.78
SiN_x cap removed	3.268	-0.88

Table 7.1: Lattice spacing in the (111) direction of the measured samples in Figure 7.4 and the corresponding axial strain value for the (In,Ga)As shell.

$a_{NW,\,as\,grown} = 3.267$ Å. Additionaly, a shoulder at a smaller angle is detected. We can assume that the first peak corresponds to the core-shell NWs and the shoulder results from the polycrystalline parasitic layer on the oxide-covered Si substrate between the NWs and the wurtzite structure in the NWs.[20] In the core-shell system, the strain is partitioned between the core and the shells.[68] This behaviour is in contrast to the case of planar layers, where the substrate is assumed to be infinitely thick and lattice-mismatched layers grown on the substrate contain the entire strain.

In general the elastic energy in a system given by

$$U = \frac{1}{2}\int C_{ijkl}\epsilon_{ij}\epsilon_{kl}dV \tag{7.1}$$

where C_{ijkl} are the elastic stiffness tensor elements and ϵ_{ij} the elastic strain tensor components. For an infinitely long NW we can assume that the strain distribution is constant along the length,

$$U = \frac{1}{2}L_{NW}\int C_{ijkl}\epsilon_{ij}\epsilon_{kl}dA \tag{7.2}$$

where L_{NW} is the NW length and the integration is executed over the cross-sectional area of the NW. The elastic stiffness tensor is typically defined with respect to the crystallographic system. In the case of a cubic crystal, the base is formed by $\langle 100\rangle$, $\langle 010\rangle$, and $\langle 001\rangle$. In order to use the NW specific directions $\langle 1\bar{1}0\rangle$, $\langle 1\bar{1}2\rangle$, and $\langle \bar{1}\bar{1}\bar{1}\rangle$ the base needs to be transformed via a rotation matrix $\mathcal{R}$. Following this procedure[135] the strain energy with respect to the axial direction is

$$U = \frac{1}{3}L_{NW}\int (c_{11}+2c_{12}+4c_{44})\epsilon_{zz}^2 dA = L_{NW}E\int \epsilon_{zz}^2 dA \tag{7.3}$$

where c_{11}, c_{12}, and c_{44} are the unique elastic constants in the cubic system, ϵ_{zz} is the strain in the axial $\langle \bar{1}\bar{1}\bar{1}\rangle$ direction and E sums up the elastic constants in a single constant for simplicity.

The axial strain in the GaAs core and outer shells and in the (In,Ga)As shell are

$$\epsilon_{GaAs} = \frac{a_{shared} - a_{GaAs}}{a_{GaAs}} \tag{7.4}$$

$$\epsilon_{\text{(In,Ga)As}} = \frac{a_{\text{shared}} - a_{\text{(In,Ga)As}}}{a_{\text{(In,Ga)As}}} \tag{7.5}$$

with the shared axial lattice constant a_{shared}, and the lattice constant of the relaxed GaAs and (In,Ga)As, a_{GaAs} and $a_{\text{(In,Ga)As}}$, respectively. By minimization of the total energy from Equation 7.3 with respect to a_{shared} we obtain

$$a_{\text{shared}} = \frac{a_{\text{(In,Ga)As}} a_{\text{GaAs}} \left(E_{\text{GaAs}} a_{\text{(In,Ga)As}} A_{\text{GaAs}} + E_{\text{(In,Ga)As}} a_{\text{GaAs}} A_{\text{(In,Ga)As}} \right)}{E_{\text{(In,Ga)As}} A_{\text{(In,Ga)As}} a_{\text{GaAs}}^2 + E_{\text{GaAs}} A_{\text{GaAs}} a_{\text{(In,Ga)As}}^2} \tag{7.6}$$

where E_{GaAs} and $E_{\text{(In,Ga)As}}$ are calculated using the elastic constants for core and shell in Equation 7.3, respectively, and A_{GaAs} and $A_{\text{(In,Ga)As}}$ are the cross-sectional areas of GaAs core and outer shell and the (In,Ga)As shell, respectively. For the case of small In contents in the (In,Ga)As shell we assume that $E_{\text{GaAs}} = E_{\text{(In,Ga)As}}$. Using Equation 7.6, we calculate the shared lattice parameter for the as grown NW and obtain $a_{\text{shared}} = 3.267$ Å. Here, we used a cylindrical model of the NW to calculate the areas from the respective radii of core and shells. Also, we assumed the same lattice constant for GaAs and AlAs. This theoretical value is in good agreement with the experimental value of $a_{\text{NW, as grown}} = 3.267$ Å, confirming our simple model.

The green curve in Figure 7.4 shows a measurement on the sample with deposited SiN_x cap. The main peak beside the substrate peak is broadened and shifted to slightly higher angles, compared to the as-grown sample. The corresponding lattice parameter of the NW is $a_{\text{NW, cap}} = 3.262$ Å. This value is smaller than for the sample without SiN_x cap, indicating that the NW is compressively strained by $\epsilon_{\text{NW, cap}} = -0.16\%$ with respect to the as-grown state. The deposited SiN_x is typically slightly tensily strained due to the chosen deposition parameters,[242] thus resulting in the strain of the NW. This strain also explains the shift in emission energy by deposition of the SiN_x shell seen in Figure 7.2(c).

The yellow curve in Figure 7.4 shows the measurement on the sample after annealing at 900 °C. Two broad peaks are detected at angles corresponding to lattice spacing of $a_{\text{annealed, 1}} = 3.266$ Å and $a_{\text{annealed, 2}} = 3.238$ Å. The orange curve shows a measurement of the annealed sample at a position on the substrate that is outside of the NW array. Here, we can assume that the signal only corresponds to the parasitic layer on the substrate surface. In addition to the substrate peak only one peak exists. The peak position is in good agreement with the first peak of the measurement inside the NW array. Therefore, we attribute the first peak to the parasitic layer of relaxed GaAs, $In_{0.15}Ga_{0.85}As$, and AlAs. Typically we see separate peaks of the different polycrystalline layers. Thus, the existence of a single peak from the parasitic layers indicates that also these layers intermix strongly during the annealing forming a mixed alloy layer. The lower intensity of the peak measured out of the NW array (orange curve) compared to the peak measured inside the NW array (yellow curve) indicates that the polycrystalline parasitic layer has a preferential crystal orientation inside the NW arrays. Possibly the parasitic layer adopts

the crystalline orientation from the NWs. The second peak is attributed to the NW structure, yielding $\epsilon_{\text{(In,Ga)As, annealed}} = -1.78\%$ in the $In_{0.15}Ga_{0.85}As$ shell, which differs from the as-grown sample by $\Delta\epsilon_{\text{(In,Ga)As, annealed}} = -0.87\%$ from the values shown in Table 7.1. As discussed before, the SiN_x material deposited by PECVD contains residual hydrogen, with amounts depending on deposition conditions. After annealing the SiN_x cap the hydrogen content is lower and the lattice shrinks. This compressive stress is imposed onto the NW structure, leading to compressive strain in the NW and another core-shell structure of NW and cap is formed in which the strain is also partitioned.

The red curve in Figure 7.4 shows the measurement on the annealed sample after removing the SiN_x cap. Besides the substrate peak, only one broad peak is detected corresponding to $a_{\text{SiN removed}} = 3.268$ Å. This value is very similar to the value of the as-grown sample, indicating that the strain induced by the SiN_x cap is relieved after the SiN_x is removed. Furthermore, it shows that the re-distribution of the alloy during annealing does not change the axial lattice constant. The large peak width might indicate that either the axial strain is more inhomogeneous after annealing or the NWs exhibit more tilting, which results in a broader peak in this XRD measurement. A stronger degree of tilting is also suggested by the SEM images of that sample (cp. Figure 7.1).

The strain in the NW also affects the bandgap of the material and thereby shifts the peak energy in luminescence. This shift is detected for the annealed sample in Figure 7.2, where the emission energy decreases by 37 meV after removing the SiN_x cap. This effect might also partially explain the strong blue-shift with annealing temperature. Furthermore, the strain affects the FWHM of the luminescence peak, possibly indicating inhomogeneous strain profiles in the NW, leading to broader emission. For uniaxially strained GaAs NWs the reported changes in emission energy with strain are similar to our results.[243] However, for a precise correlation of the impact of strain on the electronic energy more complex band-stucture calculations are necessary,[244] the complete strain profile of the core-shell NW needs to be taken into account,[135] and the temperature dependence of the strain due to the difference in lattice expansion needs to be taken into account, which is beyond the scope of this study.

7.4 Luminescence properties of the annealed core-shell sample

Figure 7.5(a) shows PL spectra taken at 10 K for varying excitation power on a NW ensemble of the annealed sample (T_{Anneal} =900 °C) after removing the SiN_x cap. For the lowest excitation power, the spectrum is centred at 1.41 eV. For increasing excitation power, the peak shifts to higher energies and shows a smoother shape. No sharp peaks are detected that have been observed for the as-grown sample in Figure 6.1. These sharp emission features were assumed to originate from excitons localized at potential fluctuations in the $In_{0.15}Ga_{0.85}As$ shell. The absence of such features indicates that the annealed sample exhibits less alloy clustering. Figure 7.5(b) shows the peak energy as a

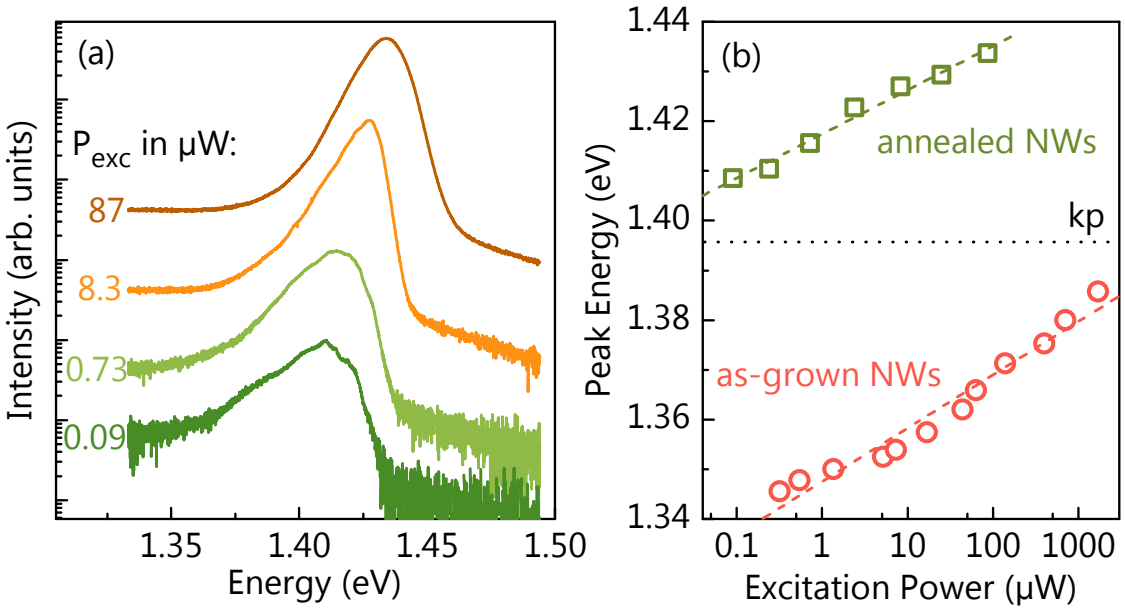

Figure 7.5: (a) PL spectra taken at 10 K on an ensemble of NWs of the annealed sample (T_{Anneal} = 900 °C) after removing the SiN_x cap. The excitation power is given next to the respective curve. (b) Peak energy from Gaussian fits of the spectra taken on the annealed sample (green squares) and on the as-grown sample (red circles, cf. Figure 6.1) as a function of excitation power. The dotted line indicates the theoretical $In_{0.15}Ga_{0.85}As$ transition energy from $\mathbf{k}\cdot\mathbf{p}$ calculations. The dashed lines are fits of Equation 7.7.

function of excitation power for the as-grown NW sample (red circles, cf. Figure 6.1) and the annealed NW sample (green squares). For both samples, the peak energy increases for increasing excitation power. This power-dependence of the peak energy makes the comparison to the theoretical value from $\mathbf{k}\cdot\mathbf{p}$ calculations difficult, which is shown as the dotted line (calculation by Oliver Marquardt). The dashed lines are fits of the equation

$$E_{\text{peak}} = E_1 + b\log(P_{\text{exc.}}/1\mu\text{W}) \tag{7.7}$$

to the experimental data, where E_1 is the energy at $P_{\text{exc.}} = 1$ µW and b is a fit parameter corresponding to the increase per decade of excitation power. The corresponding values of E_1 and b obtained by the fits are given in Table 7.2.

	E_1(eV)	b(meV/dec)
as-grown NWs	1.3475 ± 0.0012	10.7 ± 0.5
annealed NWs	1.4174 ± 0.0005	8.9 ± 0.5

Table 7.2: Values obtained by fitting Equation 7.7 to the experimental data in Figure 7.5.

The different values for E_1 reflect again the blue-shift of emission due to the annealing

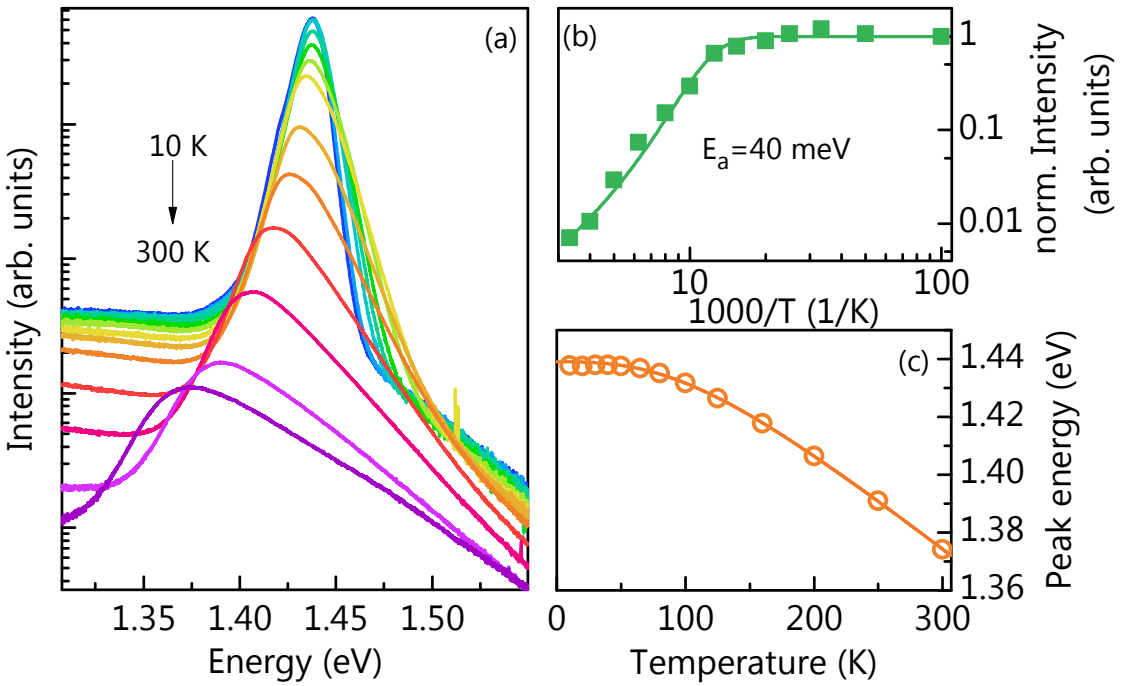

Figure 7.6: (a) PL spectra taken at $P_{exc} = 87$ µW on a NW ensemble of the annealed sample. The temperature was varied between 10 K and 300 K as indicated in the graph. (b) Normalized integrated intensity of the peaks in (a) as a function of temperature. The line is a fit of Equation 6.1 to the experimental data, yielding an activation energy of 40 meV. (c) Central energy of the emission peak in (a) as a function of temperature. The line is a fit of Equation 7.8 from the Pässler model to the experimental data.

process. On the other hand, also the value for b differs slightly between the two values. Here, the annealed sample shows a smaller value, meaning a smaller increase of emission energy with increasing excitation power. This increase indicates most probably band-filling effects that happen when more carriers in a band exist than available states at $\mathbf{k} = 0$. Then, states at higher energy are filled leading to a higher emission energy when the carriers finally recombine. This effect is particularly strong for semiconductors with low effective mass of electrons and holes, where the density of states per unit energy is small. Therefore, similar effects have been shown particularly for Arsenides and Antimonides.[245,246]

Figure 7.6(a) shows PL spectra taken on the annealed sample for temperatures from 10 K to 300 K with $P_{exc} = 87$ µW. The spectra at all temperatures show only a single peak with increasing width for increasing temperature. Also, a pronounced tail at high energies is detected. This tail might be related to emission from hot carriers[215]. Figure 7.6(b) shows the integrated intensity as a function of reciprocal temperature. It is roughly constant below 100 K and decreases rapidly for higher temperatures, yielding a room-temperature intensity of 1% of the low temperature value. This value is comparable to the as-grown sample with GaAs/AlAs shell (cf. Figure 6.2). To compare the quenching

	α (meV/K)	Θ (K)	p	$E(0\ K)$ (eV)
This study	0.36 ± 0.11	256 ± 17	2.7 ± 0.2	1.4390 ± 0.0004
GaAs bulk [247]	0.473	225.6	2.513	
$In_{0.1}Ga_{0.9}As$ QW [249]	0.415	219.1	2.36	
$In_{0.53}Ga_{0.47}As$ MQW [250]	0.320 ± 0.003	199 ± 4	3.1 ± 0.1	

Table 7.3: Values obtained by fitting Equation 7.8 from the Pässler model to the experimental data in Figure 7.6 compared to values reported in previous studies.

in more detail we fitted Equation 6.1 to the experimental data. Here, one activation channel was sufficient, yielding an activation energy $E_a = 40 \pm 3$ meV, which agrees well with $E_2 = 37$ meV, discussed in chapter 6. These results show, that the localization of excitons at low temperatures is not significant in this sample and the thermal quenching of the PL intensity is only determined by a single recombination channel with the same activation energy as in the as-grown state, which we attributed to a recombination center specific to $In_{0.15}Ga_{0.85}As$ grown under the specific growth conditions. However, the precise nature of this recombination channel is still unclear.

Figure 7.6(c) shows the peak energy obtained from Gaussian fits to the spectra as a function of temperature. The band gap energy decreases due to enhanced electron-phonon interaction. This phenomenon is described in good approximation by the model of Pässler [247,248]. Its central equation for the band gap energy as a function of temperature is

$$E_g(T) = E(0) - \frac{\alpha\Theta}{2}\left[\sqrt[p]{1+\left(\frac{2T}{\Theta}\right)^p} - 1\right] \tag{7.8}$$

where $E(0)$ is the band gap at 0 K, α a material specific parameter, p is an empirical parameter related to the electron-phonon spectral function, and Θ is a characteristic temperature representing the effective phonon energy in the system. As the Pässler model does not take into account localization effects at low temperatures we fit Equation 7.8 to the experimental data for temperatures from 50 K to 300 K, where localization effects should be negligible. We obtain the curve (extended to the entire temperature range) shown in Figure 7.6(c) with the fit parameters given in the first row of Table 7.3.

The band gap energy at 10 K taken from the fit curve is $E(10\ K) = 1.4390$ eV ± 0.4 meV, yielding a difference to the experimental value of $\Delta E = 1.4 \pm 0.4$ meV. This quantity is typically interpreted as the localization energy in disordered semiconductors. [251] The obtained value shows that the localization depth is small compared to the value of 6 meV obtained by the analysis in chapter 6, proving the higher homogeneity of the annealed sample. Furthermore, in Table 7.3 all obtained fit factors are compared to literature values for bulk GaAs [247], a (100) $In_{0.1}Ga_{0.9}As$ QW, [249] and a (100) $In_{0.53}Ga_{0.47}As$ MQW [250]. These factors are expected to be specific for a certain material. From the literature values

it seems that α decreases gradually with increasing In content in the material, agreeing with our value for 15% In. Also the value for p is similar to the literature values. However, the obtained value for Θ is significantly larger than the literature values, indicating an increased phonon energy. Also here, more work needs to be done to understand these differences in detail.

7.5 Conclusion

We have presented for the first time a process that enables the ex-situ annealing of NWs at temperatures of up to 900 °C. A SiN_x cap is used to protect the NW material from decomposition during the RTA treatment. After annealing at 900 °C and removing the SiN_x cap by wet etching, the NW morphology shows only small changes compared to the as-grown state. In contrast, the luminescence signal is shifted to higher energies and the FWHM decreases from 40 meV to 14 meV, indicating a strong homogenization of the In distribution in the (In,Ga)As shell during the annealing. Furthermore, we showed that the SiN_x cap improves light-coupling to the NW. Due to the shrinking of the SiN_x cap, compressive strain is imposed onto the NW, which is relieved again after removing the SiN_x cap.

In a detailed investigation of the annealed sample we showed that fewer indications for localization of carriers at low temperatures exist compared to the as-grown samples: No sharp lines are detected in the low-temperature PL spectra, no thermal quenching related to shallow localizations is detected, and the localization energy obtained from a fit to the peak energy variation is only 1.4 meV. Therefore, we suppose that the annealing process effectively homogenizes the In distribution in the (In,Ga)As material, removing the clusters discussed in chapter 6. However, the detailed structure of the annealed sample is unknown and further experiments by APT or TEM are required. Such an understanding, however, might give valuable insight into the migration of atoms inside radial structures such as NWs. Furthermore, we showed that the annealed samples show an increase in emission energy with increasing excitation energy that is similar to the as-grown samples. Our results suggest that the effect is related to band filling effects observed in semiconductors with low effective electron mass. Finally, we showed that the thermal quenching of the PL intensity of the annealed sample shows the same activation energy as the as-grown sample, indicating an inherent defect activation. These defects might be native defects in the $In_{0.15}Ga_{0.85}As$ shell that may form at the low growth temperature and high V/III ratio used for shell growth and remain in the $In_{0.15}Ga_{0.85}As$ shell during annealing.

8 Conclusions and outlook

In this thesis, the controlled growth of ordered arrays of GaAs NWs in combination with $In_{0.15}Ga_{0.85}As$ shell QWs was investigated with a focus on their luminescence properties. In this chapter, the main conclusions are briefly summarized and open questions are discussed that might be answered by future studies. Furthermore, as an outlook, two concrete projects are briefly described which are enabled by the results presented in this work.

8.1 Conclusions

In the first two chapters we focused on the realization of regular arrays of GaAs NWs that are suitable for the growth of core-shell structures as the basis for complex device structures. Here, we used Si substrates with oxide masks patterned by EBL, achieving hole sizes of about 40 nm that are small enough to avoid unintended leakage currents from the shell to the substrate in future core-shell devices. Establishing the growth of NW arrays with high vertical yield (i.e. high ratio of vertically oriented NWs to holes) was a challenging goal at the beginning of this work as it sensitively depends on both, the processing and growth conditions. Here, we found that the surface preparation is crucial. Boiling the wafer in ultrapure water for 10 min leads to a dramatic increase of the vertical yield of GaAs NWs, indicating that the microscopic roughness of the Si substrate plays an important role during the initial nucleation of the NW. This result might help to understand the nucleation of NWs under the liquid droplet and lead to more reproducible growth results across different research groups.

On this basis, we developed a new two-step growth approach, which enables the nucleation of GaAs NWs at low V/III ratio, the required condition for high vertical yield, and the elongation at higher V/III ratios. With this growth approach we have realized untapered NWs with both, a diameter as thin as 45 nm and a length of 2.5 µm at high vertical yield, which had not been shown before for SAG in the Ga-assisted mode by MBE. This result enables the realization of core-shell structures with homogeneous strain profiles and an advantageous strain partitioning. We showed that the diameter evolution of GaAs NWs during growth not only depends on the changing size of the Ga droplet, but also on the direct VS growth on the NW sidewall. In this context, we have derived a model that explains the radial VS growth consistently with the understanding of the axial NW growth based on diffusion processes on the NW sidewall. The combined model now enables the description of the temporal evolution of the entire shape of GaAs NWs

and its prediction over a large parameter space. This which will be necessary to realize core-shell structures with precise length and diameter for complex device structures. As the model is only based on fundamental physical principles, we expect that these results are not restricted to the growth of GaAs NWs by MBE but should also apply to other materials and growth techniques.

Based on this understanding of the growth processes, we decoded the role of the surface diffusion length of dopant atoms for the doping of VLS grown NWs. We argued that the surface diffusion length of dopant atoms impinging on the NW sidewall determines the incorporation path into the NW. Using our comprehensive model we showed that in the case of negligible surface diffusion of dopants, most dopants will incorporate into the VS grown part and form an almost ideal delta-doped interface layer to the VLS grown part. Assuming that dopant profiles of such doped GaAs NWs became available, a comparison with our predictions will enable insight into dopant surface diffusion processes that are not accessible so far. Furthermore, it might also help to explain the dependence of obtained dopant profiles on the growth conditions used in different studies and lead to optimized doping schemes for the realization of devices.

In the following chapters of this work, we used arrays of GaAs NWs as optimum templates for the investigation of the growth and luminescence properties of $In_{0.15}Ga_{0.85}As$ shell QWs. These shells can be grown conformally around GaAs NWs at relatively low substrate temperatures and high V/III flux ratios. Here, the precise separation between the NWs, achieved by SAG, leads to very symmetric cross-sectional structures. The necessary growth conditions for conformal shell growth also lead to good luminescence properties as the NW sidefacets require similar growth conditions due to their non-polar $\{1\bar{1}0\}$ surfaces. However, the growth of NW shells in MBE is inherently different compared to the growth of planar layers. The three-dimensional structure of the NW, the directionality of the material fluxes in MBE, and the substrate rotation lead to an inherent flux sequence on the NW sidewalls. Depending on the relative location of the material cells, different flux sequences arise, leading to dramatically different material properties. Only for shells grown with cell combinations where the group III and As fluxes are deposited separately, high luminescence intensities could be achieved. The corresponding flux sequence resembles the flux sequences used in migration enhanced epitaxy (MEE), indicating that similarly beneficial effects exist also in the growth of NW shells. However, the impact of the different flux sequences is much stronger for NW shells compared to planar growth which we ascribe to the impact of the $\{11\bar{2}\}$ edges of the NW where defects might form under certain conditions. The impact of such inherent flux sequences should also apply for shell growth of different materials, but the implications might be different. One can imagine that not only the surface diffusion is affected but also the desorption of atoms and transient surface energies during the sequence. However, we emphasize that the flux sequence is inherent to the growth system and its optimization is limited. Potential improvements might be the design of controlled shutter sequences for the shell growth and the use of dual cells for deposition of alloy constituents like In and

Ga from the exact same direction.

Finally, we focused on two luminescence features of the core-shell samples. First, at elevated temperatures, the luminescence intensity is quenched dramatically. We demonstrated that thermionic emission of charge carriers from the shell QW to the outer GaAs shell takes place, leading to rapid nonradiative recombination at the NW surface. This channel for nonradiative recombination can be suppressed by adding an AlAs barrier shell. Using a model based on our understanding of the carrier localization we could show that the interface of the shell QW to the outer shells crucially affects the nonradiative recombination at low temperatures. As the growth temperature needed for the growth of homogeneous shells is rather low for growth of AlAs, its interface to the QW exhibits defects. The introduction of a GaAs spacer shell between the shell QW and the AlAs barrier shell effectively reduces this effect. Based on the understanding of the channels for nonradiative recombination at different temperatures we could design a structure with a GaAs spacer shell of sufficient thickness that offers high luminescence intensities both at low temperatures and at room temperature.

Second, even after optimizing the growth parameters, the luminescence of the $In_{0.15}Ga_{0.85}As$ shell QWs still exhibits broad peaks due to alloy clustering inherent to the growth processes. These clusters also lead to localization of charge carriers at low temperatures. The nature of these clusters is unclear and further investigation by TEM or APT might help to locate them similar to what has been done for clusters in (Al,Ga)As shells. For the homogenization of the alloy, we developed a process that enables for the first time the ex-situ annealing of III-V NWs at temperatures up to 900 °C. Here, a SiN_x cap layer deposited around the NW core-shell structure can succesfully protect the NW structure from decomposition. Using this process, the FWHM of the emission peak corresponding to the shell QW decreased from above 40 meV to 14 meV. In this process, the $In_{0.15}Ga_{0.85}As$ alloy is strongly homogenized and the alloy clusters are removed which results in a blue-shift of the emission energy. Experimental alloy profiles obtained by APT could elucidate the migration of atoms in the radial NW structure. The annealing process now enables the realization of core-shell structures of highest qualities and is suitable for nanostructures consisting of many other materials.

Nonetheless, two open questions remain that affect the luminescence properties of such core-shell NWs. First, the annealed sample exhibited a similar thermal quenching behaviour of the luminescence intensity compared to the as-grown samples, yielding an activation energy of 40 meV. We attribute this defect tentatively to a defect characteristic for $In_{0.15}Ga_{0.85}As$ grown under the specific growth conditions (low temperature, high V/III ratio). However, the nature of this recombination channel is unknown and more work is necessary to explore ways to remove the origin of this dominating channel for nonradiative recombination. Second, the lower parts of the annealed NWs show very weak emission, similar to the as-grown samples. The origin of this effect is not clear yet but we suspect that it correlates with the high density of stacking faults and twin planes at the bottom of the NWs. These planar defects may not be detrimental by themselves

but may lead to the formation of defects when growing shells vertical to them. A detailed investigation of this correlation and the microscopic nature of the interface in the defective areas might help to improve the growth of shells on sidewall surfaces normal to planar defects.

8.2 Outlook

This thesis presents the necessary understanding and experimental steps to grow specifically designed arrays of GaAs/(In,Ga)As core-shell quantum well structures with optimized structure for high luminescence intensity and narrow emission linewidths. Based on the growth on the versatile oxide mask these results enabled two concrete projects that are already in progress.

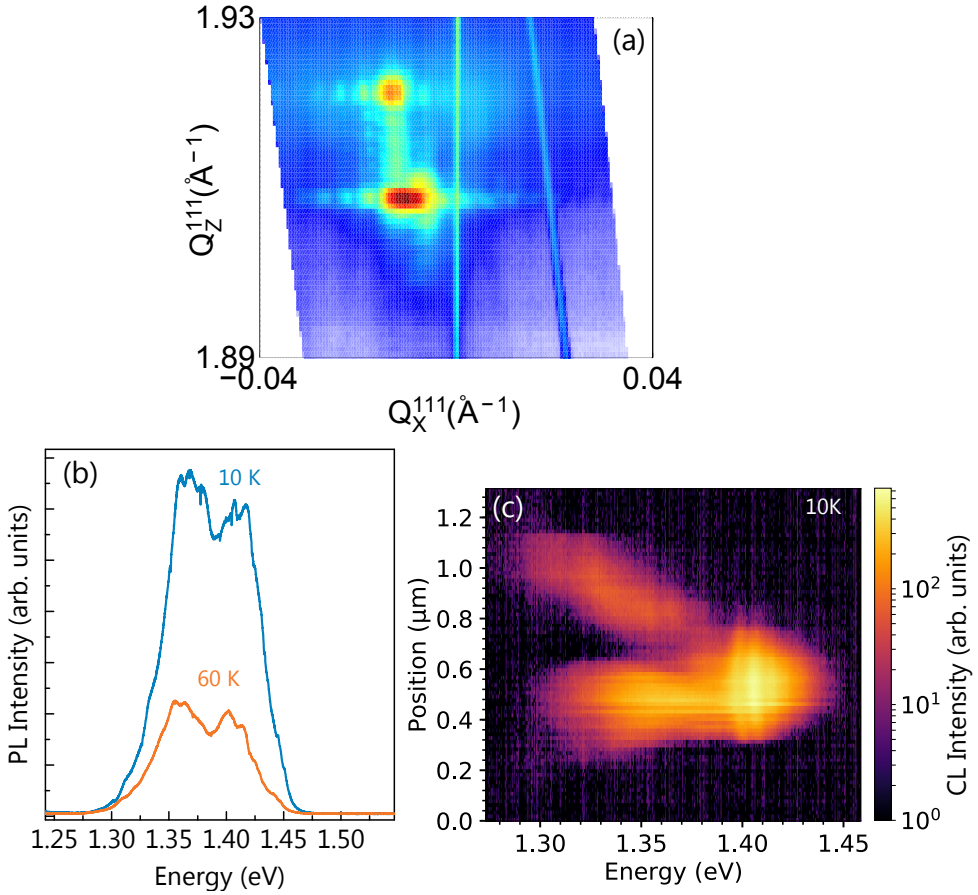

Figure 8.1: Correlated measurements performed on one and the same single free-standing NW: (a) reciprocal space map at the (111) Bragg peak measured by nanofocus synchrotron X-ray diffraction. Measurement performed by Ali Al Hassan (Universität Siegen). (b) Micro-PL spectra taken at different temperatures. (c) CL linescan taken at 10 K. Measurement performed by Jonas Lähnemann.

First, the discussed structures may be the basis for a more detailed analysis of the inter-

action of radial QWs with external fields and explore the correlation of structural properties, i.e. the strain distribution in the NW, with the electronic properties, i.e. mainly the emission energy, exploring the existence of shear strains[135] inducing piezoelectric polarization fields and the effect of spontaneous polarization in wurtzite sections.[143,252,253] Figure 8.1 shows correlated measurements recently acquired by different techniques on one and the same free-standing NW. The versatile mask that was used for the samples discussed in this thesis contains a line of single holes for NW growth, with a separation of 10 µm between them. These fields enable the efficient measurement of single NWs on the substrate by various complementary methods (The sample has a core-shell structure with 10 nm $In_{0.15}Ga_{0.85}As$ shell and 30 nm outer GaAs shell): Figure 8.1(a) shows a reciprocal space map (RSM) at the (111) Bragg peak measured by nanofocus synchrotron X-ray diffraction. Reflection from zincblende and wurtzite phase are observed. The synchrotron beam has a size of 1.8 µm x 0.6 µm assuring that only the desired NW is measured. As the NWs were measured standing on the substrate, further measurements at the $(2\bar{2}0)$ reflection at different heights of the NW have also been measured in the in-plane direction. However, the analysis is not finished and here we want to limit the discussion to the possibilities these correlative measurements may present. Figure 8.1(b) shows PL spectra taken at two different temperatures of the same NW. By using a high-magnification microscope objective we assure that only the NW of interest is measured. Figure 8.1(c) shows a CL line-scan taken at low temperature of the same NW. As the NW was measured standing on the substrate the CL measurement needs to be performed under a tilting angle, leading to an apparently compressed NW length. These results now give complementary information about the crystal structure and the electronic structure of single NWs and from the $(2\bar{2}0)$ measurements further information about the structure of the shells may be obtained.

Second, the growth on Si substrates covered with a freely designable oxide mask now enables the realization of more complex device structures based on specific NW arrays. Figure 8.2(a) shows the schematic diagram of a device structure that was proposed recently by researchers at Paul-Drude-Institut.[21] An array of NWs is positioned on substrates that contain Si waveguides. This combination acts as a grating coupler to couple light between the waveguide and the NW but also its sorrounding in an efficient way and lead the way to the realization of lasing structures. Using core-shell NWs that generate light or act as photodetectors, a complete optical interconnect system on Si could be realized based on this structure. Figure 8.2(b) shows the calculated outcoupling efficiency as a function of the separation between the NWs (period) and the height of the NWs. The calculations show that the light-coupling depends sensitively on the NW height. For an efficient device, NWs with precisely defined length and diameter (not shown here) need to be synthesized. Our understanding of the diameter evolution of GaAs NWs enables the determination of growth parameters that lead to untapered NWs of specific length. Thereby, it offers the precision that is necessary for the realization of such complex device structures in the future. Furthermore, our understanding of the doping pathways may

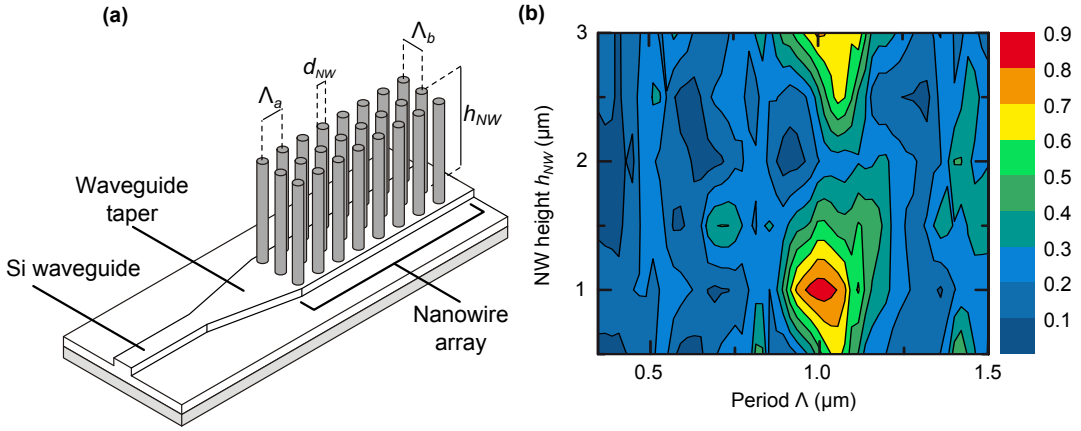

Figure 8.2: (a) Schematic diagram of a proposed device structure that combines NW arrays with silicon waveguides. (b) Calculated light-outcoupling efficiency of the NW array that is fed by incoming light from the waveguide as a function of period λ and NW height h_{NW}. Figures used with permission from Giuntoni *et al.* [21]

lead to optimized doping schemes for the realization of the electrical pumping of such devices.

Bibliography

[1] Y. B. Bolkhovityanov and O. P. Pchelyakov, GaAs epitaxy on Si substrates: modern status of research and engineering, *Physics-Uspekhi* **51**, 437–456 (2008).

[2] E. P. A. M. Bakkers, M. T. Borgström, and M. A. Verheijen, Epitaxial Growth of III-V Nanowires on Group IV Substrates, *MRS Bull.* **32**, 117–122 (2007).

[3] D. Spirkoska, J. Arbiol, A. Gustafsson, S. Conesa-Boj, F. Glas, I. Zardo, M. Heigoldt, M. H. Gass, A. L. Bleloch, S. Estrade, M. Kaniber, J. Rossler, F. Peiro, J. R. Morante, G. Abstreiter, L. Samuelson, and A. Fontcuberta i Morral, Structural and optical properties of high quality zinc-blende/wurtzite GaAs nanowire heterostructures, *Phys. Rev. B* **80**, 245325 (2009).

[4] U. Jahn, J. Lähnemann, C. Pfüller, O. Brandt, S. Breuer, B. Jenichen, M. Ramsteiner, L. Geelhaar, and H. Riechert, Luminescence of GaAs nanowires consisting of wurtzite and zinc-blende segments, *Phys. Rev. B* **85**, 045323 (2012).

[5] P. Corfdir, R. B. Lewis, O. Marquardt, H. Küpers, J. Grandal, E. Dimakis, A. Trampert, L. Geelhaar, O. Brandt, and R. T. Phillips, Exciton recombination at crystal-phase quantum rings in GaAs/$In_xGa_{1-x}As$ core/multishell nanowires, *Appl. Phys. Lett.* **109**, 082107 (2016).

[6] M. Nilsson, L. Namazi, S. Lehmann, M. Leijnse, K. A. Dick, and C. Thelander, Single-electron transport in InAs nanowire quantum dots formed by crystal phase engineering, *Phys. Rev. B* **93**, 195422 (2016).

[7] P. Krogstrup, H. I. Jørgensen, M. Heiss, O. Demichel, J. V. Holm, M. Aagesen, J. Nygard, and A. Fontcuberta i Morral, Single-nanowire solar cells beyond the Shockley-Queisser limit, *Nat. Photon.* **7**, 306–310 (2013).

[8] K. Tomioka, J. Motohisa, S. Hara, K. Hiruma, and T. Fukui, GaAs/AlGaAs core multishell nanowire-based light-emitting diodes on Si, *Nano Lett.* **10**, 1639–1644 (2010).

[9] B. Hua, J. Motohisa, Y. Kobayashi, S. Hara, and T. Fukui, Single GaAs/GaAsP Coaxial Core-Shell Nanowire Lasers, *Nano Lett.* **9**, 112–116 (2009).

[10] R. R. LaPierre, A. C. E. Chia, S. J. Gibson, C. M. Haapamaki, J. P. Boulanger, R. Yee, P. Kuyanov, J. Zhang, N. Tajik, N. Jewell, and K. M. a. Rahman, III-V nanowire

photovoltaics: Review of design for high efficiency, *Phys. Status Solidi RRL* **7**, 815–830 (2013).

[11] M. De Luca, G. Lavenuta, A. Polimeni, S. Rubini, V. Grillo, F. Mura, A. Miriametro, M. Capizzi, and F. Martelli, Excitonic recombination and absorption in $In_xGa_{1-x}As$/GaAs heterostructure nanowires, *Phys. Rev. B* **87**, 235304 (2013).

[12] J. Tatebayashi, Y. Ota, S. Ishida, M. Nishioka, S. Iwamoto, and Y. Arakawa, Site-controlled formation of InAs/GaAs quantum-dot-in-nanowires for single photon emitters, *Appl. Phys. Lett.* **100**, 263101 (2012).

[13] E. Uccelli, J. Arbiol, J. R. Morante, and A. Fontcuberta i Morral, InAs quantum dot arrays decorating the facets of GaAs nanowires., *ACS nano* **4**, 5985–5993 (2010).

[14] R. B. Lewis, P. Corfdir, J. Herranz, H. Küpers, U. Jahn, O. Brandt, and L. Geelhaar, Self-Assembly of InAs Nanostructures on the Sidewalls of GaAs Nanowires Directed by a Bi Surfactant, *Nano Lett.* **17**, 4255–4260 (2017).

[15] A. Fontcuberta i Morral, D. Spirkoska, J. Arbiol, M. Heigoldt, J. Ramon Morante, and G. Abstreiter, Prismatic quantum heterostructures synthesized on molecular-beam epitaxy GaAs nanowires, *Small* **4**, 899–903 (2008).

[16] M. Moewe, L. C. Chuang, S. Crankshaw, K. W. Ng, and C. Chang-Hasnain, Core-shell InGaAs/GaAs quantum well nanoneedles grown on silicon with silicon-transparent emission, *Opt. Express* **17**, 7831 (2009).

[17] E. Dimakis, U. Jahn, M. Ramsteiner, A. Tahraoui, J. Grandal, X. Kong, O. Marquardt, A. Trampert, H. Riechert, and L. Geelhaar, Coaxial Multishell (In,Ga)As/GaAs Nanowires for Near-Infrared Emission on Si Substrates, *Nano Lett.* **14**, 2604–2609 (2014).

[18] K. W. Park, C. Y. Park, S. Ravindran, J.-S. Jang, Y.-R. Jo, B.-J. Kim, and Y. T. Lee, Observation and tunability of room temperature photoluminescence of GaAs/GaInAs core-multiple-quantum-well shell nanowire structure grown on Si (100) by molecular beam epitaxy, *Nanoscale Res. Lett.* **9**, 626 (2014).

[19] X. Yan, X. Zhang, J. Li, Y. Wu, J. Cui, and X. Ren, Fabrication and optical properties of GaAs/InGaAs/GaAs nanowire core–multishell quantum well heterostructures, *Nanoscale* **7**, 1110–5 (2015).

[20] R. B. Lewis, L. Nicolai, H. Küpers, M. Ramsteiner, A. Trampert, and L. Geelhaar, Anomalous Strain Relaxation in Core-Shell Nanowire Heterostructures via Simultaneous Coherent and Incoherent Growth, *Nano Lett.* **17**, 136–142 (2017).

[21] I. Giuntoni, L. Geelhaar, J. Bruns, and H. Riechert, Light coupling between vertical III-As nanowires and planar Si photonic waveguides for the monolithic integration of active optoelectronic devices on a Si platform, *Opt. Express* **24**, 18417 (2016).

[22] A. Y. Cho, How molecular beam epitaxy (MBE) began and its projection into the future, *J. Cryst. Growth* **201**, 1–7 (1999).

[23] A. Y. Cho, Morphology of epitaxial growth of GaAs by a molecular beam method: The observation of surface structures, *J. Appl. Phys.* **41**, 2780–2786 (1970).

[24] A. Y. Cho and H. C. Casey, GaAs-$Al_xGa_{1-x}As$ double-heterostructure lasers prepared by molecular-beam epitaxy, *Appl. Phys. Lett.* **25**, 288–290 (1974).

[25] L. Esaki and R. Tsu, Superlattice and Negative Differential Conductivity in Semiconductors, *IBM J. Res. Dev.* **14**, 61–65 (1970).

[26] I. V. Markov, *Crystal growth for beginners - Fundamentals of Nucleation, Crystal growth and Epitaxy*, World Scientific Publishing Co. Pte. Ltd. (2003).

[27] A. Ichimiya and P. I. Cohen, *Reflection high-energy electron diffraction*, Cambridge University Press (2004).

[28] C. Sartel, D. L. Dheeraj, F. Jabeen, and J.-C. Harmand, Effect of arsenic species on the kinetics of GaAs nanowires growth by molecular beam epitaxy, *J. Cryst. Growth* **312**, 2073–2077 (2010).

[29] A. Y. Cho, Bonding direction and surface-structure orientation on GaAs (001), *J. Appl. Phys.* **47**, 2841–2843 (1976).

[30] L. Däweritz and R. Hey, Reconstruction and defect structure of vicinal GaAs(001) and $Al_xGa_{1-x}As$(001) surfaces during MBE growth, *Surf. Sci.* **236**, 15 (1990).

[31] R. D. Richards, F. Bastiman, C. J. Hunter, D. F. Mendes, A. R. Mohmad, J. S. Roberts, and J. P. David, Molecular beam epitaxy growth of GaAsBi using As_2 and As_4, *J. Cryst. Growth* **390**, 120–124 (2014).

[32] P. Y. Yu and M. Cardona, *Fundamentals of Semiconductors: Physics and Material Properties*, Graduate Text in Physics, Springer, 4th edition (2010).

[33] D. Strauch and B. Dorner, Phonon dispersion in GaAs, *J. Phys. Condens. Matter* **2**, 1457–1474 (1990).

[34] C. Hauswald, *Dynamics of free and bound excitons in GaN nanowires*, PhD thesis, Humboldt-Universität zu Berlin, Mathematisch-Naturwissenschaftliche Fakultät I (2015).

[35] W. C. Dash and R. Newman, Intrinsic Optical Absorption in Single-Crystal Germanium and Silicon at 77°K and 300°K, *Phys. Rev.* **99**, 1151–1155 (1955).

[36] F. Jabeen, V. Grillo, S. Rubini, and F. Martelli, Self-catalyzed growth of GaAs nanowires on cleaved Si by molecular beam epitaxy, *Nanotechnology* **19**, 275711 (2008).

[37] C. Colombo, D. Spirkoska, M. Frimmer, G. Abstreiter, and A. Fontcuberta i Morral, Ga-assisted catalyst-free growth mechanism of GaAs nanowires by molecular beam epitaxy, *Phys. Rev. B* **77**, 155326 (2008).

[38] K. Hiruma, T. Katsuyama, K. Ogawa, M. Koguchi, H. Kakibayashi, and G. P. Morgan, Quantum size microcrystals grown using organometallic vapor phase epitaxy, *Appl. Phys. Lett.* **59**, 431–433 (1991).

[39] B. Bauer, A. Rudolph, M. Soda, A. Fontcuberta i Morral, J. Zweck, D. Schuh, and E. Reiger, Position controlled self-catalyzed growth of GaAs nanowires by molecular beam epitaxy, *Nanotechnology* **21**, 435601 (2010).

[40] S. Plissard, K. a. Dick, G. Larrieu, S. Godey, A. Addad, X. Wallart, and P. Caroff, Gold-free growth of GaAs nanowires on silicon: arrays and polytypism, *Nanotechnology* **21**, 385602 (2010).

[41] S. J. Gibson, J. P. Boulanger, and R. R. LaPierre, Opportunities and pitfalls in patterned self-catalyzed GaAs nanowire growth on silicon, *Semicond. Sci. Technol.* **28**, 105025 (2013).

[42] A. M. Munshi, D. L. Dheeraj, V. T. Fauske, D. C. Kim, J. Huh, J. F. Reinertsen, L. Ahtapodov, K. D. Lee, B. Heidari, A. T. J. van Helvoort, B. O. Fimland, and H. Weman, Position-Controlled Uniform GaAs Nanowires on Silicon using Nanoimprint Lithography, *Nano Lett.* **14**, 960–6 (2014).

[43] M. Heiss, E. Russo-Averchi, a. Dalmau-Mallorquí, G. Tütüncüoğlu, F. Matteini, D. Rüffer, S. Conesa-Boj, O. Demichel, E. Alarcon-Lladó, and A. Fontcuberta i Morral, III-V nanowire arrays: growth and light interaction, *Nanotechnology* **25**, 014015 (2014).

[44] S. Plissard, G. Larrieu, X. Wallart, and P. Caroff, High yield of self-catalyzed GaAs nanowire arrays grown on silicon via gallium droplet positioning., *Nanotechnology* **22**, 275602 (2011).

[45] H. Küpers, A. Tahraoui, R. B. Lewis, S. Rauwerdink, M. Matalla, O. Krüger, F. Bastiman, H. Riechert, and L. Geelhaar, Surface preparation and patterning by nano imprint lithography for the selective area growth of GaAs nanowires on Si(111), *Semicond. Sci. Technol.* **32**, 115003 (2017).

[46] H. Küpers, R. B. Lewis, A. Tahraoui, M. Matalla, O. Krüger, F. Bastiman, H. Riechert, and L. Geelhaar, Diameter evolution of selective area grown Ga-assisted GaAs nanowires, *Nano Res.* (2018).

[47] R. S. Wagner and W. C. Ellis, Vapor-liquid-solid mechanism of single crystal growth, *Appl. Phys. Lett.* **4**, 89–90 (1964).

[48] N. P. Dasgupta, J. Sun, C. Liu, S. Brittman, S. C. Andrews, J. Lim, H. Gao, R. Yan, and P. Yang, 25th anniversary article: semiconductor nanowires–synthesis, characterization, and applications., *Adv. Mater.* **26**, 2137–84 (2014).

[49] K. Hiruma, M. Yazawa, T. Katsuyama, K. Ogawa, K. Haraguchi, M. Koguchi, and H. Kakibayashi, Growth and optical properties of nanometer-scale GaAs and InAs whiskers, *Applied Physics Reviews* **77**, 447–462 (1995).

[50] J. C. Harmand, G. Patriarche, N. Pere-Laperne, M. N. Mrat-Combes, L. Travers, and F. Glas, Analysis of vapor-liquid-solid mechanism in Au-assisted GaAs nanowire growth, *Appl. Phys. Lett.* **87**, 1–3 (2005).

[51] P. Mohan, J. Motohisa, and T. Fukui, Controlled growth of highly uniform, axial/radial direction-defined, individually addressable InP nanowire arrays, *Nanotechnology* **16**, 2903–2907 (2005).

[52] K. A. Dick and P. Caroff, Metal-seeded growth of III-V semiconductor nanowires: towards gold-free synthesis, *Nanoscale* **6**, 3006–21 (2014).

[53] C. Lindberg, A. Whiticar, K. A. Dick, N. Sköld, J. Nygård, and J. Bolinsson, Silver as Seed-Particle Material for GaAs Nanowires—Dictating Crystal Phase and Growth Direction by Substrate Orientation, *Nano Lett.* **16**, 2181–2188 (2016).

[54] R. Sun, N. Vainorius, D. Jacobsson, M.-E. Pistol, S. Lehmann, and K. A. Dick, Sn-seeded GaAs nanowires grown by MOVPE, *Nanotechnology* **27**, 215603 (2016).

[55] S. Brotherton and J. Lowther, Electron and Hole Capture at Au and Pt Centers in Silicon, *Phys. Rev. Lett.* **44**, 606–609 (1980).

[56] S. Breuer, C. Pfüller, T. Flissikowski, O. Brandt, H. T. Grahn, L. Geelhaar, and H. Riechert, Suitability of Au- and self-assisted GaAs nanowires for optoelectronic applications, *Nano Lett.* **11**, 1276–1279 (2011).

[57] N. Jiang, P. Parkinson, Q. Gao, S. Breuer, H. H. Tan, J. Wong-Leung, and C. Jagadish, Long minority carrier lifetime in Au-catalyzed GaAs/$Al_xGa_{1-x}As$ core-shell nanowires, *Appl. Phys. Lett.* **101**, 023111 (2012).

[58] S. Ermez, E. J. Jones, S. C. Crawford, and S. Gradečak, Self-Seeded Growth of GaAs Nanowires by Metal-Organic Chemical Vapor Deposition, *Crystal Growth & Design* **15**, 2768–2774 (2015).

[59] Z. Dong, Y. André, V. Dubrovskii, C. Bougerol, C. Leroux, M. Ramdani, G. Monier, A. Trassoudaine, D. Castelluci, and E. Gil, Self-catalyzed GaAs nanowires on silicon by hydride vapor phase epitaxy, *Nanotechnology* **28** (2017).

[60] F. Glas, J.-C. Harmand, and G. Patriarche, Nucleation Antibunching in Catalyst-Assisted Nanowire Growth, *Phys. Rev. Lett.* **104**, 135501 (2010).

[61] F. Glas and V. G. Dubrovskii, Self-narrowing of size distributions of nanostructures by nucleation antibunching, *Physical Review Materials* **1**, 036003 (2017).

[62] H. Küpers, F. Bastiman, E. Luna, C. Somaschini, and L. Geelhaar, Ga predeposition for the Ga-assisted growth of GaAs nanowire ensembles with low number density and homogeneous length, *J. Cryst. Growth* **459**, 43–49 (2017).

[63] A. Fontcuberta i Morral, C. Colombo, G. Abstreiter, J. Arbiol, and J. R. Morante, Nucleation mechanism of gallium-assisted molecular beam epitaxy growth of gallium arsenide nanowires, *Appl. Phys. Lett.* **92**, 63112 (2008).

[64] T. Tauchnitz, T. Nurmamytov, R. Hübner, M. Engler, S. Facsko, H. Schneider, M. Helm, and E. Dimakis, Decoupling the Two Roles of Ga Droplets in the Self-Catalyzed Growth of GaAs Nanowires on SiO_x/Si(111) Substrates, *Crystal Growth & Design* **17**, 5276–5282 (2017).

[65] M. R. Ramdani, J.-C. C. Harmand, F. Glas, G. Patriarche, and L. Travers, Arsenic Pathways in Self-Catalyzed Growth of GaAs Nanowires, *Crystal Growth & Design* **13**, 91–96 (2013).

[66] K. Tomioka, Y. Kobayashi, J. Motohisa, S. Hara, and T. Fukui, Selective-area growth of vertically aligned GaAs and GaAs/AlGaAs core-shell nanowires on Si(111) substrate, *Nanotechnology* **20**, 145302 (2009).

[67] A. Davydok, S. Breuer, A. Biermanns, L. Geelhaar, and U. Pietsch, Lattice parameter accommodation between GaAs(111) nanowires and Si(111) substrate after growth via Au-assisted molecular beam epitaxy, *Nanoscale Res. Lett.* **7**, 109 (2012).

[68] F. Glas, Strain in Nanowires and Nanowire Heterostructures, In *Semiconductors and Semimetals -Semiconductor Nanowires I: Growth and Theory*, volume 93, chapter 2, pages 79–123, Elsevier Inc., 1 edition (2015).

[69] R. La, R. Liu, W. Yao, R. Chen, M. Jansson, J. L. Pan, I. A. Buyanova, J. Xiang, S. A. Dayeh, and C. W. Tu, Self-catalyzed core-shell GaAs/GaNAs nanowires grown on patterned Si (111) by gas-source molecular beam epitaxy, *Appl. Phys. Lett.* **111** (2017).

[70] T. Mårtensson, C. P. T. Svensson, B. A. Wacaser, M. W. Larsson, W. Seifert, K. Deppert, A. Gustafsson, L. R. Wallenberg, and L. Samuelson, Epitaxial III-V Nanowires on Silicon, *Nano Lett.* **4**, 1987–1990 (2004).

[71] W. I. Wang, Molecular beam epitaxial growth and material properties of GaAs and AlGaAs on Si (100), *Appl. Phys. Lett.* **44**, 1149 (1984).

[72] M. Yamaguchi, A. Yamamoto, M. Tachikawa, Y. Itoh, and M. Sugo, Defect reduction effects in GaAs on Si substrates by thermal annealing, *Appl. Phys. Lett.* **53**, 2293–2295 (1988).

[73] E. a. Fitzgerald, Y.-H. Xie, M. L. Green, D. Brasen, a. R. Kortan, J. Michel, Y.-J. Mii, and B. E. Weir, Totally relaxed Ge_xSi_{1-x} layers with low threading dislocation densities grown on Si substrates, *Appl. Phys. Lett.* **59**, 811 (1991).

[74] C.-Y. Yeh, Z. W. Lu, S. Froyen, and A. Zunger, Zinc-blende–wurtzite polytypism in semiconductors, *Phys. Rev. B* **46**, 10086–10097 (1992).

[75] M. Koguchi, H. Kakibayashi, M. Yazawa, K. Hiruma, and T. Katsuyama, Crystal Structure Change of GaAs and InAs Whiskers from Zinc-Blende to Wurtzite Type, *Jpn. J. Appl. Phys.* **31**, 2061–2065 (1992).

[76] I. P. Soshnikov, G. E. Cirlin, A. A. Tonkikh, Y. B. Samsonenko, V. G. Dubrovskii, V. M. Ustinov, O. M. Gorbenko, D. Litvinov, and D. Gerthsen, Atomic Structure of MBE-Grown GaAs Nanowhiskers, *Phys. Solid State* **47**, 2213 (2005).

[77] S. Lehmann, D. Jacobsson, and K. A. Dick, Crystal phase control in GaAs nanowires: opposing trends in the Ga- and As-limited growth regimes, *Nanotechnology* **26**, 301001 (2015).

[78] B. A. Wacaser, K. A. Dick, J. Johansson, M. T. Borgström, K. Deppert, and L. Samuelson, Preferential interface nucleation: an expansion of the VLS growth mechanism for nanowires, *Adv. Mater.* **21**, 153–165 (2009).

[79] F. Glas, J.-C. Harmand, and G. Patriarche, Why does wurtzite form in nanowires of III-V zinc blende semiconductors?, *Phys. Rev. Lett.* **99**, 146101 (2007).

[80] D. Jacobsson, F. Panciera, J. Tersoff, M. C. Reuter, S. Lehmann, S. Hofmann, K. A. Dick, and F. M. Ross, Interface dynamics and crystal phase switching in GaAs nanowires, *Nature* **531**, 317 (2016).

[81] M. Heiss, S. Conesa-Boj, J. Ren, H.-H. Tseng, A. Gali, A. Rudolph, E. Uccelli, F. Peiró, J. R. Morante, D. Schuh, E. Reiger, E. Kaxiras, J. Arbiol, and A. Fontcuberta i Morral, Direct correlation of crystal structure and optical properties in wurtzite/zinc-blende GaAs nanowire heterostructures, *Phys. Rev. B* **83**, 045303 (2011).

[82] P. Corfdir, C. Hauswald, J. K. Zettler, T. Flissikowski, J. Lähnemann, S. Fernández-Garrido, L. Geelhaar, H. T. Grahn, and O. Brandt, Stacking faults as quantum wells in nanowires: Density of states, oscillator strength, and radiative efficiency, *Phys. Rev. B* **90**, 195309 (2014).

[83] G. S. Higashi, Y. J. Chabal, G. W. Trucks, and K. Raghavachari, Ideal hydrogen termination of the Si (111) surface, *Appl. Phys. Lett.* **56**, 656–658 (1990).

[84] G. S. Higashi, R. S. Becker, Y. J. Chabal, and a. J. Becker, Comparison of Si(111) surfaces prepared using aqueous solutions of NH_4F versus HF, *Appl. Phys. Lett.* **58**, 1656–1658 (1991).

[85] S. Watanabe, M. Shigeno, N. Nakayama, and T. Ito, Silicon-Monohydride Termination of Silicon (111) Surface Formed by Boiling Water, *Jpn. J. Appl. Phys.* **30**, 3575–3579 (1991).

[86] S. Watanabe, N. Nakayama, and T. Ito, Homogeneous hydrogen-terminated Si(111) surface formed using aqueous HF solution and water, *Appl. Phys. Lett.* **59**, 1458–1460 (1991).

[87] G. Pietsch, U. Köhler, and M. Henzler, Direct observation of silicon surface etching by water with scanning tunneling microscopy, *Chem. Phys. Lett.* **197**, 346–351 (1992).

[88] S. K. Yang, S. Peter, and C. G. Takoudis, Fundamentals of two-step etching techniques for ideal silicon-hydrogen termination of silicon (111), *J. Appl. Phys.* **76**, 4107–4112 (1994).

[89] F. Matteini, G. Tütüncüoglu, H. Potts, F. Jabeen, and A. Fontcuberta i Morral, Wetting of Ga on SiO_x and Its Impact on GaAs Nanowire Growth, *Crystal Growth & Design* **15**, 3105–3109 (2015).

[90] F. Bastiman, H. Küpers, C. Somaschini, and L. Geelhaar, Growth map for Ga-assisted growth of GaAs nanowires on Si(111) substrates by molecular beam epitaxy, *Nanotechnology* **27**, 095601 (2016).

[91] M. Heiß, E. Riedlberger, D. Spirkoska, M. Bichler, G. Abstreiter, and A. Fontcuberta i Morral, Growth mechanisms and optical properties of GaAs-based semiconductor microstructures by selective area epitaxy, *J. Cryst. Growth* **310**, 1049–1056 (2008).

[92] A. Pierret, M. Hocevar, S. L. Diedenhofen, R. E. Algra, E. Vlieg, E. C. Timmering, M. a. Verschuuren, G. W. G. Immink, M. a. Verheijen, and E. P. A. M. Bakkers, Generic nano-imprint process for fabrication of nanowire arrays, *Nanotechnology* **21**, 065305 (2010).

[93] S. Hertenberger, S. Funk, K. Vizbaras, a. Yadav, D. Rudolph, J. Becker, S. Bolte, M. Döblinger, M. Bichler, G. Scarpa, P. Lugli, I. Zardo, J. J. Finley, M. Amann, G. Abstreiter, and G. Koblmüller, High compositional homogeneity in In-rich InGaAs nanowire arrays on nanoimprinted SiO_2/Si (111), *Appl. Phys. Lett.* **101**, 043116 (2012).

[94] S. D. Hersee, X. Sun, and X. Wang, The controlled growth of GaN nanowires., *Nano Lett.* **6**, 1808–1811 (2006).

[95] J. Motohisa, J. Noborisaka, J. Takeda, M. Inari, and T. Fukui, Catalyst-free selective-area MOVPE of semiconductor nanowires on (111) B oriented substrates, *J. Cryst. Growth* **272**, 180–185 (2004), The Twelfth International Conference on Metalorganic Vapor Phase Epitaxy.

[96] Y. Zhang, J. Wu, M. Aagesen, J. Holm, S. Hatch, M. Tang, S. Huo, and H. Liu, Self-catalyzed ternary core-shell GaAsP nanowire arrays grown on patterned Si substrates by molecular beam epitaxy, *Nano Lett.* **14**, 4542–4547 (2014).

[97] S. Gibson and R. LaPierre, III-V nanowire photovoltaics: Review of design for high efficiency, *Phys. Status Solidi RRL* **7**, 845–849 (2013).

[98] D. Rudolph, L. Schweickert, S. Morkötter, B. Loitsch, S. Hertenberger, J. Becker, M. Bichler, G. Abstreiter, J. J. Finley, and G. Koblmüller, Effect of interwire separation on growth kinetics and properties of site-selective GaAs nanowires, *Appl. Phys. Lett.* **105**, 033111 (2014).

[99] M. Munsch, N. S. Malik, E. Dupuy, A. Delga, J. Bleuse, J.-M. Gérard, J. Claudon, N. Gregersen, and J. Mørk, Dielectric GaAs Antenna Ensuring an Efficient Broadband Coupling between an InAs Quantum Dot and a Gaussian Optical Beam, *Phys. Rev. Lett.* **110**, 177402 (2013).

[100] Y. Cui, L. J. Lauhon, M. S. Gudiksen, J. Wang, and C. M. Lieber, Diameter-controlled synthesis of single-crystal silicon nanowires, *Appl. Phys. Lett.* **78**, 2214 (2001).

[101] J.-H. Paek, T. Nishiwaki, M. Yamaguchi, and N. Sawaki, Catalyst free MBE-VLS growth of GaAs nanowires on (111) Si substrate, *Phys. Status Solidi C* **6**, 1436–1440 (2009).

[102] D. Rudolph, S. Hertenberger, S. Bolte, W. Paosangthong, D. Spirkoska, M. Döblinger, M. Bichler, J. J. Finley, G. Abstreiter, and G. Koblmüller, Direct observation of a noncatalytic growth regime for GaAs nanowires, *Nano Lett.* **11**, 3848–3854 (2011).

[103] P. Krogstrup, H. I. Jørgensen, E. Johnson, M. H. Madsen, C. B. Sørensen, A. Fontcuberta i Morral, M. Aagesen, J. Nygård, and F. Glas, Advances in the theory of III-V nanowire growth dynamics, *J. Phys. D: Appl. Phys.* **46**, 313001 (2013).

[104] J. Tersoff, Stable Self-Catalyzed Growth of III-V Nanowires, *Nano Lett.* **15**, 6609–6613 (2015).

[105] V. G. Dubrovskii, Group V sensitive vapor-liquid-solid growth of Au-catalyzed and self-catalyzed III-V nanowires, *J. Cryst. Growth* **440**, 62–68 (2016).

[106] Y. Wang, V. Schmidt, S. Senz, and U. Gösele, Epitaxial growth of silicon nanowires using an aluminium catalyst, *Nat. Nanotechnol.* **1**, 186–189 (2006).

[107] P. Paiano, P. Prete, N. Lovergine, and A. M. Mancini, Size and shape control of GaAs nanowires grown by metalorganic vapor phase epitaxy using tertiarybutylarsine, *J. Appl. Phys.* **100**, 094305 (2006).

[108] S. Krylyuk, A. V. Davydov, and I. Levin, Tapering Control of Si Nanowires Grown from $SiCl_4$ at Reduced Pressure, *ACS Nano* **5**, 656–664 (2011).

[109] T. Rieger, S. Heiderich, S. Lenk, M. I. Lepsa, and D. Grützmacher, Ga-assisted MBE growth of GaAs nanowires using thin HSQ layer, *J. Cryst. Growth* **353**, 39–46 (2012).

[110] F. Oehler, A. Cattoni, A. Scaccabarozzi, G. Patriarche, F. Glas, and J.-c. Harmand, Measuring and modeling the growth dynamics of self-catalyzed GaP nanowire arrays, *Nano Lett.* **18**, acs.nanolett.7b03695 (2018).

[111] V. G. Dubrovskii, T. Xu, A. Diaz, S. R. Plissard, P. Caroff, F. Glas, and B. Grandidier, Self-equilibration of the diameter of Ga-catalyzed GaAs nanowires, *Nano Lett.* **15**, 5580–5584 (2015).

[112] J. Ralston, G. W. Wicks, and L. F. Eastman, Reflection high-energy electron diffraction intensity oscillation study of Ga desorption from molecular beam epitaxially grown $Al_xGa_{1-x}As$, *J. Vac. Sci. Technol. B* **4**, 594–597 (1986).

[113] A. Fick, Ueber Diffusion, *Annalen der Physik und Chemie* **170**, 59–86 (1855).

[114] F. Glas, Vapor fluxes on the apical droplet during nanowire growth by molecular beam epitaxy, *Phys. Status Solidi B* **247**, 254–258 (2010).

[115] V. G. Dubrovskii, N. V. Sibirev, J. C. Harmand, and F. Glas, Growth kinetics and crystal structure of semiconductor nanowires, *Phys. Rev. B* **78**, 235301 (2008).

[116] V. G. Dubrovskii, Y. Berdnikov, and N. V. Sibirev, Regimes of radial growth for Ga-catalyzed GaAs nanowires, *Applied Physics A* **122**, 671 (2016).

[117] G. Priante, S. Ambrosini, V. G. Dubrovskii, A. Franciosi, and S. Rubini, Stopping and Resuming at Will the Growth of GaAs Nanowires, *Crystal Growth & Design* **13**, 3976–3984 (2013).

[118] D. E. Perea, E. R. Hemesath, E. J. Schwalbach, J. L. Lensch-Falk, P. W. Voorhees, and L. J. Lauhon, Direct measurement of dopant distribution in an individual vapour–liquid–solid nanowire, *Nat. Nanotechnol.* **4**, 315–319 (2009).

[119] L. J. Lauhon, P. Adusumilli, P. Ronsheim, P. L. Flaitz, and D. Lawrence, Atom-Probe Tomography of Semiconductor Materials and Device Structures, *MRS Bull.* **34**, 738–743 (2009).

[120] J. Dufouleur, C. Colombo, T. Garma, B. Ketterer, E. Uccelli, M. Nicotra, and A. Fontcuberta i Morral, P-Doping Mechanisms in Catalyst-Free Gallium Arsenide Nanowires, *Nano Lett.* **10**, 1734–1740 (2010).

[121] J. Wallentin and M. T. Borgström, Doping of semiconductor nanowires, *J. Mater. Res.* **26**, 2142–2156 (2011).

[122] E. Dimakis, M. Ramsteiner, A. Tahraoui, H. Riechert, and L. Geelhaar, Shell-doping of GaAs nanowires with Si for n-type conductivity, *Nano Res.* **5**, 796–804 (2012).

[123] J. G. Connell, K. Yoon, D. E. Perea, E. J. Schwalbach, P. W. Voorhees, and L. J. Lauhon, Identification of an Intrinsic Source of Doping Inhomogeneity in Vapor-Liquid-Solid-Grown Nanowires, *Nano Lett.* **13**, 199–206 (2013).

[124] A. Casadei, P. Krogstrup, M. Heiss, J. a. Rohr, C. Colombo, T. Ruelle, S. Upadhyay, C. B. Sorensen, J. Nygard, and A. Fontcuberta i Morral, Doping incorporation paths in catalyst-free Be-doped GaAs nanowires, *Appl. Phys. Lett.* **102**, 013117 (2013).

[125] Y. Zhang, Z. Sun, A. M. Sanchez, M. Ramsteiner, M. Aagesen, J. Wu, D. Kim, P. Jurczak, S. Huo, L. J. Lauhon, and H. Liu, Doping of Self-Catalyzed Nanowires under the Influence of Droplets, *Nano Lett.* **18**, 81–87 (2018).

[126] M. Hilse, M. Ramsteiner, S. Breuer, L. Geelhaar, and H. Riechert, Incorporation of the dopants Si and Be into GaAs nanowires, *Appl. Phys. Lett.* **96**, 193104 (2010).

[127] R. Dingle, H. L. Störmer, A. C. Gossard, and W. Wiegmann, Electron mobilities in modulation-doped semiconductor heterojunction superlattices, *Appl. Phys. Lett.* **33**, 665–667 (1978).

[128] I. Amit, U. Givan, J. G. Connell, D. F. Paul, J. S. Hammond, L. J. Lauhon, and Y. Rosenwaks, Spatially Resolved Correlation of Active and Total Doping Concentrations in VLS Grown Nanowires, *Nano Lett.* **13**, 2598–2604 (2013).

[129] M. H. T. Dastjerdi, E. M. Fiordaliso, E. D. Leshchenko, A. Akhtari-Zavareh, T. Kasama, M. Aagesen, V. G. Dubrovskii, and R. R. LaPierre, Three-fold Symmetric Doping Mechanism in GaAs Nanowires, *Nano Lett.* **17**, 5875–5882 (2017).

[130] R. B. Beall, J. B. Clegg, J. Castagne, J. J. Harris, R. Murray, and R. C. Newman, Post-growth diffusion of Si in delta -doped GaAs grown by MBE, *Semicond. Sci. Technol.* **4**, 1171–1175 (1989).

[131] J. J. Harris, J. B. Clegg, R. B. Beall, J. Castagné, K. Woodbridge, and C. Roberts, Delta-doping of GaAs and $Al_0.33Ga_0.67As$ with Sn, Si and Be: a comparative study, *J. Cryst. Growth* **111**, 239–245 (1991).

[132] M. T. Borgström, G. Immink, B. Ketelaars, R. Algra, and E. P. Bakkers, Synergetic nanowire growth, *Nat. Nanotechnol.* **2**, 541–544 (2007).

[133] L. J. Lauhon, M. S. Gudiksen, D. Wang, and C. M. Lieber, Epitaxial core-shell and core-multishell nanowire heterostructures, *Nature* **420**, 57–61 (2002).

[134] G. Koblmüller, B. Mayer, T. Stettner, G. Abstreiter, and J. J. Finley, GaAs-AlGaAs core-shell nanowire lasers on silicon: invited review, *Semicond. Sci. Technol.* **32**, 053001 (2017).

[135] J. Grönqvist, N. Søndergaard, F. Boxberg, T. Guhr, S. Åberg, and H. Q. Xu, Strain in semiconductor core–shell nanowires, *J. Appl. Phys.* **106**, 053508 (2009).

[136] K. L. Kavanagh, Misfit dislocations in nanowire heterostructures, *Semicond. Sci. Technol.* **25**, 024006 (2010).

[137] O. Salehzadeh, K. L. Kavanagh, and S. P. Watkins, Geometric limits of coherent III-V core/shell nanowires, *J. Appl. Phys.* **114** (2013).

[138] M. Y. Gutkin, A. L. Kolesnikova, S. A. Krasnitcky, and A. E. Romanov, Misfit dislocation loops in composite core–shell nanoparticles, *Phys. Solid State* **56**, 695–702 (2014).

[139] X. Ji, X. Yang, W. Du, H. Pan, S. Luo, H. Ji, H. Q. Xu, and T. Yang, InAs/GaSb core-shell nanowires grown on Si substrates by metal-organic chemical vapor deposition, *Nanotechnology* **27**, 275601 (2016).

[140] L.-f. Cui, Y. Yang, C.-m. Hsu, and Y. Cui, Carbon - Silicon Core–Shell Nanowires as High Capacity Electrode for Lithium Ion Batteries 2009, *Nano Lett.* **9 No.9**, 1–5 (2009).

[141] A. Mikkelsen, N. Sköld, L. Ouattara, M. T. Borgström, J. N. Andersen, L. Samuelson, W. Seifert, and E. Lundgren, Direct imaging of the atomic structure inside a nanowire by scanning tunnelling microscopy, *Nat. Mater.* **3**, 519–23 (2004).

[142] L. V. Titova, T. B. Hoang, H. E. Jackson, L. M. Smith, J. M. Yarrison-Rice, Y. Kim, H. J. Joyce, H. H. Tan, and C. Jagadish, Temperature dependence of photoluminescence from single core-shell GaAs-AlGaAs nanowires, *Appl. Phys. Lett.* **89**, 173126 (2006).

[143] K. Moratis, S. L. Tan, S. Germanis, C. Katsidis, M. Androulidaki, K. Tsagaraki, Z. Hatzopoulos, F. Donatini, J. Cibert, Y.-M. M. Niquet, H. Mariette, and N. T. Pelekanos, Strained GaAs/InGaAs Core-Shell Nanowires for Photovoltaic Applications, *Nanoscale Res. Lett.* **11**, 176 (2016).

[144] M. Heurlin, T. Stankevič, S. Mickevičius, S. Yngman, D. Lindgren, A. Mikkelsen, R. Feidenhans'l, M. T. Borgström, and L. Samuelson, Structural Properties of Wurtzite InP-InGaAs Nanowire Core-Shell Heterostructures, *Nano Lett.* **15**, 2462–2467 (2015).

[145] H. A. Fonseka, A. S. Ameruddin, P. Caroff, D. Tedeschi, M. De Luca, F. Mura, Y. Guo, M. Lysevych, F. Wang, H. H. Tan, A. Polimeni, and C. Jagadish, InP-$In_xGa_{1-x}As$ core–multi-shell nanowire quantum wells with tunable emission in the 1.3–1.55 μm wavelength range, *Nanoscale* **9**, 13554–13562 (2017).

[146] I. Vurgaftman, J. R. Meyer, and L. R. Ram-Mohan, Band parameters for III-V compound semiconductors and their alloys, *J. Appl. Phys.* **89**, 5815 (2001).

[147] R. E. Nahory, M. A. Pollack, W. D. Johnston, and R. L. Barns, Band gap versus composition and demonstration of Vegard's law for $In_{1-x}Ga_xAs_yP_{1-y}$ lattice matched to InP, *Appl. Phys. Lett.* **33**, 659–661 (1978).

[148] C. T. Foxon, S. Novikov, J. Hall, R. Campion, D. Cherns, I. Griffiths, and S. Khongphetsak, A complementary geometric model for the growth of GaN nanocolumns prepared by plasma-assisted molecular beam epitaxy, *J. Cryst. Growth* **311**, 3423–3427 (2009).

[149] M. López and Y. Nomura, Surface diffusion length of Ga adatoms in molecular-beam epitaxy on GaAs(100)-(110) facet structures, *J. Cryst. Growth* **150**, 68–72 (1995).

[150] Y. Heon Kim, D. Woo Park, and S. Jun Lee, Gallium-droplet behaviors of self-catalyzed GaAs nanowires: A transmission electron microscopy study, *Appl. Phys. Lett.* **100**, 033117 (2012).

[151] J. Grandal, M. Wu, X. Kong, M. Hanke, E. Dimakis, L. Geelhaar, H. Riechert, and A. Trampert, Plan-view transmission electron microscopy investigation of GaAs/(In,Ga)As core–shell nanowires, *Appl. Phys. Lett.* **105**, 121602 (2014).

[152] G. Biasiol and E. Kapon, Mechanisms of Self-Ordering of Quantum Nanostructures Grown on Nonplanar Surfaces, *Phys. Rev. Lett.* **81**, 2962–2965 (1998).

[153] G. Biasiol, A. Gustafsson, K. Leifer, and E. Kapon, Mechanisms of self-ordering in nonplanar epitaxy of semiconductor nanostructures, *Phys. Rev. B* **65**, 1–15 (2002).

[154] M. Heiss, Y. Fontana, A. Gustafsson, G. Wüst, C. Magen, D. D. O'Regan, J. W. Luo, B. Ketterer, S. Conesa-Boj, A. V. Kuhlmann, J. Houel, E. Russo-Averchi, J. R.

Morante, M. Cantoni, N. Marzari, J. Arbiol, A. Zunger, R. J. Warburton, and A. Fontcuberta i Morral, Self-assembled quantum dots in a nanowire system for quantum photonics, *Nat. Mater.* **12**, 439–444 (2013).

[155] D. Rudolph, S. Funk, M. Döblinger, S. Morkötter, S. Hertenberger, L. Schweickert, J. Becker, S. Matich, M. Bichler, D. Spirkoska, I. Zardo, J. J. Finley, G. Abstreiter, and G. Koblmüller, Spontaneous alloy composition ordering in GaAs-AlGaAs core-shell nanowires., *Nano Lett.* **13**, 1522–7 (2013).

[156] J. B. Wagner, N. Sköld, L. Reine Wallenberg, and L. Samuelson, Growth and segregation of GaAs-$Al_xIn_{1-x}P$ core–shell nanowires, *J. Cryst. Growth* **312**, 1755–1760 (2010).

[157] L. Mancini, Y. Fontana, S. Conesa-Boj, I. Blum, F. Vurpillot, L. Francaviglia, E. Russo-Averchi, M. Heiss, J. Arbiol, A. Fontcuberta i Morral, and L. Rigutti, Three-dimensional nanoscale study of Al segregation and quantum dot formation in GaAs/AlGaAs core-shell nanowires, *Appl. Phys. Lett.* **105**, 243106 (2014).

[158] N. Jeon, B. Loitsch, S. Morkoetter, G. Abstreiter, J. Finley, H. J. Krenner, G. Koblmüller, and L. J. Lauhon, Alloy Fluctuations Act as Quantum Dot-like Emitters in GaAs-AlGaAs Core-Shell Nanowires, *ACS Nano* **9**, 8335–8343 (2015).

[159] Y. Fontana, P. Corfdir, B. Van Hattem, E. Russo-Averchi, M. Heiss, S. Sonderegger, C. Magen, J. Arbiol, R. T. Phillips, and A. Fontcuberta i Morral, Exciton footprint of self-assembled AlGaAs quantum dots in core–shell nanowires, *Phys. Rev. B* **90**, 075307 (2014).

[160] P. Corfdir, Y. Fontana, B. Van Hattem, E. Russo-Averchi, M. Heiss, A. Fontcuberta i Morral, and R. T. Phillips, Tuning the g-factor of neutral and charged excitons confined to self-assembled (Al,Ga)As shell quantum dots, *Appl. Phys. Lett.* **105**, 223111 (2014).

[161] J. C. Bourgoin, H. J. von Bardeleben, and D. Stievenard, Native defects in gallium arsenide, *J. Appl. Phys.* **64**, R65 (1988).

[162] J. P. Contour, G. Neu, M. Leroux, C. Chaix, B. Levesque, and P. Etienne, An optical characterization of defect levels induced by MBE growth of GaAs, *J. Vac. Sci. Technol. B* **1**, 811 (1983).

[163] W. Shockley and W. T. Read, Statistics of the Recombinations of Holes and Electrons, *Phys. Rev.* **87**, 835–842 (1952).

[164] C. A. Warwick, W. Y. Jan, A. Ourmazd, and T. D. Harris, Does luminescence show semiconductor interfaces to be atomically smooth?, *Appl. Phys. Lett.* **56**, 2666–2668 (1990).

[165] K. Leosson, J. Jensen, W. Langbein, and J. Hvam, Exciton localization and interface roughness in growth-interrupted GaAs/AlAs quantum wells, *Phys. Rev. B* **61**, 10322–10329 (2000).

[166] P. Petroff, A. Cho, F. Reinhart, A. Gossard, and W. Wiegmann, Alloy Clustering in $Ga_{1-x}Al_xAs$ Compound Semiconductors Grown by Molecular Beam Epitaxy, *Phys. Rev. Lett.* **48**, 170–173 (1982).

[167] K. Muraki, S. Fukatsu, Y. Shiraki, and R. Ito, Surface segregation of In atoms during molecular beam epitaxy and its influence on the energy levels in InGaAs/GaAs quantum wells, *Appl. Phys. Lett.* **61**, 557 (1992).

[168] Y. G. Chai, R. Chow, and C. E. C. Wood, The effect of growth conditions on Si incorporation in molecular beam epitaxial GaAs, *Appl. Phys. Lett.* **39**, 800–803 (1981).

[169] M. Luysberg, H. Sohn, A. Prasad, P. Specht, Z. Liliental-Weber, E. R. Weber, J. Gebauer, and R. Krause-Rehberg, Effects of the growth temperature and As/Ga flux ratio on the incorporation of excess As into low temperature grown GaAs, *J. Appl. Phys.* **83**, 561–566 (1998).

[170] N. Moll, a. Kley, E. Pehlke, and M. Scheffler, GaAs equilibrium crystal shape from first principles, *Phys. Rev. B* **54**, 8844–8855 (1996).

[171] W. I. Wang, Instabilities of (110) III-V compounds grown by molecular beam epitaxy, *J. Vac. Sci. Technol. B* **1**, 630 (1983).

[172] E. S. Tok, T. S. Jones, J. H. Neave, J. Zhang, and B. a. Joyce, Is the arsenic incorporation kinetics important when growing GaAs(001), (110), and (111)A films?, *Appl. Phys. Lett.* **71**, 3278 (1997).

[173] J. Zhou, Y. Huang, Y. Li, and W. Y. Jia, Growth and properties of AlGaAs/GaAs heterostructures on GaAs(110) surface, *J. Cryst. Growth* **81**, 221–223 (1987).

[174] L. T. P. Allen, E. R. Weber, J. Washburn, and Y. C. Pao, Device quality growth and characterization of (110) GaAs grown by molecular beam epitaxy, *Appl. Phys. Lett.* **51**, 670–672 (1987).

[175] L. Allen, E. Weber, J. Washburn, Y. Pao, and A. Elliot, Characterization of surface faceting on (110)GaAs/GaAs grown by molecular beam epitaxy, *J. Cryst. Growth* **87**, 193–200 (1988).

[176] L. Pfeiffer, K. W. West, H. L. Stormer, J. P. Eisenstein, K. W. Baldwin, D. Gershoni, and J. Spector, Formation of a high quality two-dimensional electron gas on cleaved GaAs, *Appl. Phys. Lett.* **56**, 1697–1699 (1990).

[177] E. S. Tok, J. H. Neave, M. J. Ashwin, B. a. Joyce, and T. S. Jones, Growth of Si-doped GaAs(110) thin films by molecular beam epitaxy; Si site occupation and the role of arsenic, *J. Appl. Phys.* **83**, 4160–4167 (1998).

[178] M. Yoshita, H. Akiyama, L. N. Pfeiffer, and K. W. West, Formation of flat monolayer-step-free (110) GaAs surfaces by growth interruption annealing during cleaved-edge epitaxial overgrowth, *Jpn. J. Appl. Phys.* **40**, 252–254 (2001).

[179] B. Loitsch, N. Jeon, M. Döblinger, J. Winnerl, E. Parzinger, S. Matich, U. Wurstbauer, H. Ried, G. Abstreiter, J. J. Finley, L. J. Lauhon, and G. Koblmüller, Suppression of alloy fluctuations in GaAs-AlGaAs core-shell nanowires, *Appl. Phys. Lett.* **109**, 093105 (2016).

[180] a. Avery, H. Dobbs, D. Holmes, B. Joyce, and D. Vvedensky, Nucleation and Growth of Islands on GaAs Surfaces, *Phys. Rev. Lett.* **79**, 3938–3941 (1997).

[181] D. Holmes, E. Tok, J. Sudijono, T. Jones, and B. Joyce, Surface evolution in GaAs(110) homoepitaxy; from microscopic to macroscopic morphology, *J. Cryst. Growth* **192**, 33–46 (1998).

[182] M. Wassermeier, H. Yang, E. Tournié, L. Däweritz, and K. Ploog, Growth mechanism of GaAs on (110) GaAs studied by high-energy electron diffraction and atomic force microscopy, *J. Vac. Sci. Technol. B* **12**, 2574–2578 (1994).

[183] T. Someya, H. Akiyama, and H. Sakaki, Molecular Beam Epitaxial Growth of $In_{0.15}Ga_{0.85}As$ Quantum Wells on (110) GaAs Surfaces, *Jpn. J. Appl. Phys.* **35**, 2544–2547 (1996).

[184] R. Hey, A. Trampert, U. Jahn, O. Couto, and P. Santos, Growth of (In,Ga)As/(Al,Ga)As quantum wells on GaAs(110) by MBE, *J. Cryst. Growth* **301–302**, 158–162 (2007).

[185] Y. Horikoshi, M. Kawashima, and H. Yamaguchi, Migration-Enhanced Epitaxy of GaAs and AlGaAs, *Jpn. J. Appl. Phys.* **27**, 169–179 (1988).

[186] M. López, Y. Takano, K. Pak, and H. Yonezu, Realization of low facet density and the growth mechanism of GaAs on GaAs(110) by migration-enhanced epitaxy, *Appl. Phys. Lett.* **58**, 580–582 (1991).

[187] R. Hey, a. Trampert, and P. Santos, (In,Ga)As/GaAs quantum wells on GaAs(110), *Phys. Status Solidi C* **3**, 651–654 (2006).

[188] J. Zhang, J. Neave, B. Joyce, A. Taylor, S. Armstrong, and M. Pemble, A RHEED and RA study of MEE growth, *Appl. Surf. Sci.* **60–61**, 215–223 (1992).

[189] A. Díaz Álvarez, T. Xu, G. Tütüncüoglu, T. Demonchaux, J.-P. Nys, M. Berthe, F. Matteini, H. a. Potts, D. Troadec, G. Patriarche, J.-F. Lampin, C. Coinon, A. Fontcuberta i Morral, R. E. Dunin-Borkowski, P. Ebert, and B. Grandidier, Non-stoichiometric Low-Temperature Grown GaAs Nanowires, *Nano Lett.* **15**, 6440–6445 (2015).

[190] Y. Horikoshi, Migration-enhanced epitaxy of GaAs and AlGaAs, *Semicond. Sci. Technol.* **8**, 1032–1051 (1993).

[191] Y. Y.-N. Guo, T. Burgess, Q. Gao, H. H. Tan, C. Jagadish, and J. Zou, Polarity-driven Non-uniform Composition in InGaAs Nanowires., *Nano Lett.* **13**, 5085–9 (2013).

[192] X. Yuan, P. Caroff, F. Wang, Y. Guo, Y. Wang, H. E. Jackson, L. M. Smith, H. H. Tan, and C. Jagadish, Antimony Induced (112)A Faceted Triangular $GaAs_{1-x}Sb_x$/InP Core/Shell Nanowires and Their Enhanced Optical Quality, *Adv. Funct. Mater.* **25**, 5300–5308 (2015).

[193] J. Treu, T. Stettner, M. Watzinger, S. Morkötter, M. Döblinger, S. Matich, K. Saller, M. Bichler, G. Abstreiter, J. J. Finley, J. Stangl, and G. Koblmüller, Lattice-Matched InGaAs-InAlAs Core-Shell Nanowires with Improved Luminescence and Photoresponse Properties, *Nano Lett.* **15**, 3533–3540 (2015).

[194] L. Geelhaar, J. Marquez, K. Jacobi, A. Kley, P. Ruggerone, and M. Scheffler, A scanning tunneling microscopy study of the GaAs(112) surfaces, *Microelectron. J.* **30**, 393–396 (1999).

[195] D. E. Eastman and W. D. Grobman, Photoemission Densities of Intrinsic Surface States for Si, Ge, and GaAs, *Phys. Rev. Lett.* **28**, 1378–1381 (1972).

[196] R. Ludeke and A. Koma, Electronic surface states on clean and oxygen-exposed GaAs surfaces, *J. Vac. Sci. Technol. B* **13**, 241–247 (1976).

[197] P. a. Alekseev, M. S. Dunaevskiy, V. P. Ulin, T. V. Lvova, D. O. Filatov, A. V. Nezhdanov, A. I. Mashin, and V. L. Berkovits, Nitride Surface Passivation of GaAs Nanowires: Impact on Surface State Density, *Nano Lett.* **15**, 63–68 (2015).

[198] J. Noborisaka, J. Motohisa, S. Hara, and T. Fukui, Fabrication and characterization of freestanding GaAs/AlGaAs core-shell nanowires and AlGaAs nanotubes by using selective-area metalorganic vapor phase epitaxy, *Appl. Phys. Lett.* **87**, 093109 (2005).

[199] O. Demichel, M. Heiss, J. Bleuse, H. Mariette, and A. Fontcuberta i Morral, Impact of surfaces on the optical properties of GaAs nanowires, *Appl. Phys. Lett.* **97**, 201907 (2010).

[200] C.-C. Chang, C.-Y. Chi, M. Yao, N. Huang, C.-C. Chen, J. Theiss, A. W. Bushmaker, S. Lalumondiere, T.-W. Yeh, M. L. Povinelli, C. Zhou, P. D. Dapkus, and S. B. Cronin, Electrical and Optical Characterization of Surface Passivation in GaAs Nanowires, *Nano Lett.* **12**, 4484–9 (2012).

[201] A. Darbandi, O. Salehzadeh, P. Kuyanov, R. R. LaPierre, and S. P. Watkins, conduction Surface passivation of tellurium-doped GaAs nanowires by GaP : Effect on electrical conduction, *J. Appl. Phys.* **115**, 234305 (2014).

[202] G. Mariani, A. C. Scofield, C.-H. Hung, and D. L. Huffaker, GaAs nanopillar-array solar cells employing in situ surface passivation, *Nat. Commun.* **4**, 1497 (2013).

[203] P. Corfdir, H. Küpers, R. B. Lewis, T. Flissikowski, H. T. Grahn, L. Geelhaar, and O. Brandt, Exciton dynamics in GaAs/(Al,Ga)As core–shell nanowires with shell quantum dots, *Phys. Rev. B* **94**, 155413 (2016).

[204] J. D. Lambkin, D. J. Dunstan, K. P. Homewood, L. K. Howard, and M. T. Emeny, Thermal quenching of the photoluminescence of InGaAs/GaAs and InGaAs/AlGaAs strained-layer quantum wells, *Appl. Phys. Lett.* **57**, 1986–1988 (1990).

[205] D. Rudolph, L. Schweickert, S. Morkötter, L. Hanschke, S. Hertenberger, M. Bichler, G. Koblmüller, G. Abstreiter, and J. J. Finley, Probing the trapping and thermal activation dynamics of excitons at single twin defects in GaAs-AlGaAs core-shell nanowires, *New J. Phys.* **15**, 113032 (2013).

[206] M. Leroux, N. Grandjean, B. Beaumont, G. Nataf, F. Semond, J. Massies, and P. Gibart, Temperature quenching of photoluminescence intensities in undoped and doped GaN, *J. Appl. Phys.* **86**, 3721 (1999).

[207] M. Gurioli, A. Vinattieri, M. Colocci, C. Deparis, J. Massies, G. Neu, A. Bosacchi, and S. Franchi, Temperature dependence of the radiative and nonradiative recombination time in GaAs/$Al_xGa_{1-x}As$ quantum-well structures, *Phys. Rev. B* **44**, 3115–3124 (1991).

[208] R. L. Greene, K. K. Bajaj, and D. E. Phelps, Energy levels of Wannier excitons in GaAs-$Ga_{1-x}Al_xAs$ quantum-well structures, *Phys. Rev. B* **29**, 1807–1812 (1984).

[209] D. Orani, A. Polimeni, A. Patanè, M. Capizzi, F. Martelli, A. D'Andrea, N. Tomassini, P. Borri, M. Gurioli, and M. Colocci, Binding Energy and Lifetime of Excitons in $In_xGa_{1-x}As$/GaAs Quantum Wells, *Phys. Status Solidi A* **164**, 107–110 (1997).

[210] J. R. Botha and A. W. R. Leitch, Thermally activated carrier escape mechanisms from $In_xxGa_{1-x}As$/GaAs quantum wells, *Phys. Rev. B* **50**, 18147–18152 (1994).

[211] L. C. Andreani, F. Tassone, and F. Bassani, Radiative lifetime of free excitons in quantum wells, *Solid State Commun.* **77**, 641–645 (1991).

[212] D. S. Citrin, Radiative lifetimes of excitons in quantum wells: Localization and phase-coherence effects, *Phys. Rev. B* **47**, 3832–3841 (1993).

[213] T. Amand, X. Marie, B. Dareys, J. Barrau, M. Brousseau, D. J. Dunstan, J. Y. Emery, and L. Goldstein, Well-width dependence of the excitonic lifetime in strained III-V quantum wells, *J. Appl. Phys.* **72**, 2077–2079 (1992).

[214] G. Bacher, C. Hartmann, H. Schweizer, T. Held, G. Mahler, and H. Nickel, Exciton dynamics in $In_xGa_{1-x}As/GaAs$ quantum-well heterostructures: Competition between capture and thermal emission, *Phys. Rev. B* **47**, 9545–9555 (1993).

[215] D. Tedeschi, M. De Luca, H. A. Fonseka, Q. Gao, F. Mura, H. H. Tan, S. Rubini, F. Martelli, C. Jagadish, M. Capizzi, and A. Polimeni, Long-Lived Hot Carriers in III-V Nanowires, *Nano Lett.* **16**, 3085–3093 (2016).

[216] K. Komolibus, A. C. Scofield, K. Gradkowski, T. J. Ochalski, H. Kim, D. L. Huffaker, and G. Huyet, Improved room-temperature luminescence of core-shell InGaAs/GaAs nanopillars via lattice-matched passivation, *Appl. Phys. Lett.* **108**, 061104 (2016).

[217] B. Deveaud, T. C. Damen, J. Shah, and C. W. Tu, Dynamics of exciton transfer between monolayer-flat islands in single quantum wells, *Appl. Phys. Lett.* **51**, 828–830 (1987).

[218] N. Yamada, G. Roos, and J. S. Harris, Threshold reduction in strained InGaAs single quantum well lasers by rapid thermal annealing, *Appl. Phys. Lett.* **59**, 1040–1042 (1991).

[219] B. L. Olmsted and S. N. Houde-Walter, Dependence of Al-Ga interdiffusion in AlGaAs on stoichiometry between Ga-rich and As-rich solidus limits, *Appl. Phys. Lett.* **60**, 368–370 (1992).

[220] S. Bürkner, M. Baeumler, J. Wagner, E. C. Larkins, W. Rothemund, and J. D. Ralston, Influence of interdiffusion processes on optical and structural properties of pseudomorphic $In_{0.35}Ga_{0.65}As/GaAs$ multiple quantum well structures, *J. Appl. Phys.* **79**, 6818–6825 (1996).

[221] A. Hierro, J. M. Ulloa, J. M. Chauveau, A. Trampert, M. A. Pinault, E. Tournié, A. Guzmán, J. L. Sánchez-Rojas, and E. Calleja, Annealing effects on the crystal structure of GaInNAs quantum wells with large In and N content grown by molecular beam epitaxy, *J. Appl. Phys.* **94**, 2319–2324 (2003).

[222] U. Gösele, T. Tan, M. Schultz, U. Egger, P. Werner, R. Scholz, and O. Breitenstein, Diffusion in GaAs and Related Compounds: Recent Developments, *Defect and Diffusion Forum* **143-147**, 1079–1094 (1997).

[223] P. Kasanaboina, M. Sharma, P. Deshmukh, C. L. Reynolds, Y. Liu, and S. Iyer, Effects of Annealing on GaAs/GaAsSbN/GaAs Core-Multi-shell Nanowires, *Nanoscale Res. Lett.* **11**, 47 (2016).

[224] C. T. Foxon, J. A. Harvey, and B. A. Joyce, The evaporation of GaAs under equilibrium and non-equilibrium conditions using a modulated beam technique, *J. Phys. Chem. Solids* **34**, 1693–1701 (1973).

[225] Z. Zhong, Z. Li, Q. Gao, Z. Li, K. Peng, L. Li, S. Mokkapati, K. Vora, J. Wu, G. Zhang, Z. Wang, L. Fu, H. H. Tan, and C. Jagadish, Efficiency enhancement of axial junction InP single nanowire solar cells by dielectric coating, *Nano Energy* **28**, 106–114 (2016).

[226] M. Bouwes Bavinck, M. Zieliński, B. J. Witek, T. Zehender, E. P. Bakkers, and V. Zwiller, Controlling a Nanowire Quantum Dot Bandgap Using a Straining Dielectric Envelope, *Nano Lett.* **12**, 6206–11 (2012).

[227] P. Stepanov, M. E. Aizarna, J. Bleuse, N. S. Malik, Y. Curé, E. Gautier, V. Favre-Nicolin, J.-M. Gérard, and J. Claudon, Large and uniform optical emission shifts in quantum dots externally strained along their growth axis, *Nano Lett.* **16**, 3215–3220 (2016).

[228] S. O'Brien, J. R. Shealy, D. P. Bour, L. Elbaum, and J. Y. Chi, Effects of rapid thermal annealing and SiO_2 encapsulation on GaInAs/AlInAs heterostructures, *Appl. Phys. Lett.* **56**, 1365–1367 (1990).

[229] M. Ichimura, A. Usami, and T. Wada, Thermodynamic model for the annealing process of Si-implanted GaAs, *Model. Simul. Mater. Sc.* **1**, 529–538 (1993).

[230] O. M. Khreis, W. P. Gillin, and K. P. Homewood, Interdiffusion: A probe of vacancy diffusion in III-V materials, *Phys. Rev. B* **55**, 15813–15818 (1997).

[231] K.-C. Lin and S.-C. Lee, The structural and optical properties of a-SiN_x:H prepared by plasma-enhanced chemical-vapor deposition, *J. Appl. Phys.* **72**, 5474–5482 (1992).

[232] T. Longjuan, Z. Yinfang, Y. Jinling, L. Yan, Z. Wei, X. Jing, L. Yunfei, and Y. Fuhua, Dependence of wet etch rate on deposition, annealing conditions and etchants for PECVD silicon nitride film, *Journal of Semiconductors* **30**, 096005 (2009).

[233] D. E. Aspnes, S. M. Kelso, R. A. Logan, and R. Bhat, Optical properties of $Al_xGa_{1-x}As$, *J. Appl. Phys.* **60**, 754–767 (1986).

[234] K. Luke, Y. Okawachi, M. R. E. Lamont, A. L. Gaeta, and M. Lipson, Broadband mid-infrared frequency comb generation in a Si_3N_4 microresonator, *Opt. Lett.* **40**, 4823 (2015).

[235] N. Anttu, K. L. Namazi, P. M. Wu, P. Yang, H. Xu, H. Q. Xu, and U. Håkanson, Drastically increased absorption in vertical semiconductor nanowire arrays: A non-absorbing dielectric shell makes the difference, *Nano Res.* **5**, 863–874 (2012).

[236] A. Patanè, A. Polimeni, M. Capizzi, and F. Martelli, Linewidth analysis of the photoluminescence of $In_xGa_{1-x}As/GaAs$ quantum wells (x=0.09, 0.18, 1.0), *Phys. Rev. B* **52**, 2784–2788 (1995).

[237] O. M. Khreis, K. P. Homewood, and W. P. Gillin, Interdiffusion in InGaAs/GaAs: The effect of growth conditions, *J. Appl. Phys.* **84**, 232–236 (1998).

[238] M. Albrecht, V. Grillo, T. Remmele, H. P. Strunk, A. Y. Egorov, G. Dumitras, H. Riechert, A. Kaschner, R. Heitz, and A. Hoffmann, Effect of annealing on the In and N distribution in InGaAsN quantum wells, *Appl. Phys. Lett.* **81**, 2719–2721 (2002).

[239] J. Bolinsson, L. Ouattara, W. A. Hofer, N. Sköld, E. Lundgren, A. Gustafsson, and A. Mikkelsen, Direct observation of atomic scale surface relaxation in ortho twin structures in GaAs by XSTM, *J. Phys.: Condens. Matter* **21** (2009).

[240] P. C. McIntyre, H. Adhikari, I. A. Goldthorpe, S. Hu, P. W. Leu, A. F. Marshall, and C. E. Chidsey, Group IV semiconductor nanowire arrays: Epitaxy in different contexts, *Semicond. Sci. Technol.* **25** (2010).

[241] T. Rieger, M. Luysberg, T. Schäpers, D. Grützmacher, and M. I. Lepsa, Molecular Beam Epitaxy Growth of GaAs/InAs Core-Shell Nanowires and Fabrication of InAs Nanotubes, *Nano Lett.* **12**, 5559–64 (2012).

[242] R. Thomas, D. Benoit, L. Clément, P. Morin, D. Cooper, and F. Bertin, Characterization of Strain Induced by PECVD Silicon Nitride Films in Transistor Channels, *AIP Conf. Proc.* **1395**, 90–94 (2011).

[243] G. Signorello, S. Karg, M. T. Björk, B. Gotsmann, and H. Riel, Tuning the light emission from GaAs nanowires over 290 meV with uniaxial strain., *Nano Lett.* **13**, 917–924 (2013).

[244] G. L. Bir and G. E. Pikus, *Symmetry and Strain-Induced Effects in Semiconductors*, Wiley: New York (1974).

[245] E. Tournie, O. Brandt, and K. H. Ploog, Low-density band-filling in strained InAs quantum wells, *Applied Physics A Solids and Surfaces* **56**, 109–112 (1993).

[246] N. Bertru, O. Brandt, R. Klann, A. Mazuelas, W. Ulrici, and K. H. Ploog, Excitons in strained (Ga,In)Sb/GaSb quantum wells, *Phys. Rev. B* **55**, 4503–4505 (1997).

[247] R. Pässler, Basic Model Relations for Temperature Dependencies of Fundamental Energy Gaps in Semiconductors, *Phys. Status Solidi B* **200**, 155–172 (1997).

[248] R. Pässler, Temperature dependence of exciton peak energies in multiple quantum wells, *J. Appl. Phys.* **83**, 3356–3359 (1998).

[249] S. Martini, A. A. Quivy, A. Tabata, and J. R. Leite, Influence of the temperature and excitation power on the optical properties of InGaAs/GaAs quantum wells grown on vicinal GaAs(001) surfaces, *J. Appl. Phys.* **90**, 2280–2289 (2001).

[250] E. M. Lopes, J. L. Duarte, I. F. L. Dias, L. C. Poças, E. Laureto, and J. C. Harmand, Photoluminescence properties of a Si doped InGaAs/InGaAlAs superlattice, *J. Phys.: Condens. Matter* **19**, 086207 (2007).

[251] H. Schömig, S. Halm, A. Forchel, G. Bacher, J. Off, and F. Scholz, Probing Individual Localization Centers in an InGaN/GaN Quantum Well, *Phys. Rev. Lett.* **92**, 106802 (2004).

[252] F. Boxberg, N. Søndergaard, and H. Q. Xu, Photovoltaics with piezoelectric core–shell nanowires, *Nano Lett.* **10**, 1108–12 (2010).

[253] M. Hocevar, L. T. Thanh Giang, R. Songmuang, M. I. den Hertog, L. Besombes, J. Bleuse, Y.-M. Niquet, and N. T. Pelekanos, Residual strain and piezoelectric effects in passivated GaAs/AlGaAs core-shell nanowires, *Appl. Phys. Lett.* **102**, 191103 (2013).

List of Figures

2.1 Description of MBE setup 6
2.2 Model of the luminescence process 8
2.3 Schematic diagram of μ-PL setup. 10
2.4 Attenuation of the PL setup. 11
2.5 Schematic diagram of the time-resolved PL setup. 12
2.6 Data presentation from time-resolved PL 12

3.1 SEM image of GaAs NWs grown on a Si (111) substrate covered by a thin native oxide. 15
3.2 Model of the wurtzite and zincblende crystal structure 16
3.3 EBL mask outline. 18
3.4 AFM micrographs of Si(111) surfaces treated by different surface preparations. 19
3.5 SEM micrographs comparing NW samples grown on substrates prepared with different surface treatments prior to growth. 20
3.6 SEM top-view micrographs of Ga droplets deposited on unpatterned Si(111) substrates with different surface treatments. 21
3.7 Vertical yield for varying V/III flux ratio. 22
3.8 Micrographs of NW arrays on substrates patterned by EBL and NIL. . . . 24

4.1 Results from two-step growth procedure. 29
4.2 NW diameter as a function of Ga flux. 30
4.3 Average radial growth rate. 31
4.4 NW shape calculated by the growth model. 34
4.5 Evaluation of experimental and effective V/III ratio. 36
4.6 Tapering as function of V/III ratio and growth time. 38
4.7 Tapering as a function of V/III ratio for different times and unique combinations of diameter and length for untapered NW morphologies 39
4.8 Map of calculated dopant density in the VS grown part. 42

5.1 Band-gap energy and strain with respect to GaAs as function of In content 46
5.2 Structure of NW core-shell samples. 47
5.3 PL of samples grown at different temperatures. 49
5.4 CL scans on samples grown at different temperatures. 51
5.5 PL of samples grown at different V/III ratios. 53

5.6 PL of samples grown at different growth rates. 54
5.7 Model of low index surfaces 55
5.8 PL comparison of samples grown using As sources mounted at different cell ports. 57
5.9 TEM measurement on a core-shell NW 58
5.10 Cell configuration and corresponding flux sequence on the NW sidewall. 60
5.11 PL comparison of samples grown at different rotation speeds and using different Ga sources. 62

6.1 Power-dependent PL spectra of (In,Ga)As shell QW 66
6.2 Temperature-dependent PL for (In,Ga)As shell QW samples with different outer shell structures. 67
6.3 Integrated intensity of (In,Ga)As shell QW samples with different outer shell structure as a function of temperature. 68
6.4 PL transients of (In,Ga)As shell QW samples with different outer structure and model description. 71

7.1 SEM images of samples at different stages of the annealing process. 76
7.2 PL spectra of samples at different stages of the annealing process. 78
7.3 CL measurements on annealed core-shell NWs. 80
7.4 XRD measurements of samples at different stages of the annealing process. 81
7.5 PL spectra taken on NW ensembles and single NWs at varying excitation power. 85
7.6 PL measurements of the annealed sample as a function of temperature. . . 86

8.1 Measurements performed on a single NW 92
8.2 Proposed device structure for the integration of NWs with waveguides . . 94

Acknowledgements

This work would not have been possible without the guidance and support of many people. In this context, this thesis is not only the presentation of scientific results but also a symbol of my personal development over the last years. Therefore, I am grateful for the time that was given to me to learn how to explore complex problems and find solutions. During this time, the collaboration with experienced people formed the perfect surroundings for the development of many skills that I will profit from in the future. I am grateful to all people involved in different ways in this process.

I want to thank my doctoral supervisor Prof. Dr. Henning Riechert for giving me the opportunity to work at Paul-Drude-Institut (PDI) and conduct my scientific studies. Through my previous work on my master thesis I already had an idea of what to expect from working at PDI and I was happy to be welcomed as a PhD candidate. Especially his efforts in assuring the supply of patterned substrate for NW growth made this work possible.

I want to thank Dr. Lutz Geelhaar for the scientific supervision as the head of the nanowire group. His guidance was a good mixture of direct advice in difficult situations and the freedom for making my own decisions. He always encouraged and motivated me in the right moments and gave me the feeling that he trusted in those decisions. For this atmosphere I am very grateful. Furthermore, he is a great teacher of scientific style, showing me how to compose manuscripts or prepare presentations, and eventually proof reading this thesis. Finally, I want to thank him for giving me the possibility to attend international conferences that helped me in locating my position in the research community.

During the work on this thesis, I had the privilege to closely work with two outstanding researchers who had a tremendous impact on my work: Dr. Ryan Lewis was always open to questions and discussions of all sorts of ideas concerning growth phenomena and possible consequences, which resulted in countless hours of conversations over the last years. He always encouraged me to push things forward to obtain an understanding that is comprehensive and meaningful. Dr. Pierre Corfdir taught me almost everything I know about photoluminescence. His intuitive understanding of complex topics and broad knowledge helped me to understand more complicated results.

I want to thank the colleagues who shared their experience and knowledge with me and even supplied additional experimental data. The culture of open doors and helpfulness made my work so pleasant. These people include Dr. Oliver Brandt, Dr. Uwe Jahn, Dr. Jonas Lähnemann, and Dr. Timur Flissikowski who helped me with all things

regarding luminescence experiments, Dr. Esperanza Luna, Dr. Achim Trampert, and Dr. Michael Niehle regarding the microstructure of my samples, as well as Dr. Klaus Biermann regarding special question about MBE.

A large part of this thesis relied on the processing of substrates and samples, which was elaborated and planned with the head of the processing lab, Dr. Abbes Tahraoui. He was always very committed in trying new ideas and optimizing existing processes. For the processing of samples at PDI I am thankful to Sander Rauwerdink, Bernd Drescher, Walid Anders, and Sebastian Meister, who put much effort in always providing the best possible results. Furthermore, I am thankful for the successful cooperation with our colleagues from the process technology department at the Ferdinand-Braun-Institut led by Dr. Olaf Krüger. Here, Mathias Matalla made sure that we had a reliable source of patterned substrates of highest quality during the last years. Further thanks go to Dr. Ina Ostermay, who provided the SiN_x layers that were suitable for our purposes.

At PDI the researcher can concentrate on the scientific side because many technicians help and care for the technical side of the laboratory work. Without their efforts the results of this thesis would have not been possible. I want to thank Michael Höricke and Carsten Stemmler for their careful work of maintaining and improving the MBE setup that I used. Due to their experience and knowledge I could always be sure that the MBE was in its best possible state. Also I want to thank Claudia Hermann for caring for the functionality of the chemical lab which was central for this work. Finally, I want to thank Anne-Kathrin Bluhm for taking SEM images of the endless chain of samples over the last years.

The great working environment I had the privilege to experience during the last years was created in huge parts by my dear office mates, the members of the Nanowire group, and my fellow students who shared the same fate. All of these people made the last years so memorable. Thank you for the hundreds of lunches at the Mensa, the countless coffees at the Cafe, the Platz-beers, the fun in the newly established ornithology lab, the cookies at the student seminar, the cookies in the hallway, the champagnes at the defenses, the chats about coffee in the coffee kitchen, the elevator jokes inside the elevator, the train rides during the fields trips, and so on and so forth.

Finally, I want to thank everybody who was not directly involved in my scientific work but supported me outside of the institute. I want to thank my family, and especially my parents who raised me to become an independent and confident person. Without their moral support I would have stopped long ago. Likewise, I am grateful for having Lara accompanying me during the last years. Thank you for being there for me and enduring all the stressful phases. Also I want to thank David in this part. Even though I sometimes took it for granted, now I realize how privileged I was to have such a good and old friend working next door. Our discussions at late hours in the institute or even later hours outside the institute helped me a lot in keeping focus and managing stress and fears during intense phases. Finally, I want to thank all my friends who supported me and respected shortcomings in intense phases.

Selbstständigkeitserklärung

Ich erkläre, dass ich die vorliegende Arbeit selbstständig und nur unter Verwendung der angegebenen Literatur und Hilfsmittel angefertigt habe.

Berlin, den 25.05.2018 Hanno Küpers